GREEN BANK OBSERVATORY

GBT Memo 315

A New GBT Holography System: Conceptual Design and Considerations for the Front End and Reference Antenna

Walter Klahold

September 30, 2024

Abstract

A conceptual design for a new holography system for the Green Bank Telescope is proposed which will allow use of astronomical sources to illuminate the primary reflector and measure large scale ($\sim D/15$) deformations over time scales of approximately 10 minutes. Whereas the current system is limited by its correlator bandwidth to using a small number of goestationary satellites with narrowband beacons as sources, the new system would be able to perform surface deformation measurements at essentially any antenna elevation within the limits of the GBT. And with sufficient sensitivity, it may also measure dynamic wind- or thermally-induced deformations, potentially opening up the daytime to high frequency observing.

Obtaining this sensitivity will require leveraging modern digital samplers to expand the correlator bandwidth to 1 GHz or more, increasing the reference antenna collecting area by a factor of 20 or more, and using a cryogenic front end. This memo will focus in particular on the practical challenges of meeting the specifications for the reference antenna and front end electronics, while a more detailed discussion of the digital correlator will be given in a future memo. Some discussion will also be devoted to several systematic measurement errors which are either unique or more acute in the new holography system and its area of application, with practical strategies being given to limit their effects.

1 Introduction

The current holography[1] system for the Green Bank Telescope was first installed in 2008, and following an initial period of testing and commissioning, it has been used successfully since then to measure deformations of the GBT's primary reflector surface to within $\sim$100 µm, ultimately leading to a substantial reduction in r.m.s. surface error from 390 µm to $\sim$240 µm and a corresponding increase in antenna aperture efficiency by $\sim$ 10% or more (Hunter et al., 2011). However, certain components of the system were in fact initially designed and built a decade or more previous to this, and as a result the capabilities of the current holography system are severely limited by the technology that was available at the time. Most importantly, the ADCs for the digital correlator backend have sufficient sample rate to

[1]Unless specified otherwise, we discuss traditional, or with-phase holography in this memo, which is to be distinguished from out-of-focus (OOF) holography

process a bandwidth of at most 100 kHz (White, 1993), and this in turn limits the available sources that can be used in a holography measurement to geostationary satellites with strong, narrowband satellite beacons included in Ku-band downlinks (e.g. Intelsat's Galaxy 18 and Galaxy 28).

This is disadvantageous for three main reasons. Firstly, suitable geostationary satellites are sparsely distributed in the sky, and so even if the measured surface deformations were accurately corrected by the GBT's active surface, there will typically be a long slew time between the source used for the holography measurement and a follow-up scientific observation. In the intervening interval, which could last up to about 10 minutes and include a slew in both azimuth and elevation, mechanical loading to the GBT structure from wind and gravity and thermal loading from the sun may have changed dramatically, thus negating the improvements from the previous surface correction.

A second, related problem is that the orbital parameters of these satellites are such that they appear at only a handful of elevations up to about the geographical colatitude of the GBT, or 51.567°. Thus, while there is sparse sky coverage below this elevation, there are no suitable satellite beacons whatsoever above this elevation, at least among geostationary satellites. The third disadvantage has to do with the fact that the geostationary satellites are owned, operated, and maintained by outside organizations, and there is no guarantee that the downlink beacons used for holography measurements will remain active or usable in the long term.

Virtually every one of the issues could be solved or mitigated if a sufficient number of astronomical sources could also be used. For the current holography system, its bandwidth is far too narrow to obtain sufficient sensitivity from these sources, which typically have a broadband emission spectrum approaching that of a blackbody and produce a radiant flux several orders of magnitude lower than that produced by satellites. However, with the somewhat recent advent of GSps ADCs, the possibility now exists that these astronomical sources could be used in holography measurements which leverage the radiometric sensitivity advantage of a wider system bandwidth, thus reducing the slew time to the follow-up scientific observations and potentially allowing for high frequency observing during the daytime.

This is the main driver behind recent efforts to design a new holography system for use on the GBT, and in this memo we will present a conceptual design for the new system. In particular, we will outline the primary system requirements and goals, the hardware and software changes that will be needed for the system to meet those requirements, and an overview of the conceptual design at the component level. A few technical challenges relating to the reference antenna and the use of cryogenic front ends are given special attention, as well as several potentially important systematic measurement errors which may seriously affect system performance and accuracy. The memo concludes with a basic cost estimate and development timeline. In general, the focus here will be to specify the key hardware requirements related to the front end electronics and optics, whereas the core features of the digital correlator backend will be discussed in mostly general terms, with a more detailed analysis being saved for a future memo.

2 System requirements

The typical use case for the current holography system has been to measure the GBT's primary reflector surface at sufficiently high resolution (sub-meter scales) to locate highly localized deformations caused by faulty actuators. This requires measuring the GBT beam out to 50 or more sidelobes over a period of a few hours. This is not suitable for measuring and correcting for dynamic deformations that occur on much shorter time scales, but the new holography system must still retain the capability of performing these types of measurements.

The additional requirements for the new system relate to a use case in which the source is generally much weaker and the total duration of the surface measurement must be much shorter. System specifications were therefore determined based on the following nominal use case:

- Source power flux density: 1-2 Jy minimum
- Total measurement time: $\sim$10 minutes
- Surface measurement uncertainty: 100 µm
- Spatial resolution: $D/15 = 6.67$ m

The lower limit to the source power flux density ensures that the system's required radiometric sensitivity remains reasonably achievable while still greatly expanding the list of suitable sources. As shown in Figure 1, at Ku-band, there are approximately 70 sources in the GBT calibrator catalog with the required minimum power flux density, and these have an average separation of about 24°, or about a 1 minute full-rate slew time. The total measurement time has been set in order to reduce the dynamic wind and thermal effects mentioned earlier. The time scale at which these effects become significant has so far not been sufficiently established, and so the upper limit to the measurement duration is approximate. The 1-σ surface measurement uncertainty corresponds to the required surface accuracy $\lambda_{min}/16$ =200 µm at the nominal minimum operating wavelength $\lambda_{min} = 3$ mm for the GBT (Maddalena, 1991).

The spatial resolution has been set based on the observation that the current empirical gravity model for the GBT surface, which is based on Out-of-Focus (OOF) holography measurements, has the largest statistical dispersion for the low order Zernike terms used to parameterize the surface (Maddalena, 2014). This implies that the deformations produced by wind and thermal loading are of predominantly large scale. The spatial resolution $\Delta x = D/15 = 6.67$ m corresponds to the requirement that the lowest 15 Zernike polynomials be measurable ($D = 100$ m is the GBT projected aperture diameter).

The final requirement for the new system is that it be available for use at all times, but without taking up a turret slot at the GBT Gregorian focus, which is the location for the test receiver. The current holography test receiver takes up its own turret slot and is installed only for a few weeks at a time before and after a high frequency observing season to identify faulty actuators. With the holography system available at all times, this allows for surface measurement and correction to take place once per observation rather than a few times per observing season.

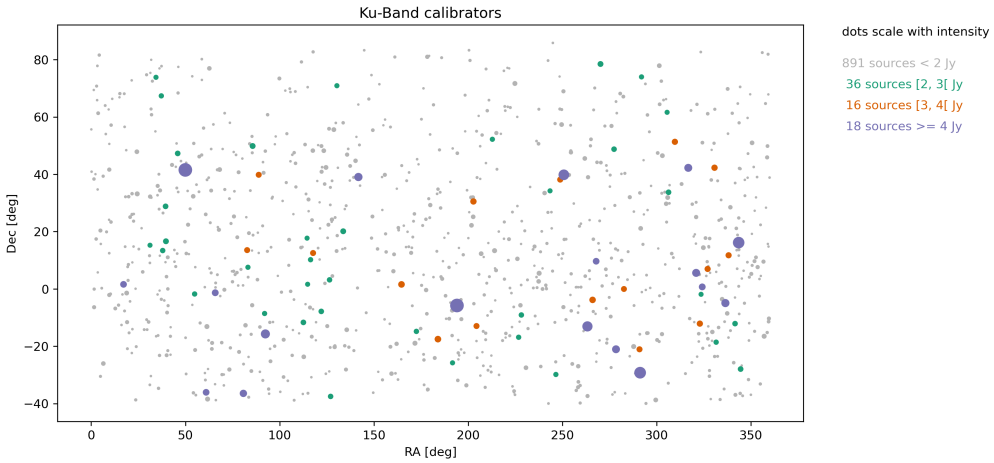

Figure 1: Map of Ku-band calibrators for the GBT, segregated according to power flux density (Credit: Anika Schmiedeke)

3 Hardware specifications

Fulfilling the system requirements given above is driven largely by the required radiometric sensitivity implied by the use case for the astronomical sources. An in-depth discussion of the sensitivity analysis is given in Appendix A, but will be summarized here. The analysis covers two scenarios of differing weather conditions: Scenario 1 represents "good" weather, where the receiver system temperature and atmospheric opacity are at the first quartile level, as determined from Green Bank weather statistics. Scenario 2 represents "bad" weather, where the system temperature and atmospheric opacity are at the third quartile level.

Fixed system and measurement parameters were chosen based on the system requirements in Section 2 or approximate estimates of technical constraints, and are shown in Table 5 of Section A.5. For convenience, we include a few of these here:

- Source power flux density: 2 Jy
- Reference antenna diameter: 2 m
- Aperture plane resolution: 6.67 m
- Number of points per map row/column: 20
- Instantaneous bandwidth: 1 GHz
- Integration time per point: 0.333 s

The number of points per row and column is chosen to avoid aliasing (see Section F.3), while the integration time was chosen according to a 10 minute total mapping time with a slew rate of one GBT beam FWHM per 4.5 integration times, which would limit beam smearing to 1% for an on-the-fly map (Mangum et al., 2007). Other system assumptions include a cryogenic front end, a Cassegrain reference antenna, and single polarization feeds. Freely varied parameters included test antenna edge taper, telescope elevation, and frequency.

In terms of optimum frequency, the sensitivity analysis demonstrated that the measurement uncertainty is a balance between interferometric sensitivity (number of wavelengths per unit surface displacement) and atmospheric opacity. In this case, the optimum frequency range turned out to be Ku-band, which is fortuitous since it is consistent with the requirement that the system have backwards compatibility with the Ku-band satellite downlinks. For Scenario 1, the minimum measurement uncertainty was 120 µm at 14 GHz and for Scenario 2 it was 140 µm at 12 GHz (both evaluated at zenith). While neither of these meet the required 100 µm measurement uncertainty requirement, we can expect a nominal factor of $\sqrt{2}$ decrease in uncertainty if both the test and reference feeds were made dual polarized (assuming an unpolarized source). For this case, the uncertainty drops to 80 µm and 100 µm for scenarios 1 and 2, respectively. From this we arrive at the following system specifications:

- Operating frequency: Ku-band
- Instantaneous system bandwidth: 1 GHz minimum
- Test antenna edge taper: 8 dB
- Reference antenna diameter: 2 m minimum
- Reference antenna configuration: Cassegrain
- Front end cryogenically cooled
- Test and reference antennas dual polarized

The final requirement that the system be available at all times and without taking up its own turret slot is complicated by the need to cryogenically cool the front end. It appears that a suitable solution would be to have the holography test receiver share a dewar and refrigerator with the KFPA receiver. As described in further detail in Section 5.2, this would require fairly minimal modifications to the KFPA dewar and turret hole cover as well as upgrading its refrigerator to a CTI model 1020, which would be beneficial to the KFPA receiver anyway. The holography reference receiver, would be permanently installed at the location of the current one, just above the subreflector. The details of supplying cryogenic cooling to its front end electronics are also given in Section 5.2.

4 Overview of the new holography system

4.1 Analog front end

A block diagram of the proposed holography system is shown in Figure 2. As mentioned above, both the test and reference receiver include dual-polarized feeds, and here the polarizations are represented as being linear. This choice was made on the basis that, as shown, all receiver components from the feed to the second stage amplifiers are cryogenically cooled, and given that the design requires the test receiver to share a dewar with the KFPA, the excess bulk taken up by waveguide components to convert between circular and linear polarizations would be disadvantageous. It is possible that circularly polarized feeds would

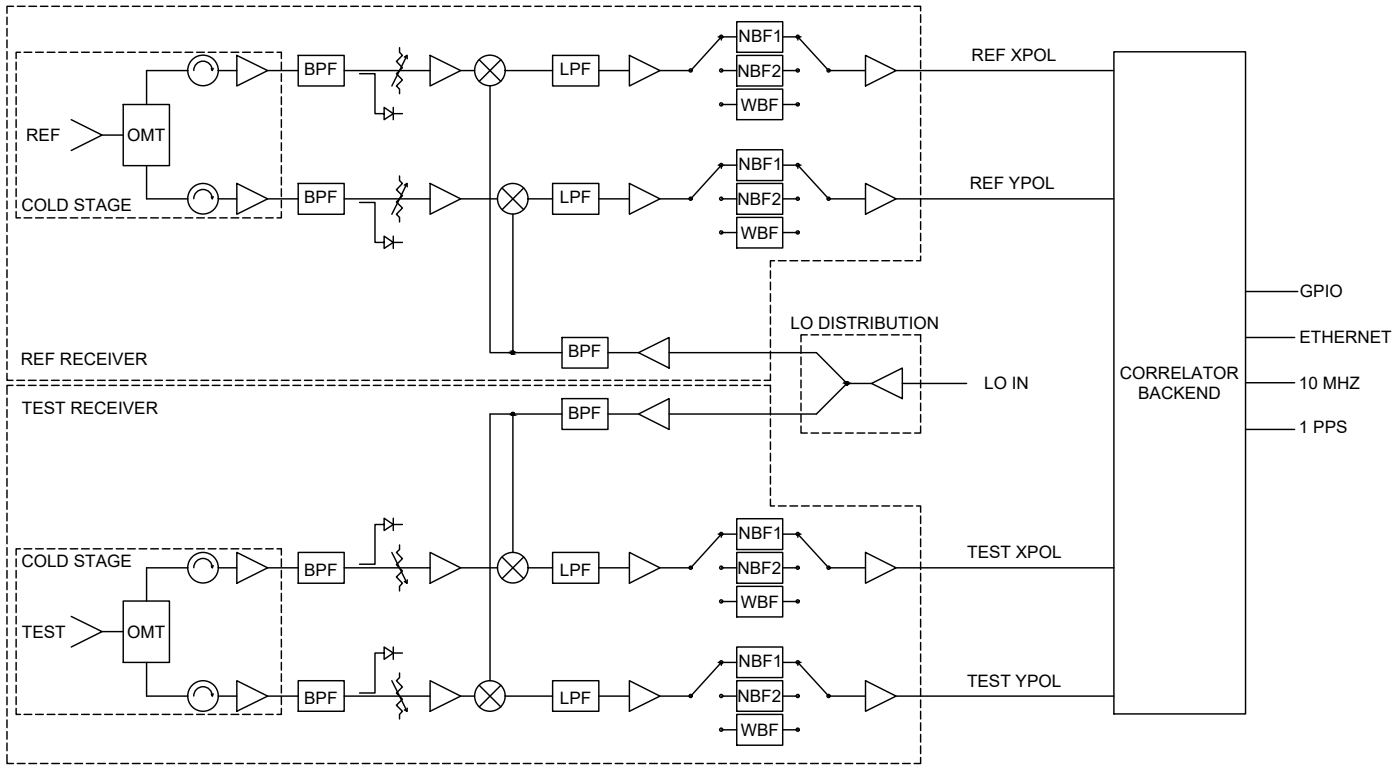

Figure 2: Block diagram of proposed holography system. OMT=orthomode transducer, BPF=bandpass filter, LPF=lowpass filter, NBF1=10 kHz wide narrowband filter, NBF2=100 kHz wide narrowband filter, WBF=wideband filter. XPOL and YPOL refer to the dual linear polarizations for both the test and reference receivers. LO refers to a local oscillator signal provided by either of two available frequency synthesizers at the GBT (LO1A or LO1B). 1 PPS (pulse-per-second) and 10 MHz are reference signals phase-locked to the site maser and are used as a synchronization trigger and timing reference, respectively. TEST and REF denote the cooled feed horns for the corresponding receivers, which illuminate either the GBT or the Cassegrain reference antenna.

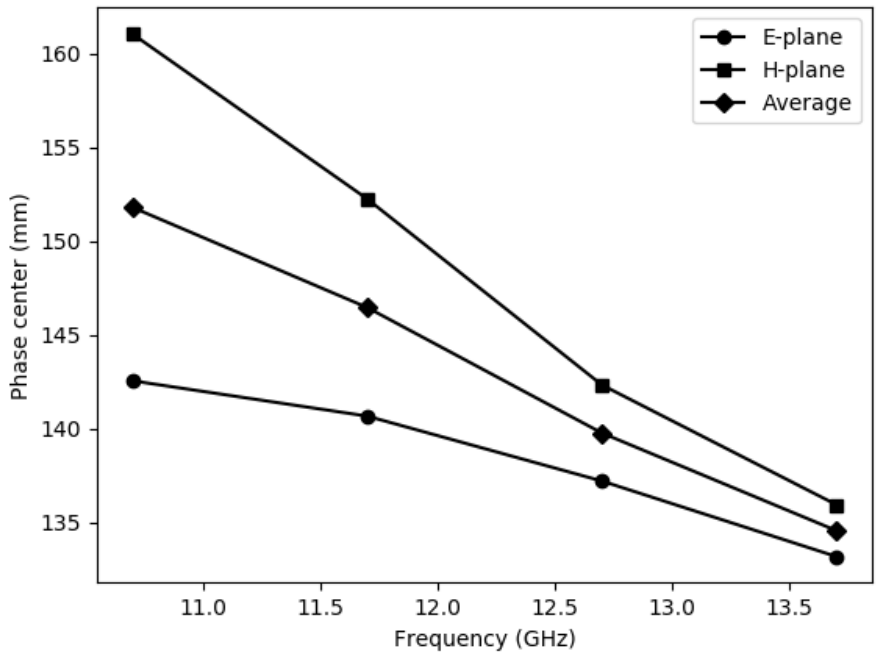

Figure 3: Calculated axial positions of E- and H-plane and average phase centers for the test feed of the current holography system

mitigate misalignment-induced decorrelation of the test and reference signals, but this has not been thoroughly explored.

While a new feed horn for the reference receiver will likely have to be re-designed according to the chosen reference antenna shape and geometry, it is possible that the feed horn for the test receiver may be re-used from the current system. It has a 4 dB edge taper in order to provide adequate sensitivity over the majority of the GBT primary reflector (Hunter et al., 2011), and this is reasonably close to the optimal 8 dB edge taper determined in the sensitivity analysis in Section A.5.

Whether or not it gets re-used, however, one drawback to having a shallow edge taper is that the E- and H-plane phase centers tend to have a wider separation along the feed axis, which in turn introduces an astigmatic phase distribution over the projected aperture plane even for the case where there are no deformations of the reflector surface. Another drawback is that the frequency dependence of the phase centers also tends to increase (Balanis, 2005). From the simulation results shown in Figure 3 for the current test receiver feed, both of these features can be observed. In principle this can be accounted for using lab measurements of the feed beam pattern, but if the feeds are dual polarized and there is reasonable symmetry between orthogonal polarizations, the feed-induced astigmatism measured in one polarization should match that in the other after a rotation by 90°, which would allow these effect to be determined in-situ and calibrated out.

The orthomode transducers (OMTs) following the feeds have been left unspecified, although their performance is expected not to be critical given that the targeted fractional

bandwidth is limited to about 0.1:1 by the backend. The isolators following the OMTs are similarly unspecified, although we require that they be waveguide isolators to reduce their noise temperature contribution.

The first stage low noise amplifiers (LNAs) on the other hand will be critical in determining the overall system sensitivity. In the analysis carried out in Appendix A, it was assumed the test and reference receiver temperatures were in the range of 3-4 K, which corresponds to the noise temperature of modern cryogenic LNAs operating at Ku-band. All waveguide components including the feeds are also cooled to mitigate additional contributions to the noise temperature.

After the first stage LNAs all components are presumed to be at ambient temperature. The first of these are a set of bandpass filters (BPF), which are primarily meant to attenuate any unwanted RFI. The design of these filters will be challenging, since they also must let through the small range of frequencies occupied by geostationary satellite beacons (nominally 11.7 GHz). Choosing a high order filter with a large slope at its upper band edge would be desirable from this standpoint. However this must also be weighed against the associated increase in sensitivity of the filter phase response with temperature (D'Addario, 2003). For now the filter characteristics are left unspecified, since determining them will likely require some experimentation and study of the RFI environment.

The next elements along the signal chain are digital attenuators paired with power detectors. Given the likely presence of strong RFI, the purpose of the attenuators will be to protect downstream amplifiers from saturation given a certain threshold power reading from the detectors. This may be implemented either manually or through an automatic level control loop, and in the case of the latter the attenuator setting must be monitored by backend system to ensure proper scaling and calibration of the data. Control and monitoring of the digital attenuators and detectors can be accomplished via the backend's general purpose input/output (GPIO) bus. The cryogenic LNAs will of course remain unprotected, but this is a necessary trade-off to maintain overall system sensitivity.

After a second stage of ambient temperature amplifiers, all signal channels are mixed with an LO signal derived from a single LO frequency synthesizer (either LO1A or LO1B). This is accomplished by a central two-way power divider to distribute the LO to the test and reference receivers followed by two additional power dividers located at each receiver to distribute the LO to the separate polarization channels. This is done in order to mitigate phase noise which would result from having two or more frequency synthesizers or phase-locked oscillators driving each of the separate mixers.

For astronomical sources with a broadband, nominally blackbody emission spectrum, the LO will be tuned such that the nominal 1 GHz bandwidth falls within the upper sideband of the LO and gets downconverted to a nominal IF center frequency of 750 MHz. The low pass filters (LPF) following the mixers are meant to eliminate the other sideband and any additional unwanted harmonics. Here, it is assumed that the ADCs in the backend have a sample rate of 3 GSps, and in this case a 750 MHz IF center frequency allows adequate frequency buffer at both the lower and upper end of the first Nyquist zone to prevent aliasing of a 1 GHz signal bandwidth.

At this IF center frequency, the required limit of differential timing jitter for the digital backend would be about 30 ps (i.e. the jitter in clock skew between test and reference signals; see Section A.4), but this could be relaxed somewhat by biasing the IF center frequency lower.

However, biasing the IF center frequency too low would degrade image rejection, and so we will assume the optimum value is nominally 750 MHz. A wideband bandpass filter (WBF) will provide additional filtering and further define the IF bandpass, and a final amplifier stage will provide any additional gain required to drive the ADCs in the backend.

Using the backend GPIO interface, each of the WBFs may be toggled to one of two alternate narrowband bandpass filters (NBF1 or NBF2), which are meant to define the IF bandpass for those cases where a narrowband signal such as that from a satellite beacon is used for the holography measurement. The nominal bandwidths of these filters will be 10 and 100 kHz, corresponding to the two available bandwidth settings for the current holography system. The larger of these two bandwidths will allow for the use of satellite downlinks which also include sidebands in addition to a central tone. For both cases, it will be advantageous to tune the LO such that the IF center frequency is half the nominal bandwidth (either 5 or 50 kHz), since the image rejection considerations should not be at play for a tone-like signal and the temperature sensitivity of the NBF phase response would decrease as a result of its lower Q-factor.

4.2 Special design considerations for the analog front end

Assuming proper steps are taken to reduce loss in the earliest stages of the front end electronics and waveguide components, meeting the sensitivity requirements should be more or less straightforward. However, there are other considerations at play for the front end. As explained in D'Addario (1982), measuring the phase of the GBT's antenna aperture field to high precision corresponds to a high degree of required dynamic range in the measurement of its farfield pattern. As mentioned in Hunter et al. (2011), the required dynamic range for a 100 µm measurement uncertainty is about 70 dB, and since we require similar or better uncertainty for the new system, we must ensure that the new front end electronics achieve this specification as well. The programmable attenuators mentioned above will be important in this regard, but careful selection of amplifiers and double- or triple-balanced mixers will still be necessary in any case.

Another important consideration is the need to match the instrumental responses between channels corresponding to the same polarization but different antenna. In the ideal case, which is what has been assumed in the sensitivity analysis carried out in Appendix A, the net amplitude and phase response due to all components preceding the correlator are identical (up to a time delay), whereas any mismatch in component responses will result in a loss of coherence and a corresponding reduction in signal-to-noise ratio in the measurement. Constraints on these deviations have been given for the cases of 1% and 0.2% maximum reduction in signal-to-noise ratio (or gain) in Table 1 of D'Addario (2003), which we reproduce here in Table 1:

As in Section A.4, a 1% limit to loss of coherence has generally been applied to individual sources of error in this conceptual design, and so the corresponding guidelines given in the table will likely be followed. However, if it is found that more stringent specifications on mismatch errors must be followed, this will likely add to the overall cost of the front end system, as a larger sample of components will need to be tested in order to select the ones that meet the matching specifications.

One caveat with this is that there is at least one pair of the components in the system

Type of mismatch	1% maximum gain error	0.2% maximum gain error
Amplitude slope (edge to edge)	2.7 dB	1.2 dB
Sinusoidal ripple (peak to peak)	1.5 dB	0.75 dB
Center frequency displacement	0.007 B	0.001 B
Phase variation (random, rms)	9.1°	4.0°

Table 1: Limits to bandpass mismatch errors between pairs of signals to be correlated (D'Addario, 2003). Here, B is the signal bandwidth.

which likely cannot be matched, and these are the feeds. Because they will have different illumination patterns, one matched to the GBT subreflector and the other matched to the subreflector of the Cassegrain reference antenna, their phase and amplitude response across the signal bandwidth may exceed the specifications given in Table 1. However, for a small fractional bandwidth it may be possible to approximate these effects as an effective propagation delay, which can be easily compensated for by suitably sizing the lengths of interconnecting cables. The use of analog or digital equalization filters may be used in the event that this approximation is invalid.

Finally, one must also consider the effects of temperature instability, particularly for those cases where the required integration time is on the order of a few seconds or more. This has already been discussed above with respect to the selection of filters, which may be among some of the more susceptible components when the number of poles becomes large. Temperature-induced gain instability in the amplifiers will be another concern. Selecting components according to low temperature sensitivity will be one way to mitigate errors, but active or passive temperature stabilization of the electronics and the surrounding chassis may be required as well. This will be particularly important for the reference receiver, which is more exposed to the elements. In the current holography system, temperature stabilization of the reference receiver is already implemented using a custom-built temperature controller, and it may be possible to re-use some of this existing equipment and infrastructure.

Temperature stabilization of the cables leading to the reference antenna will be important as well, particularly for the new system in which the LO is distributed to each of the receivers at or near Ku-band. As mentioned above, a low-side LO injection scheme is proposed for the mixing stage, and this is to reduce the required LO frequency and corresponding phase instability. In the current holography system, passive temperature stabilization of cables leading to the reference receiver is implemented by running them through conduit, and this too will be re-used in the new system for the same reason.

4.3 Digital backend and correlator

In this section we will specifically discuss the digital backend to the proposed holography system. Its primary function is to cross-correlate the signals in both polarization channels of the test receiver with the corresponding channels in the reference receiver, average the result, and transmit it to a remote host, although it is also capable of interacting with other parts of the system through its GPIO interface (e.g. the digital attenuators mentioned above). The core DSP functions will be implemented on an FPGA. For the present purposes, only a general overview of these DSP functions and other auxiliary features will be given here, but

a more detailed discussion concerning specific hardware implementations and specifications will be saved for a future memo.

The backend shown in Figure 2 is shown in greater detail in Figure 4, including all of the relevant DSP blocks. The four analog signals discussed in the previous section–i.e. two polarization channels for both the test and reference receiver–are each sampled and digitized by four ADC units. The ADC sample rate is to be nominally 3 GSps in order to fully accommodate a 1 GHz bandwidth plus some additional margin to prevent aliasing. The 10 MHz and 1 PPS (pulse-per-second) signals are timing references that are phase locked to the site hydrogen maser, and these are used by the clock generator to generate clock and synchronization pulses for the ADCs and other functions on the FPGA.

The essential DSP functions to be implemented on the FPGA are the following:

- Hilbert transform
- Variable time delay
- Finite impulse response (FIR) filter bank
- Multiplication
- Accumulation/integration
- Packetization

The function of the Hilbert transform is to generate complex samples of the test receiver output with in-phase and quadrature components, which is required to measure the complex beam pattern of the test antenna and in turn compute the aperture field phase. FIR filter implementations of the Hilbert transform have been used previously in digital correlator designs (Savci & Erdoğan, 2019), and in fact some FPGA manufacturers include these within their standard DSP firmware libraries. Alternatively, IQ samplers could be used at the inputs to the backend, allowing this operation to be offloaded from the FPGA.

The variable time delay is meant to compensate for the geometric time delay, which is the propagation time between a given source and the test receiver relative to the propagation time from the same source to the reference receiver. As discussed in Appendix B, this depends both upon the relative separation of the test and reference antennas (i.e. their baseline), as well as their orientation with respect to the line of sight towards the source. Whether the reference antenna is located at ground level or on the GBT structure, the required delay will therefore have a static component as well as a dynamic component as the GBT slews to various offset angles from the source. For the reference antenna's current position, the static component is about 500 ns while the dynamic component varies by about 3 ns per degree elevation offset from the source.

As shown in Section A.1, due to the finite coherence time $\Delta\nu^{-1}$ of a finite bandwidth signal, a static error in delay compensation of as little as 80 ps will result in a 1% loss signal-to-noise ratio at the correlator output for a 1 GHz signal bandwidth. Similarly, in Section A.4 it was shown that an r.m.s. fluctuation in delay compensation of as little as 30 ps will have the same effect. Ideally, the correct delay compensation can be applied given precise surveying of the reference antenna position and real time feedback to the backend of

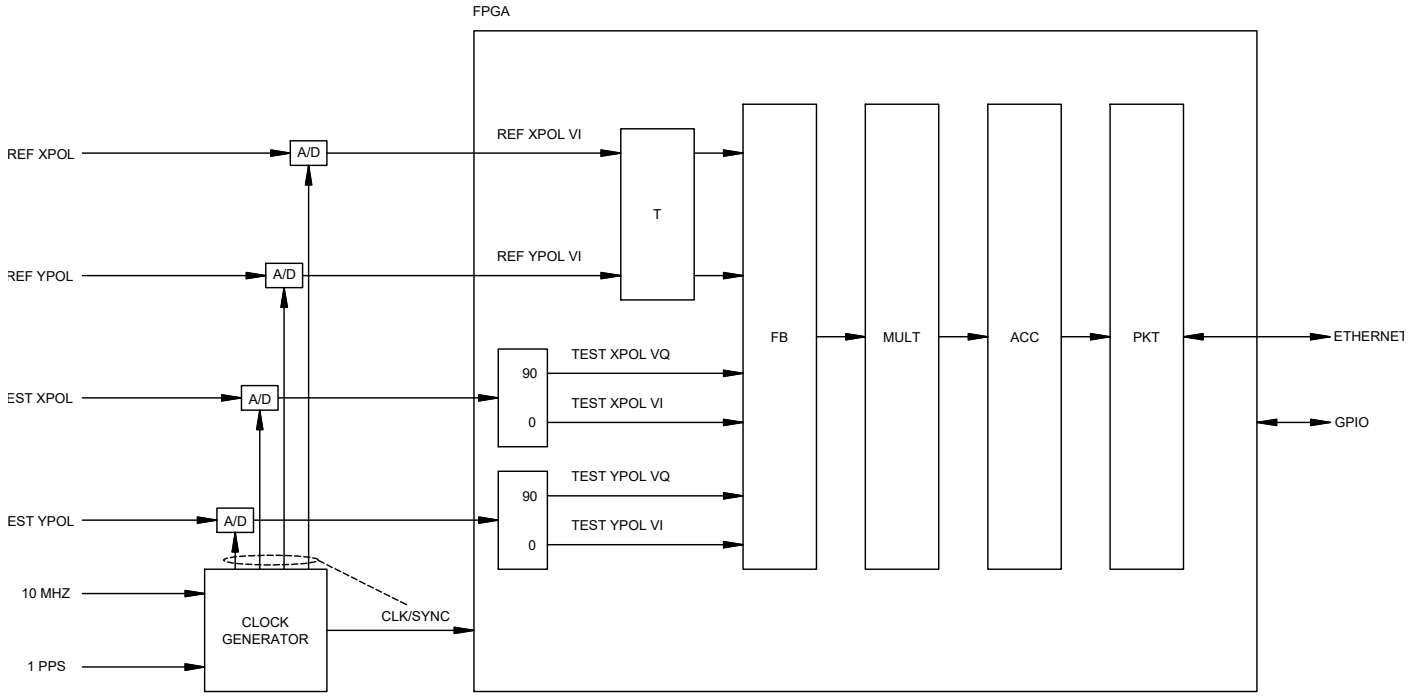

Figure 4: Block diagram for the backend of the proposed holography system. Analog input signals include those shown in Figure 2 from the test and reference receiver as well as 1 PPS (pulse-per-second) and 10 MHz signals which are phase locked to the site maser and provide a stable clock reference and synchronization trigger pulses. DSP blocks within the digital correlator include the Hilbert transform blocks, which convert real samples to complex samples with in-phase and quadrature components, a variable time delay (T), a finite impulse response filter bank (FB), multiply (MULT) and accumulate (ACC) blocks, and finally a packetizer (PKT) for the ethernet interface.

the telescope's orientation with respect to the source, although there are other confounding factors relating to the gravitational deformations of the GBT feed arm which complicate matters (see Section 7.1.1).

Another difficulty relating to the time delay is the fact that the required precision is appreciably smaller than the assumed sample spacing, which for a 3 GSps ADC is 333 ps. Whereas a delay of an integral number of samples can be realized straightforwardly using shift registers, fractional delays are more challenging to implement. An approximate fractional delay can be implemented using an FIR filter (Johansson & Eghbali, 2014), where the accuracy of the approximation and the filter bandwidth generally increase at the cost of increased filter complexity. The fractional delay can also be varied in real-time without introducing transients, as required for accurate delay tracking. Furthermore, such an implementation can also be supplemented with a real-time adjustable phase shift, which can be used to cancel the phase shift resulting from the delayed LO (see the first term in Equation (29) of Section A.1).

The next DSP block is an FIR filter bank. The purpose of this is to subdivide the full signal bandwidth into multiple adjacent, and minimally overlapping sub-bands such that, in the following multiplication block, cross-correlation is performed only between signals that have passed through the same FIR filter. This may partly alleviate the timing requirements described above, for which the maximum delay compensation error scales as the inverse bandwidth of the cross-correlated signals. But its other purpose is to mitigate the "bandwidth-smearing" effect of the measured antenna aperture field, which is summarized in Section 7.1.2 and discussed at greater length in Appendix E.

The multiplication block then is responsible for computing the products just described. To be explicit, with index p denoting polarization, index j denoting one of the N filter bank channels, I and Q denoting the in-phase and quadrature components of the test receiver signals, and finally primes denoting reference receiver signals, the multiplication block forms the $4N$ products:

$$v_{x,p,j} = v_{I,p,j} v'_{I,p,j} \tag{1}$$

$$v_{y,p,j} = v_{Q,p,j} v'_{I,p,j} \tag{2}$$

where $v_{x,p,j}$ is the real part of the cross-correlation and $v_{y,p,j}$ is the corresponding imaginary part (here, x and y should not be confused with the polarization, which is indexed by p). In other words, cross-correlation between signals of opposite polarization and different frequency channels are not computed, this being on the basis that they are uncorrelated.

In the current holography system, products such as

$$P = v_I v_Q \tag{3}$$

$$P' = v'_I v'_Q \tag{4}$$

are formed, which are equivalent to the total power from the test and reference receiver, respectively. These are useful diagnostic measures to have at hand, and so it is likely these, too, would be implemented in some form in the new system. However, for simplicity, we have presented only the bare essential components to the correlator for discussion.

The final two DSP blocks shown in Figure 4 are the accumulate block, which is responsible for synchronously averaging each of the cross-correlation products given above. and the

packetizer, which is responsible for packaging the averaged data into an appropriate network protocol format for transmission to a remote host for further data processing. Similarly, configuration information such as integration time and required delay values must also be parsed out from incoming packets. It is conceivable that, before transmission of integrated data, at least some of the computations required to regrid and Fourier transform the correlator data into the required aperture field and surface deformation data will be performed either on the same FPGA or a separate processing unit. However, this possibility will not be explored here.

4.4 Advanced backend development

There are a few DSP functions not included in the working concept shown in Figure 4 that would be potentially useful in the final production version. We mention two of these here only as avenues for future development rather than critical components of the conceptual design. The first of these is the equalization filter, which was mentioned above in relation to compensating for phase and amplitude mismatch between the test and receiver feeds. In general, though, this may potentially be used to equalize the response between test and reference receivers due to any arbitrary component mismatches, which would considerably reduce the difficulty of the initial build and sourcing spares. In principle, this is straightforward to implement if the mismatches are known and stable with time and/or temperature. If not, however, there isn't presently a clear path towards implementation, though little has been done so far to explore this possibility.

In addition to this, digital RFI detection and mitigation would likely prove invaluable given that the new system is designed to operate at or near the satellite downlink bands. Both online, pre-correlation RFI mitigation algorithms such as spectral kurtosis and spectral flatness as well as offline, post-correlator algorithms such as sum threshold have previously been developed for digital correlators for radio astronomy applications (Thompson, 2014; Perez-Portero et al., 2022), although there would undoubtedly be some effort required to incorporate these into the present application.

5 Challenges for hardware development and implementation

In Section 3, the basic hardware specifications for the proposed holography system were laid out. Two of these present particular challenges towards development and implementation: the construction of a minimum 2 meter diameter reference antenna and the cryogenic cooling of both the test and reference receivers. We discuss both of these below.

5.1 The reference antenna

The reference antenna for the proposed holography system is a symmetric paraboloidal reflector with a Cassegrain configuration and a diameter of at least 2 meters, which is a factor of 4.7 larger than the currugated horn currently being used as the reference antenna. This design is principally meant to increase system sensitivity: the large diameter increases the gain

Figure 5: Anemometer for weather station #3, located above the subreflector and nearby to the current holography reference antenna, which is shown in the foreground (Credit: Bob Simon)

and radiant flux collected from the source, and, compared to a prime focus configuration, the Cassegrain configuration reduces the amount of spillover noise coupled into the feed from the ground. There is also the additional benefit that the receiver is easier to access and service, and the mechanical loading to the primary reflector is reduced. The latter is particularly important in light of the fact that the receiver will be equipped with cryogenic components. However, the increased diameter brings along with it some additional complications.

The first of these is the practical matter of ensuring the antenna does not obstruct access or other nearby structures and systems. Aside from a light fixture, the nearest of these is the anemometer for weather station #3. It is located a little over 1 meter away towards the direction of the upper elevator (see Figure 5). This is marginally far enough away for a 2 meter diameter antenna. However, it is also clamped to a gimbal mount to allow it to stay vertical as the GBT tips, and so care must be taken to ensure its counterweights do not come into contact with the reference antenna when tipped. On the other hand, it must also be verified that the reference antenna will not compromise the accuracy of the anemometer either. The next nearest point of concern is the air traffic warning light just above the subreflector and approximately 2 meters away from the current reference antenna location. While this is farther away than the anemometer, it must be ensured that the antenna does not violate FAA guidelines by presenting too great a visual obstacle to nearby aircraft [2].

[2] https://www.faa.gov/documentLibrary/media/Advisory_Circular/AC_70_7460-1L_.pdf

While the above considerations do not appear insurmountable, the situation would become increasingly difficult to manage should it turn out that a reference antenna much larger than 2 meters is required. Other options for mounting it to the structure may be available, but it is possible the only alternative would be to locate it at ground level. This would considerably simplify installation, access, and maintenance, but this is not without its drawbacks. Ensuring that the GBT does not shadow the reference antenna requires locating the reference antenna at some considerable distance, relinquishing certain parts of the sky for holography measurements, or constructing a pair of reference antennas that could be alternately used given the desired source. The first of these options would likely degrade the overall performance of the holography system, since phase instability due to atmospheric turbulence and differential expansion in cables generally increases with increasing antenna separation. Based on the currently observed phase instability, which may largely be due to atmospheric turbulence, limiting the antenna spacing to about 140 m should limit the loss of signal-to-noise ratio to about 1% (see Section A.4).

The final implication of the increased antenna diameter is that the beamwidth will be reduced by the same factor. And since the source must remain on-axis with the main beam of the reference antenna for the duration of a holography measurement, it may no longer be adequate to have the reference antenna fixed in position as it is currently. But this depends on a couple of factors. For one thing, it will depend on the maximum offset angle from the source for which the GBT farfield pattern is measured, which in turn depends on the required spatial resolution in the aperture plane. For the low resolution use case described in Section 2, the spatial resolution is $\Delta x = D/15 = 6.67$ m, and the corresponding maximum angular offset from the source is about 0.1° at Ku-band. This is about 0.06 beamwidths for the current reference antenna and 0.3 beamwidths for the new reference antenna, assuming a 2 meter diameter. However, in those cases where high spatial resolution is required (such as when locating faulty actuators), the maximum angular offset will typically be about 1°. This is 0.3 beamwidths for the current reference antenna and 1.4 beamwidths for the new reference antenna. On this basis, it is therefore not adequate to have the reference antenna fixed, at least for those cases where the required spatial resolution is less than a few meters.

An additional factor one must consider is the effect of feed arm flexure. For the most part, this was not relevant to the current holography system since good alignment of the reference antenna needed to be ensured only for a few telescope elevations corresponding to geostationary satellites. But for astronomical sources distributed throughout the sky, the orientation of the reference antenna with respect to the axis of the GBT and the source direction may change substantially for objects located near the horizon versus those located at zenith. In Section D.5 the GBT finite element model was used to predict the location and orientation of the reference antenna as a function of telescope elevation. In Table 7 it is shown that, between horizon and zenith, the reference antenna's tilt in the elevation direction will change by as much as 0.28°, which is about 0.4 beamwidths for the new reference antenna. This is a significant contribution, and it assumes no additional flexure occurs in the reference antenna structure itself.

These results indicate that if the new holography system must adequately perform for all telescope elevations and at the highest required spatial resolutions, it must also be equipped with motorized control with sufficient pointing accuracy, or about $0.1\lambda/D \sim 0.07^\circ$. This will add to the antenna's size, weight, and overall complexity. Additional development will also

need to occur to mitigate the RFI emissions from the motor, develop a pointing model to maintain the required pointing accuracy, and create software resources for interacting with the motor driver. However, it may be sufficient in the early prototyping stage to do without the motor control, since for low resolution holography measurements a fixed mounting scheme appears to be adequate.

5.2 Cryogenics

As discussed in Section 3 and Appendix A, cryogenic front ends for the test and reference receivers are required to ensure adequate system sensitivity. Actually implementing this, however, will be challenging for both receivers. In the case of the reference receiver, the chief obstacle is the limited available helium flow capacity from the prime focus helium lines. For the test receiver, the chief obstacle is the additional requirement to permanently install it at or near the GBT's Gregorian focus. We will address the situation with the reference receiver first.

5.2.1 Reference receiver cryogenics

Currently, no helium lines have been plumbed in for cryogenics at the current reference antenna location, and the nearest place a set of new lines could be added is a manifold near the prime focus boom. About 30' of hard piping would be required for the supply and return lines together, and there may be some spare piping available from the original GBT construction. However, there are few, if any shutoff valves in the helium lines leading to the GBT compressors, so adding a pair of tees for a new set of lines would require venting the entire length of the lines and later pumping and purging with helium. Altogether, this would amount to several days to a few weeks of work.

Assuming this can be managed, there still remains the issue of sourcing enough helium from the compressor connected to those lines. Table 2 shows the mass flow capacity and horsepower for each of the six helium scroll compressors installed at the GBT in addition to the demand from each of the receivers. At prime focus there are currently two receivers in active use, the prime focus (PF) receiver and the Ultra-Wideband (UWB) receiver. A third proposed receiver, the Advanced L-band Phased Array Camera (ALPACA) would also be installed at prime focus. Assuming the holography receivers could be cooled with a CTI model 350 Gifford-McMahon (GM) refrigerator, which has an estimated mass flow requirement of about 15 scfm, mass flow would be adequate if the PF receiver were installed, marginal for the UWB receiver, and insufficient for the ALPACA receiver.

Nevertheless, this would not make cooling the reference receiver unviable. One alternative option would be to plumb in about 60' of extra length to tap into the helium lines supplying the Gregorian receivers. In particular, compressor 6 typically will supply helium to either the C- or S-band receivers, but rarely both. Tapping into the lines for this compressor would ensure that, under most circumstances, a minimum of about 25 scfm of mass flow would be available, which is sufficient for a model 350 refrigerator. Another alternative would be to cool the reference receiver with a Stirling cryocooler, which requires no external compressor. The primary trade-offs with these refrigerators is that they generally have higher minimum temperature ($\sim$35 K instead of $\sim$15 K) and increased levels of vibration relative to the

Compressor	HP	MF capacity	Receiver	Refrigerator	Total MF requirement
1	7.5	90	PF	1020	35
			UWB	1020 (x2)	70
			ALPACA	1020 (x3)	105
2	5	50	W	350	15
			ARGUS	1020	35
			Ku	350	15
3	6	60	MUSTANG 2	PT	N/A
4	6	60	L	1020	35
			X	350	15
5	6	60	KFPA	350	15
			Ka	1020	35
			Q	1020	35
6	6	60	C	350	15
			S	1020	35

Table 2: Estimated mass flow (MF) capacity and horsepower (HP) versus demand for each of the six GBT helium compressors. Refrigerators are given as CTI model numbers, except for the Mustang 2 receiver, which uses a Cryomech pulse tube (PT) cryocooler (mass flow requirements unknown). Compressor 1 currently may only supply helium to one receiver at a time while the remainder can supply helium to at most two. Units for mass flow are scfm.

GM refrigerators more commonly used on the GBT. One particular Stirling cryocooler from Sunpower, Inc. has already been evaluated by NRAO staff (Norrod, 2008). However, some experimentation would likely still need to be done for this application, and so it would be preferable to still use a GM refrigerator and source helium from one of the Gregorian receiver compressors.

5.2.2 Test receiver cryogenics

The logistics of cooling the test receiver depend largely on where it is to be located, so we turn to this question first. As stated in Section 2, the scientific system requirements for the new holography system specify that the test receiver must be permanently installed at or near the Gregorian focus without taking up its own turret slot. In order to reduce systematic measurement errors as much as possible, it is necessary that the test receiver should be located with its phase center somewhere along the 110" diameter circle where it could be rotated into the Gregorian focus with minimal offset. Since this circle is coplanar with the top of the turret, this would require creating a new turret hole if such a location would lie between the existing Gregorian feeds.

However, very little space is available between the feeds. The largest interval unobstructed by a feed turret plate is to either side of the L-band feed, and it is about 16" wide. But at this location the L-band feed would partly obstruct the test receiver's view of the subreflector. Furthermore, there is structural ribbing and mounted equipment on the underside of the turret and directly below these locations, and so these items would have to be removed and relocated if a new turret hole were made (see Figure 6). Therefore, having

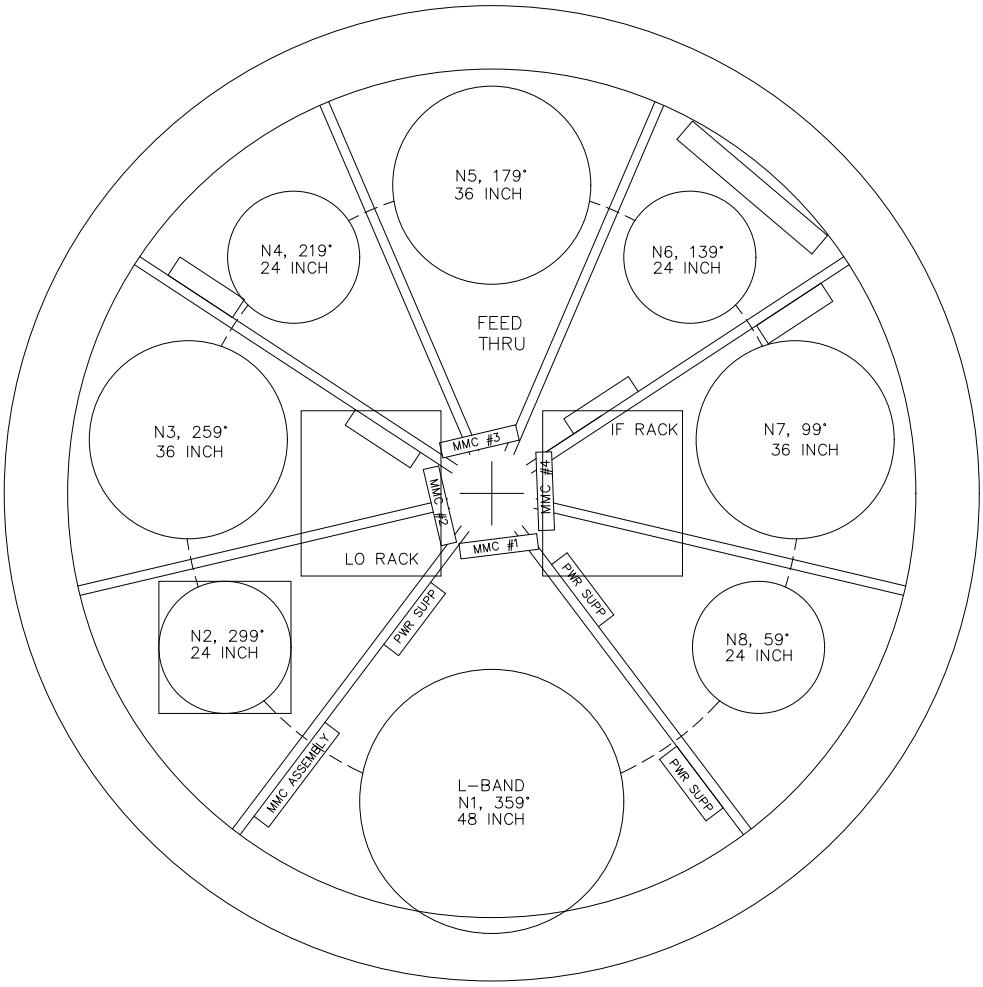

Figure 6: View of GBT turret from underneath (Credit: Bob Simon)

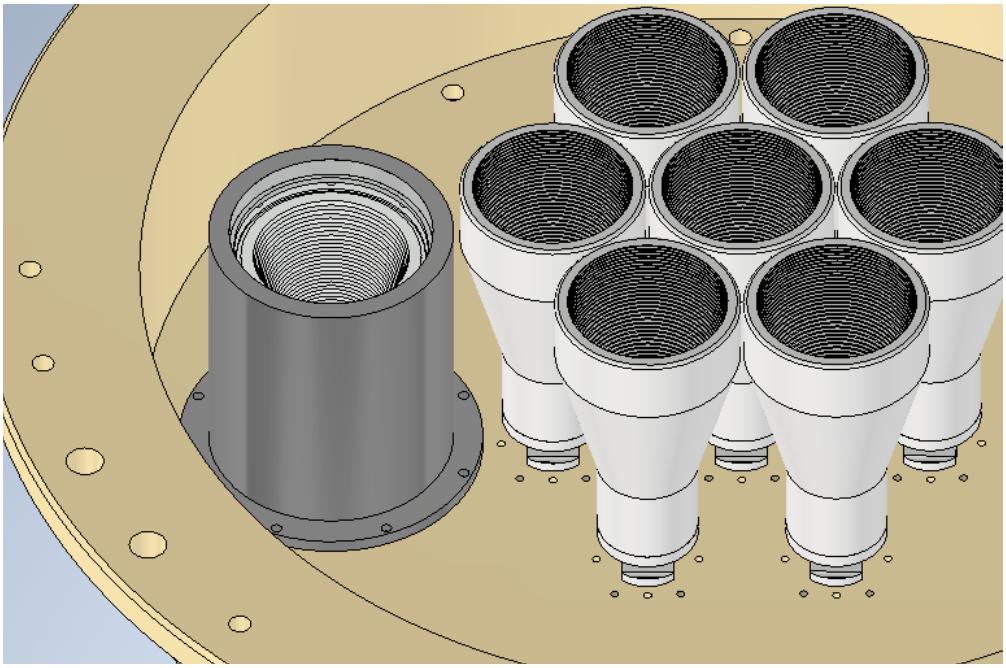

Figure 7: Working concept for incorporating the new holography test receiver into the KFPA dewar. The seven KFPA feeds are shown to the right, while the test receiver feed is on the left, and the surrounding turret hole cover is shown in beige. The feed is surrounded by a metal tube which expands the vacuum space upward and around the feed so that it can be cryogenically cooled. A foam window is shown clear on top for visualization purposes.

the test receiver share a turret slot with another receiver that is infrequently removed is the most viable option. Both the ARGUS receiver and the KFPA satisfy this criterion while also offering fairly little in the way of obstructions to the test feed, and between these two it turns out that the KFPA is more readily modified to incorporate an additional receiver inside its dewar. We show a working concept of the modification in Figures 7 and 8.

In this working concept, we use the exact model for the current test feed with the expectation that it may be re-used for the new holography system or the new feed will be of a similar size. A hole is added to the receiver's turret hole cover to allow the feed to pass through from the vacuum space below and be located at the plane coinciding with the Gregorian focus. In order that the feed may be cooled, it is attached to the top plate via a low thermal conductivity G10 tube, and a metal cap with a foam window is placed over the hole and the feed to seal the vacuum space. The waveguide components attached to the feed occupy the vacuum space below the turret plate, and are thermally linked to nearby cold plates via copper straps. The minimum required modifications in this design are the additional cap, a new turret hole cover, a new upper dewar cylinder, and additional feedthroughs for RF and biasing signals at the bottom section of the dewar. In this arrangement, a $\sim 7.9^\circ$ rotation of the turret would be required to put the test receiver into focus from the KFPA. This would require an additional hole to be made for the turret stow pin as well as any required software modifications to allow for an additional angular stow position for the turret.

With a working proof-of-concept that the test receiver can at least fit inside the modified

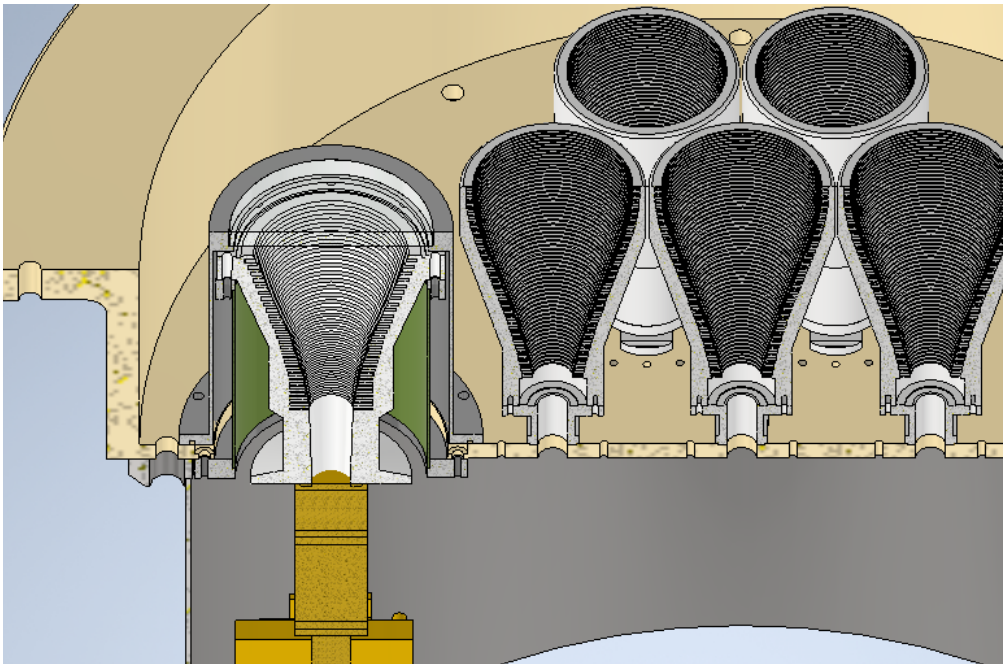

Figure 8: Same as Figure 7 but showing a cutaway view of how the test receiver is supported and the construction of the dewar extension. The green cylinder is a low thermal conductivity, G10 mechanical support for the feed, and the components hanging below the feed are a mock-up of the OMT, isolators, and LNAs depicted schematically in Figure 2

KFPA dewar, the only other issue to contend with is ensuring adequate cooling capacity from the shared refrigerator. The KFPA is currently cooled with a CTI model 350 GM refrigerator, and in fact there is only marginal cooling capacity for the KFPA front end alone. It would therefore be beneficial to both receivers if the KFPA refrigerator could be upgraded to a model 1020, assuming that mechanical supports and shielding for the test receiver are carefully designed and do not introduce any excessive heat loading.

6 Software requirements

The added complexity and instrumentation for the new holography system will require a comparable increase in complexity for the associated software. We divide the required new software features into four categories: fixed configuration changes related to permanent alterations to the instrumentation and configuration of the holography system and GBT, tasks associated with the setup and configuration of the holography system immediately preceding a measurement, "online" tasks which occur during a holography measurement, and "offline" tasks associated with post-processing of the holography measurement data. The list is meant only to be a first pass at defining the software requirements, and is not meant to be exhaustive.

6.1 Fixed configuration changes

As may be deduced from the block diagram shown in Figure 2, the new holography system will differ from the current one in terms of its basic signal routing topology. For one thing, because both the test and reference feeds will be dual-polarized, the number of signal channels being routed to the backend doubles from 2 to 4. Secondly, the new system includes only a single downconversion mixing stage fed from a single LO synthesizer, which, depending on the LO router configuration, may be either LO1A or LO1B. All of these changes must be reflected in the `IF Manager` and `standard.cabling` configuration files, including routing information, signal frequency ranges, and sideband types for mixing stages.

Monitor and control functions for the test and reference receiver will also expand somewhat. As with the current system, each signal channel will include a digital attenuator and corresponding power detector with independent monitor and control capabilities. In addition, each channel will require two control bits for toggling between either the wideband filter (WBF) or one of the two narrowband filters (NBF1 or NBF2) shown in Figure 2. Since the front end electronics for both the test and reference receiver will be cryogenically cooled, an expanded suite of sensors will be included with both in order to monitor temperatures at various points in the cold stage (at least two for the first and second stage of the refrigerator) as well as pressure inside the dewar. In the case of the test receiver, some of these readings will be associated with existing sensors for the KFPA receiver. Ambient temperature outside the test and reference receiver dewars will also be monitored.

In the later stages of development for the holography system, the reference antenna will be equipped with a positioner for accurate source tracking. This will likely have its own suite of sensors and control parameters, and so a new manager will need to be developed to interact with these features. Since the pointing of the antenna needs to be accurate to about 0.1° while being mounted to the GBT feed arm (see Section 5.1), a pointing model must be developed which accurately accounts for feed arm flexure and other dynamic structural changes to the GBT. Similar to the GBT pointing model, this may take the form of a set of empirical parameters stored in a database that is readily accessible by the reference antenna manager. Further details on this behavior during a holography measurement are discussed below.

Certain positional information for the test and reference receivers will also need to be stored for use in delay tracking and focusing of the test receiver. Similar to the reference antenna pointing model, a delay tracking model providing required reference signal time delays to the correlator backend as a function of telescope elevation, ambient temperature, etc. will need to be prepared in some form for ready access by the holography backend manager either just prior to or during a measurement sequence (see Section D.5). Regarding the focusing of the test receiver, it will be used at Gregorian focus, but since it will be located at a $\sim 7.9^\circ$ offset position from the center of the KFPA turret slot, the turret must be rotated this additional amount and stowed in order to put it into focus. A new stow position would then have to be added in software.

6.2 Measurement setup

Just prior to a holography measurement, several new configuration steps need to be taken. First of all, it is presumed the user has somehow specified whether the receiver is to operate in wideband or narrowband mode, which will inform the selection between either the WBFs or NBFs. While the GBT is initially tracking the source, a balance routine might also be included to automatically set the adjustable attenuators according to the measured signal level. The FPGA core for the correlator backend will likely have a few modes of operation defined by the parameters of the filter bank DSP block and integration time, and one of these will be selected at this stage. Finally, any initialization operations associated with the reference antenna will be performed, e.g. enabling drive motors for the positioner, and an analogous `AutoPeak` scan to determine local pointing corrections just for the reference antenna.

6.3 Measurement procedures

As with the current holography system, the measurement will likely be conducted as on-the-fly raster scans of the source (either `RALongMap` or `DecLatMap`), and the triggering of data accumulation and integration should occur in the same way it does currently. Throughout the measurement, the reference antenna must continually track the source with sufficient accuracy, and to do this the reference antenna manager must be supplied with real-time pointing corrections or the necessary information for computing these from the reference antenna pointing model. At minimum, this information would include the real-time, actual (not commanded) GBT azimuth and elevation, but it may also include data from the GBT's structural temperature sensors. Similarly, the correlator backend must be supplied with real-time delays from the delay tracking model or the GBT positioning and temperature information necessary to compute the delay at each point in the map. Local pointing corrections for the reference antenna and delays for each point in the map should also be stored in the `FITS` file for the scan for later use during post-processing.

The relaying of data from the correlator backend to the user and other data processing units will function similarly to the way it does currently, but there will be more concurrent data streams. At minimum, this number will double from having both the test and reference receivers be dual polarization, but there may also be an additional factor of a few increase due to the inclusion of a filter bank among the DSP operations performed by the correlator, which will produce several parallel streams of frequency channels. The number of frequency channels will likely be adjustable to within a few operating modes, and so the downstream data acquisition, processing, and user display must be able to handle each of these accordingly.

6.4 Post-processing

In order for the data from the correlator backend to be useful for surface corrections, they must at minimum be regridded to regularly spaced rows and columns and Fourier transformed into a map of the GBT aperture field phase, which in turn must be unwrapped through 2π and scaled appropriately to obtain the surface deformation. Currently, these

steps are initiated by the user through a combination of Python and Mathematica scripts. But since, for most use cases of the new holography system, rapid turnaround time is required between measuring the surface and performing a surface correction, a more automated process is necessary. The likely outcome is that these tasks will be handled by a dedicated FPGA- or GPU-based processing unit downstream of the correlator backend, in which case surface deformation data could be supplied directly to the active surface manager for immediate followup corrections, bypassing the intermediate step of writing to `FITS` files. In this case, `FITS` files would still be written to and stored for later use, but they may be modified to include the computed surface deformation information in addition to the raw correlator data. At this stage, however, the actual implementation for this post-correlator processing unit is still to be determined.

7 Systematic errors

The typical use case for the current holography system has largely been to measure the GBT primary reflector surface with sufficient resolution to adequately locate faulty actuators for eventual replacement. In this case, the amplitude information of a given deformation (size along the parent paraboloid axis) is secondary to where the deformation is located within the aperture plane. Furthermore, much of the low spatial frequency deformation information in the measurement is not used or is even thrown out in the data processing.

The new use case described in Section 2 for the new holography system therefore represents a strong departure from the current one, since not only is the low spatial frequency information to be retained, it must be measured accurately in order to properly set the active surface after the holography measurement. For this reason, it is critically important that systematic measurement errors affecting the measurement accuracy be identified and mitigated. In this section, we identify several potential sources of systematic measurement error, estimate their level of significance, and wherever possible give guidelines on how to mitigate their effect on the measurement accuracy. In general, we will evaluate these based on their corresponding effective surface error defined in Equations (81) and (85) in Section A.3, but since some of these are difficult to quantify with certainty, they will introduce some measure of risk to the success of the new system.

7.1 Errors due to increased bandwidth

Increasing the bandwidth of the holography system is central to achieving the radiometric sensitivity required to measure the GBT surface with weak sources over short time scales. However, this introduces or exacerbates two sources of measurement error: delay tracking errors and bandwidth smearing. The former has been discussed in Section D.5 and the latter in Appendix E. We will summarize these here and also introduce a strategy to mitigate their effects by dividing the system bandwidth into several sub-bands.

7.1.1 Delay tracking errors

Delay tracking relates to the adjustable instrumental delay t_d described in the sensitivity analysis of Section A.1, which in turn corresponds to the variable delay in the digital backend

that was described in Section 4.3. Its purpose is to exactly compensate for the geometric delay t_g, which is the difference in the propagation time from the source to the test antenna relative to the propagation time from the source to the reference antenna. From the optical constants of the GBT and the approximate current location of the reference antenna, it may be determined from Equation (122) that the geometric delay includes both a ~ 500 ns static component as well as a dynamic component that varies by about 3 ns per degree elevation offset from the source.

In Schwab (2008), this was referred to as the geometric phase correction, since for the narrow bandwidth of the current holography system, the geometric delay t_g corresponds to a unique phase delay $\theta_g = 2\pi\nu_0 t_g$. Currently, the geometric phase correction is implemented in post-processing using survey results of the reference antenna position to determine the length and orientation of the baseline with respect to the source direction for all points in the holography map. But this is not possible when the correlated signals have some non-negligible bandwidth $\Delta\nu$, since in this case any uncompensated delay comparable to or larger than the coherence time $\Delta\nu^{-1}$ will result in the signals from the test and reference antennas becoming uncorrelated (see Figure 11). Instead, delay compensation must happen in real time before the test and reference signals are correlated, and from Sections A.1 and A.4, it must be accurate to within 80 ps and stable to within about 30 ps for $\Delta\nu = 1$ GHz (depending on the IF frequency).

For the dynamic component of the geometric delay mentioned above, this is challenging but not insurmountable. The real difficulty is in accounting for the dynamic flexure of the GBT structure, which causes the antenna baseline vector $\vec{b}$ to vary in a nontrivial way. In Section D.5, the GBT finite element model and focus tracking model were used together to estimate the deviation of the geometric delay from its ideal value as a function of elevation, and there it was shown that this was of the order of a few nanoseconds or more.

In principal, these deviations may be directly measured ahead of time by having both the test and reference antenna track a source over a range of elevations while continuously varying the instrumental delay to maximize the correlator output amplitude (i.e. a delay scan analogous to an `AutoPeakFocus` scan). However, depending on how frequently these calibrations occur, this may add significant average overhead to the holography measurements. Furthermore, it assumes these deviations are repeatable. If wind and thermal loading introduce significant, non-repeatable errors to the delay tracking model, some sort of real-time feedback of the structure must be used, such as data from the GBT quadrant detector. In Section A.4 it was shown, for example, that a 1% reduction in correlated signal amplitude would result from random pointing errors of size ~ 33", which is of the same order of magnitude as typical wind-induced pointing errors (Ries, 2009).

7.1.2 Bandwidth smearing

For a finite fractional bandwidth $\delta = \Delta\nu/\nu_0$, the measured test antenna farfield pattern will be a superposition of a continuum of farfield patterns corresponding to different frequencies, and when the result is Fourier transformed to obtain the test antenna aperture field distribution, the result is a radially smeared image of the actual aperture field distribution. As described in Appendix E, this will primarily affect the Zernike decomposition of the measured surface at high radial indices n. Under optimistic condition, i.e. small surface deformations

($\Delta z \ll \lambda$) consisting of Zernike terms with $n < 5$, the effective measurement error will be below the measurement uncertainty for $\delta < 0.2$, which for $\nu_0 = 12$ GHz corresponds to 2.4 GHz. However, it is recommended that some safety factor, say 2, be applied to the maximum instantaneous bandwidth in order to deal with less benign surface deformations. A 1 GHz bandwidth would provide adequate safety maring in this case, but some experimentation may be necessary to determine this factor.

7.1.3 Bandwidth subdivision and phase unwrapping

Both of the systematic errors described above can be at least partly mitigated by subdividing the total system bandwidth into smaller windows using a filter bank and performing cross-correlation only between signals originating from the same sub-band (see Section 4.3). This would then result in a unique aperture field phase distribution for each sub-band, which from (78) could be used to determine the surface deformation using the center wavelength appropriate to each sub-band. The loss of radiometric sensitivity from restricting the bandwidth of each sub-band would then be recovered by averaging the resulting surface deformation measurements from all sub-bands together.

The main issue with this approach is that, in order to compute the surface deformation from the aperture field phase, one must first unwrap the phase through 2π relative to some chosen location in the aperture plane. This is non-trivial to do in two dimensions, though several algorithms do exist and are put into practice with the current holography system (Goldstein et al., 1988; Ghiglia & Pritt, 1998). However, any phase unwrapping algorithm will fail to determine the corresponding deformation given sufficient ambiguity in the aperture field phase map, which fundamentally is related to the r.m.s. phase noise and aliasing due to large aperture plane sample spacing (Spagnolini, 1995).

Sub-dividing the total system bandwidth should therefore proceed only to the extent that the phase noise level in each sub-band will not be degraded to the point that phase unwrapping fails. This threshold will likely take some experimentation to determine. Alternatively, multi-spectral phase unwrapping methods have already been developed in other fields (Burton & Lalor, 1994), and may allow this restriction to be circumvented. However, this has so far not been investigated, and would likely take some effort to implement.

In any case, phase unwrapping errors will still be problematic if the sample spacing in the aperture plane becomes too large or the surface deformation gradients become too great. An example of this can be seen for a one-dimensional uniform phase gradient shown in Figure 9. In Appendix F.2, the typical r.m.s. surface gradients were estimated to be in the range $\sim 160\,\mu\mathrm{m}\cdot\mathrm{m}^{-1}$ irrespective of telescope elevation. At a system operating frequency $\nu_0 = 12$ GHz, this would correspond to aperture field phase gradients of $0.013 \cdot 2\pi\,\mathrm{rad}\cdot\mathrm{m}^{-1}$ or $0.085 \cdot 2\pi$ per Δx for an aperture plane resolution of $\Delta x = D/15 = 6.67$ m. We therefore expect, at least under typical scenarios, phase unwrapping errors will be few, assuming there is sufficient signal-to-noise ratio.

7.2 Dynamic deformations

As discussed in greater length in Appendix D, the GBT beam pattern will undergo small changes over the course of the holography measurement, particularly if it must track a non-

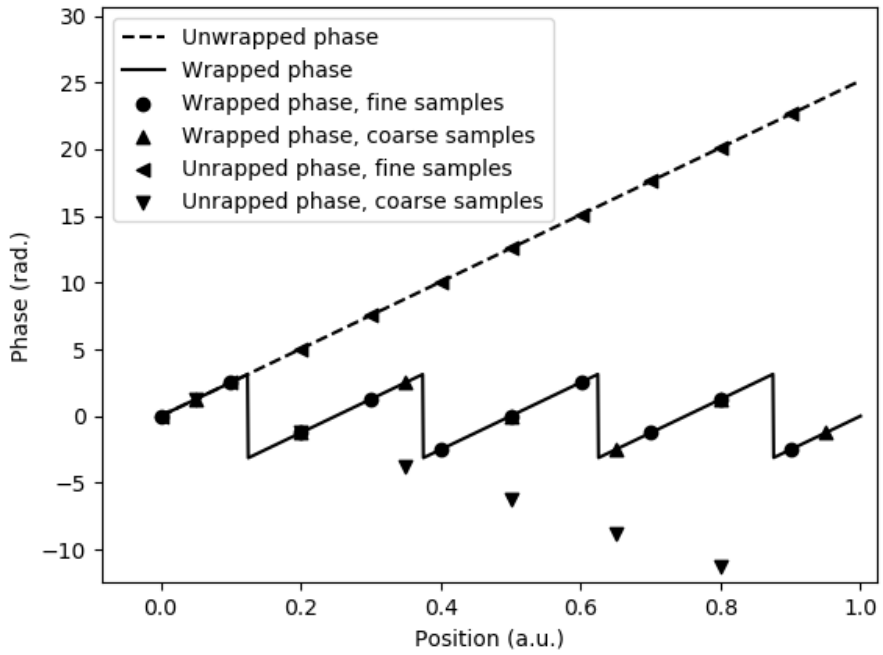

Figure 9: Example of both success and failure to unwrap phase for a uniform phase gradient. Unwrapping the finely spaced samples succeeds because samples are spaced at least twice the spatial frequency of the discontinuities in the wrapped phase, and it fails for coarse sampling because samples are spaced at less than this threshold. The `unwrap` function from the `numpy` Python library was used for unwrapping.

geostationary source. In this case, the Fourier transform relationship between the measured farfield pattern and the aperture field distribution begins to break down. In Appendix D, the effects of dynamic gravitational loading on the primary reflector and feed arm were studied in combination with the associated corrections from the GBT finite element model, Zernike gravity model, and focus tracking model. There it was determined that the dominant surface measurement errors were associated with dynamic deflections of the feed arm, the corrective action of the focus tracking model, and the associated changes in the primary reflector phase distribution. In the worst case (90° telescope elevation), this led to about 15 µm of effective surface measurement error, which is smaller than the required 100 µm surface measurement uncertainty but still approaching a level of significance.

Given that this result neglects pointing corrections and depends strongly on the accuracy of the current GBT finite element model and focus tracking model to predict the actual positions of the GBT optics, some further study will likely be required to ensure these effects can in fact be neglected. Furthermore, dynamic changes to the GBT structure due to wind and thermal loading will also be at play. These are much less repeatable, but some study should be devoted to estimating the magnitude of their effect.

7.3 Aliasing and Gibbs phenomenon

The holography measurement technique relies on the Fourier transform relationship between the antenna's aperture field distribution and its farfield pattern. But since the farfield pattern can only be sampled over a finite angular interval, the aperture field distribution is approximated by the discrete Fourier transform, which will in general introduce errors due to both aliasing and the Gibbs phenomenon. Both of these errors become more acute as the spatial resolution becomes lower, since this corresponds to the farfield pattern being sampled over a smaller domain.

These errors were analyzed in some detail in Appendix F using simple models for the aperture field. There it was determined that for a resolution of $\Delta x = D/15 = 6.67$ m and an operating frequency $\nu_0 = 12$ GHz, surface measurement errors due to aliasing could be maintained below about half the 100 µm required surface measurement uncertainty if the oversampling ratio L/D is set to $\sim$1.2 or larger (L is the size of the aperture field map). The error due to the Gibbs phenomenon also depends strongly on the gradients of the surface deformation (particularly at or near the edge of the aperture). Based on the estimated $\sim$160 µm·m^{-1} residual surface gradients for the GBT primary reflector, the associated error was also estimated to be about half the required surface measurement uncertainty for the same measurement conditions given above.

8 Cost estimate

The new holography system will replace all or most of the components from the current system, but it will also roughly double its size and complexity due to the additional polarization channel for both the test and reference receiver. In Table 3 we provide cost estimates associated with several key components or services. The costing studies on which these estimates are based are preliminary and subject to change as other alternatives are found for certain

components, but they are representative of the key hardware specifications summarized in Section 3. Wherever spare components are deemed necessary and are not already on hand, these are included in the quantity.

Component/service	Unit cost	Qty.	Extended cost
Cryogenic LNAs	6k	4	24k
FPGA backend (with ADC module)	21k[3]	1	21k
Reference antenna (with positioner)	15k	1	15k
Warm RF electronics (1 channel)	1k	12	12k
Cryogenic isolators	2k	4	8k
Rx. support electronics	2k	2	4k
Cryogenic temperature sensors	500	4	2k
OMT	500	2	1k
Reference rx. dewar fabrication	1k	1	1k
KFPA rx. dewar modifications	1k	1	1k
Structural supports, enclosures, etc.	1k	1	1k
Total			90k

Table 3: Cost estimates for various components of the new holography system

9 Development timeline

Development of the new holography system will be divided into several phases. The first phase of development will attempt to verify the feasibility of delay tracking at the required level of precision described in Section 7.1.1. The reason it is prioritized to Phase 1 is because (a) this capability is critical to the performance of the new system, (b) the analysis of Section D.5 demonstrated that dynamic deformations of the GBT structure, which are currently not well understood, may have a significant impact, and (c) feasibility can be assessed using the current system. The procedure for doing this would consist of performing several tracking scans of a strong non-geostationary source (e.g. Venus) over several elevations, measuring any deviations of the geometric delay/phase from what is expected in absence of dynamic structural deformations, and repeating measurements over several different wind and thermal loading conditions to assess repeatability. Assuming these results bode well, development would proceed to Phase 2.

Phase 2 consists generally of more detailed system design; component selection, sourcing, and fabrication; and unit testing in the lab. Proposed modifications to the KFPA will be delayed until later, and so a standalone prototype dewar for the test receiver will be constructed solely for preliminary testing. Part of this development may proceed in parallel with Phase 1 assuming proper staff resources are allocated and minimal engineering support is required for the latter. In the later parts of this phase, it is assumed that all parts of the system except possibly the backend will be available for unit testing. If software resources

[3]Incorporating FPGA development into a student project would allow the FPGA board to be purchased under an educational discount. This cost reflects an educational discount applied to the purchase of a ROACH-2 board

are available, some initial development for the reference antenna manager would be useful, but this is not necessarily required.

Phase 3 consists primarily of backend development. At this stage, all of the critical DSP elements will be designed and tested, while more advanced functionality such as RFI detection and mitigation will be saved for future development. If this is conducted as a summer student project, this could proceed in parallel with Phase 2, and would also qualify the purchase of the FPGA hardware for an educational discount (see footnote to Table 3). Software development for the backend manager should also proceed in parallel.

It will be assumed that during Phase 4 all key components and software are available for system level testing in the lab. Important figures of merit such as phase stability, receiver noise temperature, correlator sensitivity, and delay tracking precision will be assessed and compared with predictions. An initial assessment of the impact of RFI will also be possible at this stage.

Assuming the system behaves as expected during lab testing, it will then be installed on the GBT for Phase 5 testing. Included in the installation will be the plumbing in of cryogenic lines to the reference receiver location and modification of the receiver room turret to allow stowing at the offset position of the test receiver. Testing will include repeating some of the previous lab measurements but while using astronomical sources. Delay tracking performance of the new system will be compared with that observed for the current system during Phase 1. This will also include the first measurements of the GBT primary reflector with the new system and a verification that it meets the required surface measurement uncertainty and timing requirements given in Section 2. The test receiver will still be in a prototype dewar, which will be installed in its own turret slot during this short period of testing.

Phase 6 represents the final stage of development before system commissioning can take place. The KFPA will be fitted with modified parts to accommodate the test receiver and its refrigerator will be upgraded to a CTI model 1020. Adequate cryogenic performance will be verified in the lab after these modifications have been made and the test receiver installed in the KFPA dewar. If it was determined in the previous two phases that RFI detection and mitigation are required, work would begin at this stage to develop an effective backend solution (e.g. spectral kurtosis or spectral flatness algorithms). If possible, an attempt will be made to leverage previous work in this area by NRAO staff to streamline this effort. In the meantime, all components will be re-installed on the GBT, including the KFPA in preparation for eventual commissioning.

An overview of the required engineering development milestones for each phase is shown in Table 4 along with the corresponding time estimates. The 25 month total development time should be regarded only as a very rough estimate, since it does not take into account opportunities for parallel development or estimates of software development time. Furthermore, much still has to be clarified about the details of the correlator backend and any processing units downstream which transform the correlator data into surface corrections that may be used by the active surface manager. This will be left to a future memo, but in the meantime a 3 year total development time would seem to be an appropriate preliminary estimate at this stage.

Phase	Milestone	Duration
1	Delay tracking feasibility study	1 mo.
2	Component selection and sourcing	2 mo.
	Custom parts design and fabrication	4 mo.
	RF electronics testing	2 mo.
	Cryogenic testing	1 mo.
	Feed pattern measurement	1 mo.
	Reference antenna pointing verification	1 mo.
3	FPGA benchmark verification	1 wk.
	Unit testing of main correlator DSP blocks	1 mo.
	Unit testing of delay tracking	1 mo.
	Unit testing of filter bank	1 mo.
	Unit testing of GPIO interface	1 wk.
	Unit testing of network link	1 wk.
4	Receiver noise temperature measurement	1 wk.
	Correlator phase stability measurement	1 wk.
	Correlator noise measurement	1 wk.
	Delay tracking verification	1 wk.
	RFI impact assessment	2 wk.
5	GBT installation	1 wk.
	GBT cryogenics modifications	2 wk.
	GBT receiver room turret modifications	1 wk.
	Initial on-sky testing	1 wk.
6	KFPA modification	1 wk.
	KFPA cryogenic performance verification	1 wk.
	RFI detection and mitigation development	6 mo.
	Re-installation of KFPA/test receiver on GBT	1 wk.
Total		25 mo.

Table 4: Overview of estimated development timeline for new holography system

10 Conclusion

In this memo we have presented system requirements for a new holography system which would allow measurements of the GBT primary reflector surface to be made using astronomical sources over time scales as short as ~ 10 minutes. This allows surface deformations to be accurately measured and corrected over the full elevation range of the GBT, and it also enables rapid follow-up of scientific observations after the associated surface corrections have been made, thus opening up the possibility of daytime high frequency observing. From an analysis of the sensitivity implications of these requirements, such a system has found to be technically feasible assuming certain key hardware specifications are met. Principle among these are the total instantaneous bandwidth, which will be increased to 1 GHz minimum, the reference antenna diameter, which will be increased to 2 meters minimum, and the receiver noise temperature, which will be in the range of a few Kelvin and will require a cryogenic front end.

Several changes to the holography system bring with them a new assortment of challenges, such as the accurate pointing of the reference antenna and the cryogenic cooling of both the test and reference receiver front ends, and we have presented workable solutions to each case. We have also outlined several of sources of systematic measurement error which could potentially limit the usefulness of the new system. For some of these we have presented straightforward strategies for mitigating their effect, while others will require further study to fully understand and estimate their impact. Finally, we have presented a path forward for addressing these challenges and other required development milestones up to instrument commissioning and regular operational use.

References

Balanis, C. A. 2005, Antenna Theory (New Jersey: Wiley), 799–801

Burton, D. R., & Lalor, M. J. 1994, Appl. Opt., 33, 2939

Constantikes, K. 2003, PTCS Project Note 14.1

—. 2008, PTCS Project Note 53.1

Crane, P. C., & Napier, P. J. 1989, in Synthesis Imaging in Radio Astronomy, ed. R. A. Perley, F. R. Schwab, & A. H. Bridle, Vol. 6 (Astronomical Society of the Pacific), 87–108

D'Addario, L. 1982, Holography Antenna Measurements: further technical considerations, 12 m Millimetre Wave Telescope Memo 202

D'Addario, L. R. 2003, ALMA Memo 452

Ghiglia, D. C., & Pritt, M. D. 1998, Two-Dimensional Phase Unwrapping: Theory, Algorithm, and Software (Wiley)

Goldman, . A. 1997, GBT Memo 165

Goldstein, R. M., Zebker, H. A., & Werner, C. L. 1988, Radio science, 23, 713

Hunter, T. R., Schwab, F. R., White, S. D., et al. 2011, Publications of the Astronomical Society of the Pacific, 123, 1087

Johansson, H., & Eghbali, A. 2014, IEEE Transactions on Circuits and Systems I: Regular Papers, 61, 1355

Lawson, J. L., & Uhlenbeck, G. E. 1950, in Radiation Laboratory Series (McGraw Hill), 68

Lee, S. W. 1988a, in Antenna Handbook, ed. Y. T. Lo & S. W. Lee (Van Nostrand Reinhold), 27–35

—. 1988b, in Antenna Handbook, ed. Y. T. Lo & S. W. Lee (Van Nostrand Reinhold), 13–28

Longhi, P. E., Pace, L., Colangeli, S., Ciccognani, W., & Limiti, E. 2019, Electronics, 8

Maddalena, R. 1991, GBT Memo 68

—. 2014, PTCS Project Note 76.0

Mangum, J., Emerson, D., & Greisen, E. 2007, Astronomy & Astrophysics, 474, 679

Norrod, R. 2008, Electronics Division Internal Report 322

Norrod, R., & Srikanth, S. 1996, GBT Memo 155

Perez-Portero, A., Querol, J., Camps, A., et al. 2022, Remote Sensing, 14, 4672

Prestage, R. M., Constantikes, K. T., Balser, D. S., & Condon, J. J. 2004, in Ground-based Telescopes, Vol. 5489, SPIE, 1029–1040

Ries, P. 2009, PTCS Project Note 68.1

Rusch, W. V. T. 1990, IEEE Trans. Antennas Propag., 38, 1141

Ruze, J. 1966, Proceedings of the IEEE, 54, 633

Savci, K., & Erdoğan, A. Y. 2019, in 2019 Signal Processing Symposium (SPSympo), IEEE, 207–211

Schwab, F. 2008, PTCS Project Note 62

Shore, R. A., & Sletten, C. J. 1988, Reflector and Lens Antennas (Artech House), 36–37

Spagnolini, U. 1995, IEEE Transactions on Geoscience and Remote Sensing, 33, 579

Thomas, B. M. 1971, Proc. IEE, 118

Thompson, A. R., Moran, J. M., & Swenson Jr., G. W. 2017a, Interferometry and Synthesis in Radio Astronomy (Springer), 685–688

—. 2017b, Interferometry and Synthesis in Radio Astronomy (Springer), 240–244

Thompson, M., Marler, F., & Allen, K. 1980, IEEE Transactions on Antennas and Propagation, 28, 278

Thompson, N. C. 2014, PhD thesis, Stellenbosch: Stellenbosch University

Wells, D. 1998, GBT Memo 183

Wells, D., & King, L. 1995a, GBT Memo 124

—. 1995b, GBT Memo 131

Weng, F., Yan, B., & Grody, N. C. 2001, Journal of Geophysical Research: Atmospheres, 106, 20115

White, E., Ghigo, F., Prestage, R., et al. 2022, Astronomy & Astrophysics, 659, A113

White, S. 1993, GBT Memo 101

A Sensitivity analysis

In this section we will derive the uncertainty σ_z in the reflector surface deformation Δz determined from the holography measurement. For simplicity, it will be assumed in the following analysis that the reflector surface is undeformed, while the resulting uncertainty remains approximately valid for cases where Δz is small. A further simplifying assumption worth mentioning at the outset is the quasi-monochromatic approximation, for which the system bandwidth $\Delta\nu$ is assumed small in comparison with its center frequency ν_0. The limits of the quasi-monochromatic approximation are examined in Appendix E.

The following analysis will proceed by deriving the statistical properties of the complex correlator outputs v_x and v_y, which will be shown to be proportional to the farfield pattern of the antenna under test when it and the reference antenna are illuminated from a distant point source. From this we will then derive the statistical properties of the inferred test antenna aperture field, which we take as the discrete Fourier transform (DFT) of the measured test antenna farfield pattern. Finally, we will estimate the measured deformation uncertainty σ_z using the above results and certain key system parameters, e.g. bandwidth, reference antenna diameter, source power flux density, and system noise temperature.

A.1 Statistical properties of the correlator outputs

To begin we consider the simplified block diagram presented in Figure 10. Here, the voltages v_{in} and v'_{in} are, respectively, the voltages developed at the inputs of the test and reference receivers (in general, unprimed quantities will be associated with the test receiver and antenna and primed quantities will refer to the reference receiver and antenna). It is assumed that, while the corresponding test and reference antennas will differ in construction and electrical characteristics, the test and reference receivers are identical in both amplitude and phase response between the input reference plane and the input to the backend. We do, however, allow a phase imbalance $\theta_{LO} = \theta'_{LO} + \Delta\theta_{LO}$ for the LO signal arriving at the two mixers.

The instrumental delays labeled t_d and 90 apply, respectively, an adjustable time delay and a fixed 90° phase shift. The former, as will be described later in this section, is meant to compensate for the inherent propagation delay from the source to the reference plane of the two receivers, while the two 90° phase shifts are required to implement a complex correlator

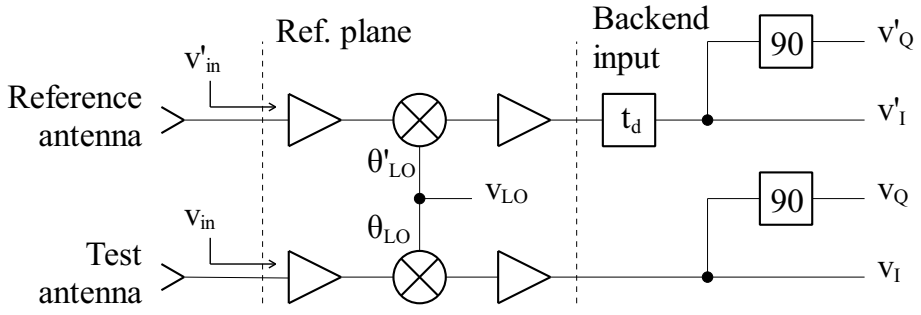

Figure 10: Relevant input and output signals to the test and reference holography receivers

for measuring both magnitude and phase. It is assumed that each of these delays introduces no additional noise to the signal and are implemented after the signals have been digitized, although the latter assumption is not strictly required.

The voltages v_{in} and v'_{in} may be expressed as a sum of correlated components v_s and v'_s due to the observed source and uncorrelated components v_n and v'_n due to finite receiver noise temperature, radiative transfer from the ground and atmosphere, the cosmic microwave background, etc. It is assumed that each of these voltages has the character of Gaussian white noise, and may be expressed as a Fourier series over the time interval $0 \leq t < \tau_0$:

$$v_{in} = v_s + v_n = \mathfrak{Re}\left[\sum_{j=0}^{\infty}(c_{s,j} + c_{n,j})e^{2\pi ijt/\tau_0}\right] \tag{5}$$

where $\mathfrak{Re}$ denotes the real part and the Fourier coefficients $c_{s,j}$ and $c_{n,j}$ are zero mean complex Gaussian random numbers with equal variances along the real and imaginary axes. A similar expression holds for v'_{in} (in the following, unless otherwise stated, expressions related to the reference antenna/receiver can be obtained from those of the test antenna/receiver by adding primes to the relevant quantities).

In the continuum limit (i.e. as the observation time $\tau_0 \to \infty$), we may relate the variances of the uncorrelated Fourier coefficients to the system temperatures T_{sys} and T'_{sys} of the test and reference receivers. For example:

$$\lim_{\tau_0\to\infty} \tau_0\langle|c_{n,j}|^2\rangle = 2 \cdot 4Z_c k_B T_{sys} = 8Z_c k_B T_{sys} \tag{6}$$

where $\langle\,\cdot\,\rangle$ denotes the expectation value, Z_c is the characteristic impedance of the transmission lines at the reference plane, and k_B is Boltzmann's constant. This expression differs from the usual Nyquist-Johnson noise relation by a factor of 2, but this will be canceled when taking the real part in (5).

To determine the variances for the correlated coefficients, we use the reciprocity theorem, which states that the received voltage v_{rx} due to a monochromatic wave with frequency ν is proportional to the incident field amplitude and the antenna farfield pattern evaluated at that same frequency (Lee, 1988a):

$$v_{rx} = C(\nu)F(\nu, \theta, \phi) \tag{7}$$

where θ and ϕ are the spherical coordinates of the source, $C(\nu)$ is proportional to the co-polarized component of the incident field amplitude and $F(\nu, \theta, \phi)$ is the farfield pattern.

In the continuum limit we can apply this theorem to the Fourier coefficients $c_{s,j}$ and $c'_{s,j}$. In particular, when the antennas are pointed at the source, we can relate $c_{s,j}$ and $c'_{s,j}$ to the noise temperatures T_{src} and T'_{src} due to the source:

$$\begin{aligned}\lim_{\tau_0\to\infty} \tau_0\langle|c_{s,j}|^2\rangle &= \lim_{\tau_0\to\infty} \tau_0\langle|C(\nu)|^2\rangle|F(\nu,0,0)|^2 \\ &= 2 \cdot 4Z_c k_B T_{src} \\ &= 8Z_c k_B T_{src}\end{aligned} \tag{8}$$

$$\begin{aligned}\lim_{\tau_0\to\infty} \tau_0\langle|c'_{s,j}|^2\rangle &= \lim_{\tau_0\to\infty} \tau_0\langle|C(\nu)|^2\rangle|F'(\nu,0,0)|^2 \\ &= 2 \cdot 4Z_c k_B T'_{src} \\ &= 8Z_c k_B T'_{src}\end{aligned} \tag{9}$$

As above, the extra factor of 2 will cancel when taking the real part in (5). The antenna temperatures can also be expressed in terms of the antenna effective areas A_e and A'_e and the incident power flux density S. We have for T_{src}:

$$T_{src} = \frac{A_e S}{2k_B}. \tag{10}$$

Here we have assumed that the source is totally unpolarized, which accounts for the factor of 2 in the denominator.

Combining the results above we have:

$$\lim_{\tau_0\to\infty} \tau_0\langle|C(\nu)|^2\rangle = \frac{4Z_c A_e S}{|F(\nu,0,0)|^2} = \frac{4Z_c A'_e S}{|F'(\nu,0,0)|^2} = \frac{4Z_c\sqrt{A_e A'_e}S}{|F(\nu,0,0)||F'(\nu,0,0)|} \tag{11}$$

$$\lim_{\tau_0\to\infty} \tau_0\langle|c_{s,j}|^2\rangle = 4Z_c A_e S\frac{|F(\nu,\theta,\phi)|^2}{|F(\nu,0,0)|^2} \tag{12}$$

$$\lim_{\tau_0\to\infty} \tau_0\langle|c'_{s,j}|^2\rangle = 4Z_c A'_e S\frac{|F'(\nu,\theta,\phi)|^2}{|F'(\nu,0,0)|^2} \tag{13}$$

If both antennas have the same polarization, the Fourier coefficients $c_{s,j}$ and $c'_{s,j}$ will both be proportional to the same field amplitude $C(\nu)$ and will therefore have nonzero covariance:

$$\lim_{\tau_0\to\infty} \tau_0\langle c_{s,j}c'^*_{s,j}\rangle = 4Z_c\sqrt{A_e A'_e}S\frac{F(\nu,\theta,\phi)F'^*(\nu,\theta,\phi)}{|F(\nu,0,0)||F'(\nu,0,0)|} \tag{14}$$

All other Fourier components are assumed to be uncorrelated.

At this stage we will make a further simplification in assuming that the reference antenna either tracks the source or its beam is wide enough that we can approximate its farfield pattern by its on-axis value $F'(\nu,0,0)$. In this case we can re-state (13) and (14):

$$\lim_{\tau_0\to\infty} \tau_0\langle|c'_{s,j}|^2\rangle = 4Z_c A'_e S \tag{15}$$

$$\lim_{\tau_0\to\infty} \tau_0\langle c_{s,j}c'^*_{s,j}\rangle = 4Z_c\sqrt{A_e A'_e}S\frac{F(\nu,\theta,\phi)}{|F(\nu,0,0)|}e^{-i\theta'_F} \tag{16}$$

where θ'_F is the phase of $F'(\nu,0,0)$. Assuming the reference antenna is undeformed and well-focused, the phase θ'_F will be equal to the corresponding geometric phase θ'_g described in Appendix B. If we also separate out the geometric phase factor from the test antenna farfield pattern as $F(\nu,\theta,\phi) = F_0(\nu,\theta,\phi)e^{i\theta_g}$, we may further simplify (12) and (16):

$$\lim_{\tau_0\to\infty} \tau_0\langle|c_{s,j}|^2\rangle = 4Z_c A_e S\frac{|F_0(\nu,\theta,\phi)|^2}{|F_0(\nu,0,0)|^2} \tag{17}$$

$$\lim_{\tau_0\to\infty} \tau_0\langle c_{s,j}c'^*_{s,j}\rangle = 4Z_c\sqrt{A_e A'_e}S\frac{F_0(\nu,\theta,\phi)}{|F_0(\nu,0,0)|}e^{i\Delta\theta_g} \tag{18}$$

where $\Delta\theta_g = \theta_g - \theta'_g$.

With the statistical properties of the input voltages v_{in} and v'_{in} having been established, we can now determine the real and imaginary outputs of the complex correlator, which we define to be:

$$v_x = v_I v'_I \tag{19}$$

$$v_y = v_Q v'_I \tag{20}$$

To do this, we will assume both receivers have a perfectly rectangular bandpass of width $\Delta\nu$ and center frequency ν_0, where the gain within the bandpass is unity:

$$v_I = \mathfrak{Re}\left[\sum_{j=j_{min}}^{j_{max}} (c_{s,j} + c_{n,j}) e^{i[2\pi(\nu_{LO} - j/\tau_0)t - \theta_{LO}]}\right] \tag{21}$$

$$v_Q = \mathfrak{Im}\left[\sum_{j=j_{min}}^{j_{max}} (c_{s,j} + c_{n,j}) e^{i[2\pi(\nu_{LO} - j/\tau_0)t - \theta_{LO}]}\right] \tag{22}$$

$$v'_I = \mathfrak{Re}\left[\sum_{j=j_{min}}^{j_{max}} (c'_{s,j} + c'_{n,j}) e^{i[2\pi(\nu_{LO} - j/\tau_0)(t-t_d) - \theta'_{LO}]}\right] \tag{23}$$

Here, j_{min} and j_{max} define the lower and upper bounds of the rectangular bandpass, ν_{LO} is the LO frequency, θ_{LO} and $\theta'_{LO} = \theta_{LO} - \Delta\theta_{LO}$ are the phases of the LO signal at the test and reference mixer input, and t_d is the instrumental delay applied to the reference receiver output. As shown in Figure 10, the quadrature voltage v_Q is delayed 90° with respect to the in-phase voltage v_I, and this is expressed above by taking the imaginary part rather than the real part. It is assumed that the LO will downconvert the incoming RF signal to a designated IF band (hence the first minus sign in the exponentials) and that the bandpass is so defined such that this does not result in overlap from image frequencies in the IF band (i.e. $\nu_{LO} > j_{max}/\tau_0$ for high side mixing or $\nu_{LO} < j_{min}/\tau_0$ for low side mixing).

From here we may directly compute the expectation value of v_x:

$$\begin{aligned}
\langle v_x \rangle =& \langle v_I v'_I \rangle \\
=& \left\langle \mathfrak{Re}\left\{\sum_{j=j_{min}}^{j_{max}} (c_{s,j} + c_{n,j}) e^{i[2\pi(\nu_{LO} - j/\tau_0)t - \theta_{LO}]}\right\} \right. \\
& \left. \cdot\, \mathfrak{Re}\left\{\sum_{k=k_{min}}^{k_{max}} (c'_{s,k} + c'_{n,k}) e^{i[2\pi(\nu_{LO} - k/\tau_0)(t-t_d) - \theta'_{LO}]}\right\} \right\rangle \\
=& \frac{1}{2}\mathfrak{Re}\left\{\sum_{j=j_{min}}^{j_{max}} \langle c_{s,j} c'^{*}_{s,j} \rangle e^{i[2\pi(\nu_{LO} - j/\tau_0)t_d - \Delta\theta_{LO}]}\right\} \\
=& \frac{1}{2}\mathfrak{Re}\left\{\int_{\nu_{min}}^{\nu_{max}} 4Z_c\sqrt{A_e A'_e} S \frac{F_0(\nu,\theta,\phi)}{|F_0(\nu,0,0)|} e^{i[2\pi(\nu_{LO} - \nu)t_d - \Delta\theta_{LO} + \Delta\theta_g]} d\nu\right\} \\
=& 2Z_c\sqrt{A_e A'_e} S\, \mathfrak{Re}\left\{e^{-i\Delta\theta_{LO}} \int_{\nu_{min}}^{\nu_{max}} \frac{F_0(\nu,\theta,\phi)}{|F_0(\nu,0,0)|} e^{i[2\pi(\nu_{LO} - \nu)t_d + \Delta\theta_g]} d\nu\right\}
\end{aligned} \tag{24}$$

where in the third step all products of uncorrelated Fourier coefficients in the double sum have been excluded, and in the fourth step we have taken the continuum limit and converted

the sum into an integral between $\nu_{min} = \nu_0 - \Delta\nu/2$ and $\nu_{max} = \nu_0 + \Delta\nu/2$. In the last step we have assumed the characteristic impedance Z_c, antenna effective areas A_e and A'_e, and incident power flux density S are all frequency independent.

In Appendix E, it was shown that for small fractional bandwidth (i.e. $\Delta\nu \ll \nu_0$) and small incident angles θ, the antenna farfield pattern is approximately frequency independent, and its value at $\nu = \nu_0$ may be brought out of the integral above. The only remaining frequency dependent term in the integral is then the exponential. As stated earlier, the purpose of the instrumental time delay t_d is to compensate for the geometric phase delay $\Delta\theta_g$ due to the difference in path lengths from the source to the reference plane in the two receivers. If we ignore unequal dispersive effects along the two paths, we can express $\Delta\theta_g$ as:

$$\Delta\theta_g = 2\pi\nu t_g \tag{25}$$

where t_g is the geometric time delay associated with the path length difference. When we adjust t_d to be equal to t_g we obtain:

$$\begin{aligned}
\langle v_x \rangle =& \frac{2Z_c\sqrt{A_e A'_e}S}{|F_0(\nu_0,0,0)|}\,\mathfrak{Re}\left\{e^{-i\Delta\theta_{LO}}F_0(\nu_0,\theta,\phi)\int_{\nu_{min}}^{\nu_{max}} e^{i[2\pi(\nu_{LO}-\nu)t_g+2\pi\nu t_g]}d\nu\right\} \\
=& \frac{2Z_c\sqrt{A_e A'_e}S\Delta\nu}{|F_0(\nu_0,0,0)|}\,\mathfrak{Re}\left\{e^{i(2\pi\nu_{LO}t_d-\Delta\theta_{LO})}F_0(\nu_0,\theta,\phi)\right\} \\
=& 2Z_c\sqrt{A_e A'_e}S\Delta\nu\frac{|F_0(\nu_0,\theta,\phi)|}{|F_0(\nu_0,0,0)|}\cos(2\pi\nu_{LO}t_d - \Delta\theta_{LO} + \theta_F)
\end{aligned} \tag{26}$$

Similarly, we have for $\langle v_y \rangle$:

$$\langle v_y \rangle = 2Z_c\sqrt{A_e A'_e}S\Delta\nu\frac{|F_0(\nu_0,\theta,\phi)|}{|F_0(\nu_0,0,0)|}\sin(2\pi\nu_{LO}t_d - \Delta\theta_{LO} + \theta_F) \tag{27}$$

Thus we see that the correlator output represents a complex voltage with modulus r_c and phase θ_c given by:

$$r_c = 2Z_c\sqrt{A_e A'_e}S\Delta\nu\frac{|F_0(\nu_0,\theta,\phi)|}{|F_0(\nu_0,0,0)|} \tag{28}$$

$$\theta_c = 2\pi\nu_{LO}t_d - \Delta\theta_{LO} + \theta_F \tag{29}$$

Since the instrumental time delay t_d will vary with the source direction over the course of the holography measurement (see (122) in Appendix B), the complex output from the correlator will be proportional to the test antenna farfield pattern $F_0(\nu,\theta,\phi)$ modulated by the geometric phase factor. But since this phase factor is known, it can be canceled either during data acquisition or in post-processing by multiplying the correlator output by the complex conjugate of this phase factor. This of course assumes that $\Delta\theta_{LO}$ and all other phase delays through the receiver elements remain stable for the entirety of the measurement.

Before continuing, it is worthwhile to consider what would happen if there were only partial compensation of the geometric delay with the instrumental delay, i.e. $t_g - t_d = \Delta t_d$. It may be shown that this contributes an additional factor of $\mathrm{sinc}\,\pi\Delta\nu\Delta t_d$ to both $\langle v_x \rangle$ and $\langle v_y \rangle$. In turn, the modulus r_c gets multiplied by the absolute value of this factor (which we plot in Figure 11), while the phase θ_c remains the same as that given by (29). Overall, then, the effect

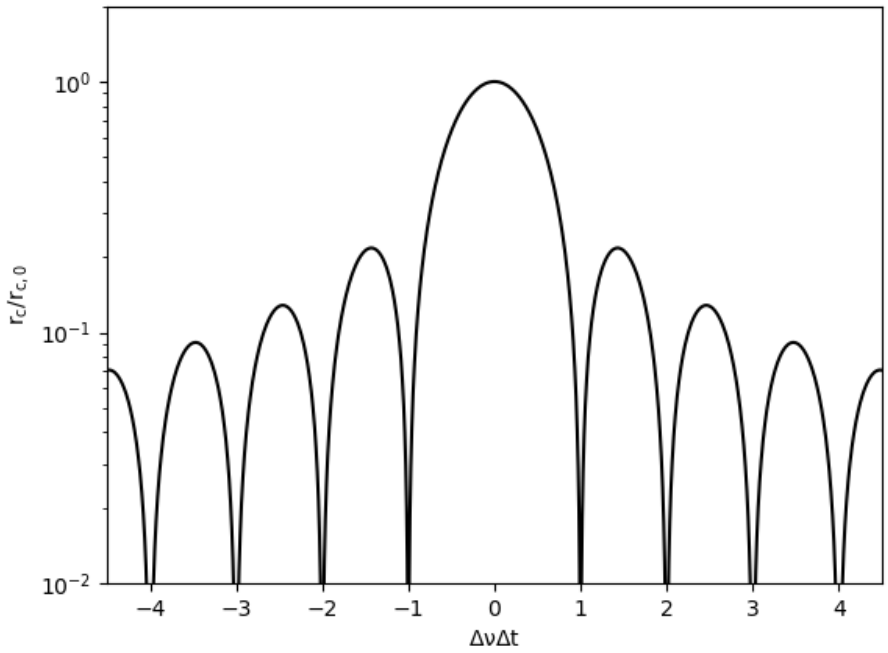

Figure 11: Modulus of complex correlator output versus delay compensation error Δt relative to its value at zero delay compensation error

of the imperfect delay compensation is to reduce the amplitude of the correlator signal, which fundamentally is due to the test and reference signals becoming decorrelated as their relative delay approaches their coherence time $\Delta\nu^{-1}$. When the system bandpass is rectangular as we have assumed here, a 1% reduction in amplitude corresponds to $\Delta\nu\Delta t_d = 0.08$, which for $\Delta\nu = 1$ GHz would correspond to $\Delta t_d = 80$ ps. In Section A.4 we will examine the effect when the delay error Δt_d is not fixed but fluctuates about zero.

Under the assumption of ergodicity, the quantities $\langle v_x \rangle$ and $\langle v_y \rangle$ represent the complex correlator outputs for a fixed source position after an integration time τ approaching infinity. To determine the uncertainty in the measured surface error, we will need to compute the expected variances in these values when the integration time is finite. To do this, we begin by computing the autocorrelation functions $R_x(t - t')$ and $R_y(t - t')$ as well as the cross-correlation function $R_{xy}(t - t')$:

$$R_x(t - t') = \langle v_x(t) v_x(t') \rangle = \langle v_I(t) v'_I(t) v_I(t') v'_I(t') \rangle \tag{30}$$

$$R_y(t - t') = \langle v_y(t) v_y(t') \rangle = \langle v_Q(t) v'_I(t) v_Q(t') v'_I(t') \rangle \tag{31}$$

$$R_{xy}(t - t') = \langle v_x(t) v_y(t') \rangle = \langle v_I(t) v'_I(t) v_Q(t') v'_I(t') \rangle \tag{32}$$

Since all of the voltages in the above expressions are assumed to be zero mean Gaussian random variables, we can use the identity (Lawson & Uhlenbeck, 1950):

$$\langle v_1 v_2 v_3 v_4 \rangle = \langle v_1 v_2 \rangle \langle v_3 v_4 \rangle + \langle v_1 v_3 \rangle \langle v_2 v_4 \rangle + \langle v_1 v_4 \rangle \langle v_2 v_3 \rangle \tag{33}$$

in addition to the variances and covariances derived above in (17), (15), and (18) to obtain the following results:

$$R_x(t-t') = G^2\left[S^2\cos^2\theta_c + \left(S^2 + \frac{ST_{sys}}{K} + \frac{ST'_{sys}}{K'} + \frac{T_{sys}T'_{sys}}{KK'}\right) g_c^2(t-t',0) + S^2 g_c(t-t',\theta_c)g_c(t-t',-\theta_c)\right] \tag{34}$$

$$R_y(t-t') = G^2\left[S^2\sin^2\theta_c + \left(S^2 + \frac{ST_{sys}}{K} + \frac{ST'_{sys}}{K'} + \frac{T_{sys}T'_{sys}}{KK'}\right) g_c^2(t-t',0) - S^2 g_s(t-t',\theta_c)g_s(t-t',-\theta_c)\right] \tag{35}$$

$$R_{xy}(t-t') = G^2\left[\frac{1}{2}S^2\sin(2\theta_c) - \left(S^2 + \frac{ST_{sys}}{K} + \frac{ST'_{sys}}{K'} + \frac{T_{sys}T'_{sys}}{KK'}\right) g_c(t-t',0)g_s(t-t',0) - S^2 g_s(t-t',\theta_c)g_c(t-t',-\theta_c)\right] \tag{36}$$

where we have defined the following terms:

$$G = 4Z_c k_B\sqrt{KK'}\Delta\nu \tag{37}$$

$$K = \frac{A_e}{2k_B}\frac{|F_0(\nu_0,\theta,\phi)|^2}{|F_0(\nu_0,0,0)|^2} \tag{38}$$

$$K' = \frac{A'_e}{2k_B} \tag{39}$$

$$\begin{aligned} g_c(t,\zeta) =& \Delta\nu^{-1}\int_{\nu_{min}}^{\nu_{max}} \cos[2\pi(\nu_{LO}-\nu)t-\zeta]\,d\nu \\ =& \cos[2\pi(\nu_{LO}-\nu_0)t-\zeta]\,\mathrm{sinc}(\pi\Delta\nu t) \end{aligned} \tag{40}$$

$$\begin{aligned} g_s(t,\zeta) =& \Delta\nu^{-1}\int_{\nu_{min}}^{\nu_{max}} \sin[2\pi(\nu_{LO}-\nu)t-\zeta]\,d\nu \\ =& \sin[2\pi(\nu_{LO}-\nu_0)t-\zeta]\,\mathrm{sinc}(\pi\Delta\nu t) \end{aligned} \tag{41}$$

We can now compute the power spectra for v_x and v_y by taking the Fourier transform of the above correlation functions:

$$S_x(\nu) = G^2\left[S^2\cos^2\theta_c\delta(\nu) + \left(S^2 + \frac{ST_{sys}}{K} + \frac{ST'_{sys}}{K'} + \frac{T_{sys}T'_{sys}}{KK'}\right)\Gamma_c(\nu,0) + S^2\Gamma_c(\nu,\theta_c)\right] \tag{42}$$

$$S_y(\nu) = G^2\left[S^2\sin^2\theta_c\delta(\nu) + \left(S^2 + \frac{ST_{sys}}{K} + \frac{ST'_{sys}}{K'} + \frac{T_{sys}T'_{sys}}{KK'}\right)\Gamma_c(\nu,0) - S^2\Gamma_s(\nu,\theta_c)\right] \tag{43}$$

$$S_{xy}(\nu) = G^2\left[\frac{1}{2}S^2\sin(2\theta_c)\delta(\nu) - \left(S^2 + \frac{ST_{sys}}{K} + \frac{ST'_{sys}}{K'} + \frac{T_{sys}T'_{sys}}{KK'}\right)\Gamma_{cs}(\nu,0) - S^2\Gamma_{cs}(\nu,\theta_c)\right] \tag{44}$$

where $\delta(\nu)$ is the Dirac delta function and $\Gamma_c(\nu,\zeta)$, $\Gamma_s(\nu,\zeta)$, and $\Gamma_{cs}(\nu,\zeta)$ are defined as follows:

$$\begin{aligned}\Gamma_c(\nu,\zeta) =& \int_{-\infty}^{\infty} e^{-2\pi i\nu t} g_c(t,\zeta) g_c(t,-\zeta)\, dt \\ =& \frac{1}{4\Delta\nu}\left[\Lambda\left(\frac{\nu+2\nu_{LO}-2\nu_0}{\Delta\nu}\right) + 2\cos(2\zeta)\Lambda\left(\frac{\nu}{\Delta\nu}\right) + \Lambda\left(\frac{\nu-2\nu_{LO}+2\nu_0}{\Delta\nu}\right)\right]\end{aligned} \tag{45}$$

$$\begin{aligned}\Gamma_s(\nu,\zeta) =& \int_{-\infty}^{\infty} e^{-2\pi i\nu t} g_s(t,\zeta) g_s(t,-\zeta)\, dt \\ =& \frac{1}{4\Delta\nu}\left[-\Lambda\left(\frac{\nu+2\nu_{LO}-2\nu_0}{\Delta\nu}\right) + 2\cos(2\zeta)\Lambda\left(\frac{\nu}{\Delta\nu}\right) - \Lambda\left(\frac{\nu-2\nu_{LO}+2\nu_0}{\Delta\nu}\right)\right]\end{aligned} \tag{46}$$

$$\begin{aligned}\Gamma_{cs}(\nu,\zeta) =& \int_{-\infty}^{\infty} e^{-2\pi i\nu t} g_s(t,\zeta) g_c(t,-\zeta)\, dt \\ =& \frac{1}{4\Delta\nu}\left[i\Lambda\left(\frac{\nu+2\nu_{LO}-2\nu_0}{\Delta\nu}\right) - 2\sin(2\zeta)\Lambda\left(\frac{\nu}{\Delta\nu}\right) - i\Lambda\left(\frac{\nu-2\nu_{LO}+2\nu_0}{\Delta\nu}\right)\right]\end{aligned} \tag{47}$$

$$\Lambda(x) = \begin{cases} 1-|x| & |x| \le 1 \\ 0 & |x| > 1 \end{cases} \tag{48}$$

We can incorporate the effect of averaging the correlator outputs v_x and v_y by multiplying their corresponding power spectra by the square of the response $H_\tau(\nu)$ of a low pass filter with characteristic time constant τ. We will assume the response is that of an ideal integrator:

$$|H_\tau(\nu)|^2 = \left|\frac{1}{\tau}\int_{-\tau/2}^{\tau/2} e^{-2\pi i\nu t}\, dt\right|^2 = \mathrm{sinc}^2(\pi\nu\tau) \tag{49}$$

The variance in the time averaged v_x and v_y will then be given by:

$$\begin{aligned}(\Delta v_x)^2 =& \int_{-\infty}^{\infty} \left[S_x(\nu) - \langle v_x\rangle^2\right] |H_\tau(\nu)|^2\, d\nu \\ \approx& \left[S_x(\nu) - \langle v_x\rangle^2\right]_{\nu=0} \int_{-\infty}^{\infty} |H_\tau(\nu)|^2\, d\nu \\ \approx& \frac{G^2}{2\Delta\nu\tau}\left[(1+\cos 2\theta_c)S^2 + \frac{ST_{sys}}{K} + \frac{ST'_{sys}}{K'} + \frac{T_{sys}T'_{sys}}{KK'}\right]\end{aligned} \tag{50}$$

$$\begin{aligned}(\Delta v_y)^2 =& \int_{-\infty}^{\infty} \left[S_y(\nu) - \langle v_y\rangle^2\right] |H_\tau(\nu)|^2\, d\nu \\ \approx& \left[S_y(\nu) - \langle v_y\rangle^2\right]_{\nu=0} \int_{-\infty}^{\infty} |H_\tau(\nu)|^2\, d\nu \\ \approx& \frac{G^2}{2\Delta\nu\tau}\left[(1-\cos 2\theta_c)S^2 + \frac{ST_{sys}}{K} + \frac{ST'_{sys}}{K'} + \frac{T_{sys}T'_{sys}}{KK'}\right]\end{aligned} \tag{51}$$

where in the second lines we have assumed that the bandwidth of the low pass filter is narrow enough that $[S_x(\nu) - \langle v_x\rangle^2]$ and $[S_y(\nu) - \langle v_y\rangle^2]$ are approximately constant in that interval

and can be brought out of the integral as their values evaluated at $\nu = 0$. Similarly, for the covariance we have:

$$\begin{aligned}\mathrm{cov}(v_x, v_y) &= \int_{-\infty}^{\infty} \left[S_{xy}(\nu) - \langle v_x \rangle \langle v_y \rangle\right] |H_\tau(\nu)|^2 \, d\nu \\ &\approx \left[S_{xy}(\nu) - \langle v_x \rangle \langle v_y \rangle\right]_{\nu=0} \int_{-\infty}^{\infty} |H_\tau(\nu)|^2 \, d\nu \\ &\approx \frac{G^2 S^2 \sin 2\theta_c}{2\Delta\nu\tau}\end{aligned} \tag{52}$$

The associated covariance matrix is given by:

$$\Sigma = \begin{bmatrix} \sigma_0^2 + \sigma'^2 \cos^2\theta_c & \sigma'^2 \cos\theta_c \sin\theta_c \\ \sigma'^2 \cos\theta_c \sin\theta_c & \sigma_0^2 + \sigma'^2 \sin^2\theta_c \end{bmatrix} \tag{53}$$

$$\sigma_0^2 = \frac{G^2}{2\Delta\nu\tau} \left(\frac{ST_{sys}}{K} + \frac{ST'_{sys}}{K'} + \frac{T_{sys}T'_{sys}}{KK'} \right) \tag{54}$$

$$\sigma'^2 = \frac{G^2 S^2}{\Delta\nu\tau} \tag{55}$$

Its eigenvalues and eigenvectors are given by:

$$\sigma_u^2 = \sigma_0^2 + \sigma'^2 = \frac{G^2}{2\Delta\nu\tau} \left(2S^2 + \frac{ST_{sys}}{K} + \frac{ST'_{sys}}{K'} + \frac{T_{sys}T'_{sys}}{KK'} \right) \tag{56}$$

$$\sigma_v^2 = \sigma_0^2 \tag{57}$$

$$\hat{u} = \begin{bmatrix} \cos\theta_c \\ \sin\theta_c \end{bmatrix} \tag{58}$$

$$\hat{v} = \begin{bmatrix} -\sin\theta_c \\ \cos\theta_c \end{bmatrix} \tag{59}$$

Hence, the probability distribution in v_x and v_y, whose centroid is given by (26) and (27), is elongated along the $\hat{u}$ direction, which is oriented at an angle θ_c from the real (v_x) axis. Note that, when both antennas are pointed at the source ($\theta = \phi = 0$) and are arranged such that the geometric time delay t_g is zero, both antenna farfield patterns will be real ($\theta_F = \theta'_F = 0$), then $\theta_c = 0$ and the u axis will coincide with the v_x axis. This is essentially the situation described in Crane & Napier (1989) for the case of a tracking, two-element interferometer, and the variance in the real part of the correlator output determined there agrees with that given in (56) above.

A.2 Statistical properties of the measured antenna aperture field

All that remains at this stage is to determine the mean and variances in the test antenna aperture field, which is proportional to the Fourier transform of the collection of measurements $\{v_{x,jk}, v_{y,jk}\}$ made over an appropriate grid of pointings $\{\theta_{jk}, \phi_{jk}\}$ about the source. We will

begin by computing the expectation value for the estimate of the test antenna aperture field, which we take to be the DFT of N^2 farfield pattern measurements $\{v_{x,jk}, v_{y,jk}\}$:

$$\tilde{E}_{R,jk} = \mathfrak{Re}\left\{\sum_{l,m=0}^{N-1} v_{z,lm} e^{-2\pi i(jl+km)/N^2}\right\} \tag{60}$$

$$\tilde{E}_{I,jk} = \mathfrak{Im}\left\{\sum_{l,m=0}^{N-1} v_{z,lm} e^{-2\pi i(jl+km)/N^2}\right\} \tag{61}$$

where we have defined $v_{z,lm} = v_{x,lm} + iv_{y,lm}$ and $\tilde{E}_{R,i}$ and $\tilde{E}_{I,i}$ are the respective real and imaginary parts of the aperture field estimate at location $\vec{\rho}_{jk} = j\Delta x\,\hat{x} + k\Delta x\,\hat{y}$, where Δx is the aperture plane grid spacing determined from the angular size of the measured farfield pattern. We will first compute the expectation value of $\tilde{E}_{R,jk}$ and $\tilde{E}_{I,jk}$ using (26) and (27):

$$\begin{aligned}\langle\tilde{E}_{R,jk}\rangle =& \mathfrak{Re}\left\{\sum_{l,m=0}^{N-1} \langle v_{x,lm} + iv_{y,lm}\rangle e^{-2\pi i(jl+km)/N^2}\right\} \\ =& \frac{2Z_c\sqrt{A_e A'_e}S\Delta\nu}{|F_0(\nu_0,0,0)|}\mathfrak{Re}\left\{\sum_{l,m=0}^{N-1} |F_{0,lm}|e^{i\theta_{F,lm}} e^{-2\pi i(jl+km)/N^2}\right\}\end{aligned} \tag{62}$$

$$\begin{aligned}\langle\tilde{E}_{I,jk}\rangle =& \mathfrak{Im}\left\{\sum_{l,m=0}^{N-1} \langle v_{x,lm} + iv_{y,lm}\rangle e^{-2\pi i(jl+km)/N^2}\right\} \\ =& \frac{2Z_c\sqrt{A_e A'_e}S\Delta\nu}{|F_0(\nu_0,0,0)|}\mathfrak{Im}\left\{\sum_{l,m=0}^{N-1} |F_{0,lm}|e^{i\theta_{F,lm}} e^{-2\pi i(jl+km)/N^2}\right\}\end{aligned} \tag{63}$$

where we have used the abbreviation:

$$F_{0,lm} = F_0(\nu_0, \theta_{lm}, \phi_{lm}) \tag{64}$$

$$\theta_{F,lm} = \theta_F(\theta_{lm}, \phi_{lm}) \tag{65}$$

and assumed that the phase angle θ_c of the correlator outputs v_x and v_y have been compensated for the offset from θ_F described above in (29).

The above result would be proportional to the antenna aperture field in the limit $\Delta x \to 0$, but since the measurement consists only of a finite sampling of the farfield pattern, the DFT above can only represent an estimate. In Appendix F it is shown that for small Δx the DFT of the farfield pattern is approximately equal to L^2 times the actual aperture field, where $L = N\Delta x$. We will assume this is the case and proceed with the model aperture field described in Appendix B, where the test antenna representing the GBT is undeformed and the Gregorian feed illumination has the raised cosine form given in (101). In this case, the aperture field is real and symmetric over the projected aperture, and using (119) we have:

$$E_a = \frac{k_0}{2\pi fM} \cdot \frac{[1-(\rho/2fM)^2]^p}{[1+(\rho/2fM)^2]^{p+1}} \tag{66}$$

where k_0 is the wavevector at the center frequency ν_0, f and M are the respective GBT focal length and magnification, and p is the exponent associated with the raised cosine feed illumination. Substituting $L^2 E_a$ into $\mathfrak{Re}\{\}$ and $\mathfrak{Im}\{\}$ above in (62) and (63) gives:

$$\langle \tilde{E}_{R,jk} \rangle = \frac{2 Z_c \sqrt{A_e A'_e} S \Delta\nu}{|F_0(\nu_0, 0, 0)|} \cdot \frac{k_0 N^2 \Delta x^2}{2\pi f M} \cdot \frac{[1 - (\rho/2fM)^2]^p}{[1 + (\rho/2fM)^2]^{p+1}} \tag{67}$$

$$\langle \tilde{E}_{I,jk} \rangle = 0 \tag{68}$$

where $\tilde{E}_{I,jk}$ evaluates to zero due our assumption that E_a is a purely real quantity. We can also use (119) to compute $|F_0(\nu_0, 0, 0)|$ in the denominator of (62) and (63) above:

$$\begin{aligned} |F_0(\nu_0, 0, 0)| =& \frac{k_0}{2\pi f M} \int_0^{2\pi} \int_0^R \frac{[1 - (\rho/2fM)^2]^p}{[1 + (\rho/2fM)^2]^{p+1}} \, \rho \, d\rho \, d\psi \\ =& \frac{k_0}{fM} \int_0^R \frac{[1 - (\rho/2fM)^2]^p}{[1 + (\rho/2fM)^2]^{p+1}} \, \rho \, d\rho \\ =& 2 k_0 f M \left[B\left(\frac{1}{2}, 1 + p, -p\right) - B\left(\frac{1}{2} - \frac{1}{2}\left(\frac{R}{2fM}\right)^2, 1 + p, -p\right) \right] \end{aligned} \tag{69}$$

where the function $B(z, a, b)$ is defined in (128) and R is the radius of the GBT projected aperture. The effective area A_e of the test antenna will also depend on the model feed illumination, and so we take the associated aperture efficiency η_a to be equal to the product of the illumination and spillover efficiencies given in (126) and (127) in Appendix B. We will take the aperture efficiency of the reference antenna to have a fixed nominal value in the remainder of the analysis.

The above expressions are enough to completely specify the expectation value for the aperture field, and we have only to derive its variance. Before we proceed however, we will simplify the expressions derived earlier for $(\Delta v_x)^2$, $(\Delta v_y)^2$, and $\mathrm{cov}(v_x, v_y)$ by assuming the weak source approximation ($S \ll T_{sys}/K, T'_{sys}/K'$), in which case we can neglect all terms proportional to the power flux density S:

$$(\Delta v_x)^2 \approx \frac{G^2 T_{sys} T'_{sys}}{2 K K' \Delta\nu \tau} = 8 Z_c^2 k_B^2 T_{sys} T'_{sys} \Delta\nu / \tau \tag{70}$$

$$(\Delta v_y)^2 \approx \frac{G^2 T_{sys} T'_{sys}}{2 K K' \Delta\nu \tau} = 8 Z_c^2 k_B^2 T_{sys} T'_{sys} \Delta\nu / \tau \tag{71}$$

$$\mathrm{cov}(v_x, v_y) \approx 0 \tag{72}$$

Hence, in this limit, the probability distribution is symmetric, has zero skewness, and is approximately constant assuming the system temperatures do not vary considerably with θ and ϕ over the course of the holography measurement.

Under this assumption we have for the variance of $\tilde{E}_{R,jk}$:

$$\begin{aligned}(\Delta\tilde{E}_{R,jk})^2 =&\langle\tilde{E}_{R,jk}^2\rangle - \langle\tilde{E}_{R,jk}\rangle^2 \\ =&\sum_{l,m,p,q=0}^{N-1}[\langle(v_{x,lm}\cos\theta_{jk,lm} + v_{y,lm}\sin\theta_{jk,lm})\cdot(v_{x,pq}\cos\theta_{jk,pq} + v_{y,pq}\sin\theta_{jk,pq})\rangle \\ &- \langle v_{x,lm}\cos\theta_{jk,lm} + v_{y,lm}\sin\theta_{jk,lm}\rangle\cdot\langle v_{x,pq}\cos\theta_{jk,pq} + v_{y,pq}\sin\theta_{jk,pq}\rangle] \\ =&\sum_{l,m=0}^{N-1}[(\Delta v_x)^2\cos^2\theta_{jk,lm} + (\Delta v_y)^2\sin^2\theta_{jk,lm}] \\ =&8N^2Z_c^2k_B^2T_{sys}T'_{sys}\Delta\nu/\tau\end{aligned} \tag{73}$$

where in the third step we have assumed statistical independence between different measurements of the farfield pattern (i.e. $\mathrm{cov}(v_{x,jk}, v_{x,lm}) = 0$ for $j \neq l$ and $k \neq m$) and used the above weak source approximation to eliminate cross terms proportional to the covariance between the real and imaginary part of the correlator output. For compactness of notation we have also defined:

$$\theta_{jk,lm} = \frac{2\pi(jl + km)}{N} \tag{74}$$

It may be shown that the variance $(\Delta\tilde{E}_{I,jk})^2$ is identical. Under central limit theorem ($\tau \to \infty$), the DFTs given in (62) and (63) for $\tilde{E}_{R,jk}$ and $\tilde{E}_{I,jk}$ are sums of joint Gaussian random variables, and it follows that $\tilde{E}_{R,jk}$ and $\tilde{E}_{I,jk}$ are also joint Gaussian random variables with mean and variance given above.

The aperture field phase, which we define by

$$\tilde{\theta}_a = \tan^{-1}\left(\frac{\tilde{E}_{I,jk}}{\tilde{E}_{R,jk}}\right) \tag{75}$$

will then have the following probability distribution (Crane & Napier, 1989):

$$P(\theta) = \frac{1}{2\pi}\exp\left(-\frac{1}{2}\frac{\langle\tilde{E}_R\rangle^2}{(\Delta\tilde{E}_I)^2}\right)\left[1 + \xi\sqrt{\pi}\exp(\xi^2)(1 + \mathrm{erf}\,\xi)\right] \tag{76}$$

$$\xi = \frac{\langle\tilde{E}_R\rangle\cos\theta}{\sqrt{2}\Delta\tilde{E}_I} \tag{77}$$

for large signal to noise ratio (i.e. $\langle\tilde{E}_R\rangle/\Delta\tilde{E}_I \gg 1$), the probability distribution for θ_c becomes sharply peaked around its mean value (0 in this case), and the associated phase error $\Delta\theta_a$ may be approximated as:

$$\Delta\theta_a \approx \frac{\Delta\tilde{E}_I}{\langle\tilde{E}_R\rangle} = \frac{\lambda_0 fM|F_0(\nu_0,0,0)|k_B\sqrt{2T_{sys}T'_{sys}}}{\Delta x^2\sqrt{A_eA'_e}S}\cdot\frac{[1 + (\rho/2fM)^2]^{p+1}}{[1 - (\rho/2fM)^2]^p}\cdot\frac{1}{\sqrt{N^2\Delta\nu\tau}} \tag{78}$$

The equivalent uncertainty σ_z in the measured surface deformation can be computed from (143) in Appendix C:

$$\begin{aligned}\sigma_z =& \frac{f + P^2/4/f}{f} \cdot \frac{\lambda_0 \Delta\theta_a}{4\pi} \\ =& \frac{f + P^2/4/f}{f} \cdot \frac{\lambda_0^2 f M |F_0(\nu_0, 0, 0)| k_B \sqrt{2 T_{sys} T'_{sys}}}{4\pi \Delta x^2 \sqrt{A_e A'_e} S} \cdot \frac{[1 + (\rho/2fM)^2]^{p+1}}{[1 - (\rho/2fM)^2]^p} \cdot \frac{1}{\sqrt{N^2 \Delta\nu\tau}}\end{aligned} \tag{79}$$

where P is the distance between the specified point in the aperture plane and primary reflector axis, λ_0 is the wavelength at the center frequency ν_0, and $|F_0(\nu_0, 0, 0)|$ is given explicitly in (69).

A.3 Effective surface deformation

The uncertainty given above in (79) for the measured surface deformation evidently depends on both the radial distance ρ from the center of the projected aperture and the radial distance P from the paraboloid axis. But since the center of the projected aperture will generally receive greater illumination from the feed than will the edges, it is more important to minimize the measurement uncertainty at the center if the antenna gain is to be maximized. We therefore define an effective r.m.s. measurement error ϵ_{rms} after (Ruze, 1966):

$$G/G_0 \approx e^{-\delta_{rms}^2} \equiv e^{-(4\pi\epsilon_{rms}^2/\lambda_0)^2} \tag{80}$$

where G and G_0 are, respectively, the on-axis gain of the antenna with and without aperture plane phase errors, and δ_{rms}^2 is the r.m.s. of the aperture field phase weighted by the aperture field:

$$\delta_{rms}^2 = \frac{\iint E'_a \Delta\theta_a^2 \, d^2\rho}{\iint E'_a \, d^2\rho} \tag{81}$$

Here, the aperture field E'_a is that produced by the feed for which the antenna gain is to be optimized, and is generally not equal to that produced by the holography test antenna feed. As mentioned in Appendix B, most GBT feeds are designed to optimize the antenna aperture efficiency, for which the edge taper is approximately 11 dB and the equivalent raised cosine exponent is 36. For convenience, we will also assume E'_a has the raised cosine form given in (101) of Appendix B, for which the aperture field is given by (66).

Substituting (78) into (81) we obtain:

$$\begin{aligned}\delta_{rms}^2 =& \delta_0^2 \frac{\int_0^U \frac{(1-u^2)^q}{(1+u^2)^{q+1}} \cdot \frac{(1+u^2)^{2p+2}}{(1-u^2)^{2p}} \, u \, du}{\int_0^U \frac{(1-u^2)^q}{(1+u^2)^{q+1}} \, u \, du} \\ =& 4\delta_0^2 \frac{B\left(1/2, 1-2p+q, 2+2p-q\right) - B\left(1/2 - U^2/2, 1-2p+q, 2+2p-q\right)}{B\left(1/2, 1+q, -q\right) - B\left(1/2 - U^2/2, 1+q, -q\right)}\end{aligned} \tag{82}$$

$$\delta_0 = \frac{\lambda_0 f M |F_0(\nu_0, 0, 0)| k_B \sqrt{2 T_{sys} T'_{sys}}}{\Delta x^2 S \sqrt{N^2 A_e A'_e \Delta\nu\tau}} \tag{83}$$

$$U = R/2fM \tag{84}$$

where $B(z, a, b)$ is defined in (128) in Appendix B. Once all terms in the above expressions are known, the effective r.m.s. surface error can be determined from the Ruze equation above:

$$\epsilon_{rms} = \frac{\lambda_0 \delta_{rms}}{4\pi} \tag{85}$$

In Section A.5 we will calculate ϵ_{rms} for various system configurations and measurement conditions and compare the result to the required 100 µm measurement uncertainty given in Section 2. We will also discuss various sources of systematic measurement error in Appendixes D, E, and F, and for these we will use the same criterion to determine the extent to which they can be neglected.

A.4 Phase and time delay fluctuations

In the analysis of Sections A.1 and A.2, it was assumed that, for fixed source coordinates θ and ϕ, the difference $t_d - t_g$ between the instrumental and geometric delay is zero and remains so for the duration of the integration time τ. Furthermore, it was assumed that the relative phase response of the signal paths corresponding to v_I, v_Q, and v'_I were constant during the same interval (including the LO contributions θ_{LO} and θ'_{LO}). In reality, however, pointing instability, disturbances in the atmosphere, differential timing jitter in the analog-to-digital converters, and differential phase noise in the LO will cause these values to fluctuate with time. If we include these effects as normally distributed, zero mean phase and time offsets, it can be shown that this contributes the following factor to both the mean real and imaginary correlator outputs:

$$\frac{e^{-\frac{1}{2}(\Delta\theta)^2}}{2\sqrt{2\pi}\Delta\nu\Delta t_d}\left\{\operatorname{erf}\left[\frac{2\pi(\nu_{LO}-\nu_0+\Delta\nu)\Delta t_d}{\sqrt{2}}\right] - \operatorname{erf}\left[\frac{2\pi(\nu_{LO}-\nu_0-\Delta\nu)\Delta t_d}{\sqrt{2}}\right]\right\} \tag{86}$$

where $\Delta\theta$ and Δt_d are the corresponding standard deviations and the function $\operatorname{erf}(z)$ is the standard error function:

$$\operatorname{erf} z = \frac{2}{\sqrt{\pi}}\int_0^z e^{-t^2}\,dt \tag{87}$$

There is a similar modification to the variances $(\Delta v_x)^2$ and $(\Delta v_y)^2$ in the correlator outputs, but in the weak source limit, the corresponding changes are negligible. The net effect therefore is a reduction in the modulus r_c of the complex correlator output and no change in the variance, so that the signal-to-noise ratio suffers a net reduction.

In the limit of small $\Delta\theta$ and Δt_d, the above factor can be expanded to second order:

$$1 - \frac{1}{2}(\Delta\theta)^2 - \frac{1}{6}\pi^2[\Delta\nu^2 + 12(\nu_{LO}-\nu_0)^2](\Delta t_d)^2 \tag{88}$$

If we assume a nominal intermediate frequency of $\nu_{IF,0} = |\nu_{LO} - \nu_0| = 750$ MHz and a bandwidth $\Delta\nu = 1$ GHz, limiting the separate contributions of $\Delta\theta$ and Δt_d to a 1% reduction in signal to noise ratio would require:

$$\Delta\theta < \sqrt{0.02} = 0.14 = 8.1^\circ \tag{89}$$

$$\Delta t_d < \sqrt{\frac{0.06}{\pi^2(\Delta\nu^2 + 12\nu_{IF,0}^2)}} = 28\,\mathrm{ps} \tag{90}$$

For a well-designed system, phase noise in the LO and timing jitter of the digital-to-analog converters should be below these thresholds, and so pointing instability and atmospheric disturbances will become the limiting factor. We will consider pointing instability first.

Using (122) we can consider the effect of a small, fluctuating pointing error $\Delta\theta$ on the geometric delay:

$$|\Delta t_g| = \frac{b\sin\theta}{c}\Delta\theta \tag{91}$$

where θ is the mean angle between the baseline vector $\vec{b}$ and the source direction $\hat{r}$ (we have assumed the length b of the antenna baseline remains fixed). If we apply the above limit to Δt_g, we can in turn limit $\Delta\theta$:

$$\Delta\theta < 28\,\mathrm{ps}\cdot\frac{c}{b\sin\theta} \tag{92}$$

For the current reference antenna location and source directions nominally on-axis with the GBT, $b \approx 60$ m and $\sin\theta \approx 1$, in which case we have $\Delta\theta < 30$". The dominant driver for short time scale pointing fluctuations is wind, and while these tend to be smaller than this upper limit, they are smaller only by a factor of a few, depending of course on wind speed and direction (Ries, 2009; Constantikes, 2003).

As for atmospheric disturbances, these are predominantly driven by turbulent fluctuations in the water vapor content of the air column along the line of sight, which in turn create fluctuations in the effective refractive index n and induced phase shift of a traversing electromagnetic wave. For two antennas separated by distance d that are viewing a source at zenith through a turbulent atmospheric layer of thickness $L \gg d$, the variance in the relative phase between the two antennas is given by the phase structure function (Thompson et al., 2017a)

$$D_\phi(d) = \left\langle|\phi(x) - \phi(x-d)|^2\right\rangle = 2.91\left(\frac{2\pi}{\lambda}\right)^2 C_n^2 L d^{5/3} \tag{93}$$

and the corresponding variance in the geometric delay t_g will be given by:

$$D_{t_g}(d) = (2\pi\nu)^{-2} D_\phi(d) = 2.91\frac{C_n^2 L d^{5/3}}{c^2} \tag{94}$$

where c is the speed of light and C_n^2 is the refractive index structure parameter, which quantifies the amount of turbulence in the atmospheric layer. L is often taken to be the size scale of clouds, or about 2 km (Thompson et al., 2017a), while C_n^2 will often be in the range of 10^{-15} to $10^{-12}\,\mathrm{m}^{-2/3}$, depending on the altitude of the layer and local weather conditions (Thompson et al., 1980).

No statistics on the structure parameter are currently available for Green Bank, but if we substitute a value of $10^{-14}\,\mathrm{m}^{-2/3}$ along with $d = 60$ m and $\lambda = 2.56$ cm, we find an r.m.s phase of 3.3° and an r.m.s. geometric delay of 0.77 ps, which is close to what is observed for the current GBT holography system (Hunter et al., 2011). Both of these are below the above thresholds for a 1% reduction in signal-to-noise ratio, although this of course is dependent on the weather conditions at the time of the holography measurement. Assuming

the antenna separation remains the same for the upgraded system, we can expect a similar level of fluctuations. For the remainder of the sensitivity analysis, we will therefore assume these effects to be negligible.

A.5 Numerical sensitivity analysis

Symbol	Description	Value
S	Source power flux density (Jy)	2
D'	Reference antenna diameter (m)	2
η'_a	Reference antenna efficiency	0.7
Δx	Aperture plane resolution (m)	6.67
N	Number of points per map row/column	20
q	Optimal GBT raised cosine illumination exponent	36
$\Delta\nu$	Instantaneous bandwidth (GHz)	1
τ	Integration time per point (s)	0.333

Table 5: Fixed system and measurement parameters for numerical sensitivity analysis

In this section we will estimate the expected r.m.s. surface measurement uncertainty ϵ_{rms} across several different parameters for the holography system and measurement conditions. To constrain the problem somewhat, we fix several of these parameters according to the system requirements given in Section 2 or some approximate assumptions about what is likely to be technically achievable. For instance, the reference antenna diameter likely cannot be much larger than 2 meters if it is to be installed in the same location as the current one, and the system instantaneous bandwidth cannot easily be made much larger than a few GHz based on current limitations to ADC technology. The number of points per row and column corresponds to an oversampling factor of 1.33, which was determined in Section F.3 to limit the measurement error due to aliasing to below the measurement uncertainty. The integration time per point is set by the maximum measurement time of ~ 10 minutes specified in Section 2 as well as the assumption that the measurement proceeds as an on-the-fly map with a maximum slew rate of one GBT beam FWHM per 4.5 integration times, which limits beam smearing to the 1% level (Mangum et al., 2007). All remaining fixed parameters are shown in Table 5.

Referring to (82) and (83) for the weighted r.m.s. aperture plane phase, to which ϵ_{rms} is proportional, the remaining quantities to be specified are the center wavelength λ_0, the raised cosine exponent p for the test antenna feed illumination, the test and reference system temperatures T_{sys} and T'_{sys}, and the test and reference antenna effective areas A_e and A'_e. For this analysis, p was varied between 5 and 70, while the center frequency $\nu_0 = c/\lambda_0$ was varied between 2 and 100 GHz with an 18 GHz gap centered on the oxygen absorption line at 60 GHz. Because the system temperatures will also vary with elevation, this was also varied between 10° and 82°.

The reference antenna effective area is specified by its diameter D' and aperture efficiency η'_a, and the test antenna effective area is specified by the GBT diameter and p through the expressions (126) and (127) for the illumination and spillover efficiencies. It will be assumed

that the reference antenna consists of a symmetric Cassegrain whose axis is aligned with that of the GBT, and in this case we can expect that the spillover temperatures for both the test and reference receiver will be similar, ignoring the small offset angle $\alpha - \beta = 12.329°$ between the Gregorian feed axis and the GBT primary reflector axis. We will therefore set $T_{sys} = T'_{sys}$.

We can further decompose the system temperature as follows:

$$T_{sys} = T_a + T_s + T_{rx} \tag{95}$$

where T_a is the uncorrelated component of the antenna temperature, T_s is the antenna spillover temperature, and T_{rx} is the receiver temperature. The antenna and spillover temperatures are given by:

$$T_a(\mathcal{E}) = \eta_s T_b(\mathcal{E}) \tag{96}$$

$$T_s = \frac{\int_0^{2\pi} \int_{\theta_H}^{\pi} T_b(\mathcal{E}(\theta_f, \phi_f))(\cos\theta_f)^{2p} \sin\theta_f \, d\theta_f \, d\phi_f}{2\pi \int_0^{\pi} (\cos\theta_f)^{2p} \sin\theta_f \, d\theta_f} \tag{97}$$

where η_s is the test antenna spillover efficiency, $(\cos\theta_f)^{2p}$ is the feed (power) pattern, and $T_b(\mathcal{E})$ is the brightness temperature for a ray propagating at elevation $\mathcal{E}$:

$$T_b(\mathcal{E}) = \begin{cases} T_{cmb} e^{-\tau_z / \sin\mathcal{E}} + T_{atm} \left(1 - e^{-\tau_z / \sin\mathcal{E}}\right) & \mathcal{E} > 0 \\ \varepsilon_{gnd} T_{gnd} & \mathcal{E} \leq 0 \end{cases} \tag{98}$$

where $T_{cmb} = 2.725$ K is the cosmic microwave background temperature, T_{atm} is the effective atmospheric temperature at frequency ν_0, τ_z is the corresponding zenith opacity, and $\varepsilon_{gnd} = 0.9$ and T_{gnd} are, respectively, the emissivity and temperature of the ground (Weng et al., 2001). We also use the zenith opacity to account for attenuation of the correlated part of the antenna temperature, which means modifying the source power flux density as follows:

$$S \to S e^{-\tau_z / \sin\mathcal{E}} \tag{99}$$

Note that in (96) the elevation corresponds to that of the GBT, whereas in (97) the elevation depends on the particular direction of the ray emanating from the feed. We will assume the receiver temperatures to follow the linear trend in noise temperature for the current state of the art cryogenic low noise amplifiers (Longhi et al., 2019):

$$T_{rx} = (0.3\,\mathrm{K} \cdot \mathrm{GHz}^{-1})\nu_0 \tag{100}$$

In order to obtain representative values for the effective atmospheric temperature, zenith opacity, and ground temperature at the site of the GBT, we have used the `Cleo` weather tool to produce archived forecasts for these values over the period 00:00 UT, September 01, 2023 to 00:00 UT, September 01, 2024. All absorption terms were included in the forecasted data except for rain, and the data were spaced in time at 4 hour increments. From these data a random selection of 100 were drawn and used to compute T_{sys} from the above expressions. In this discussion, we will present the results for two representative scenarios: Scenario 1, which represents "good" weather conditions, has T_{sys} and τ_z set to the corresponding values

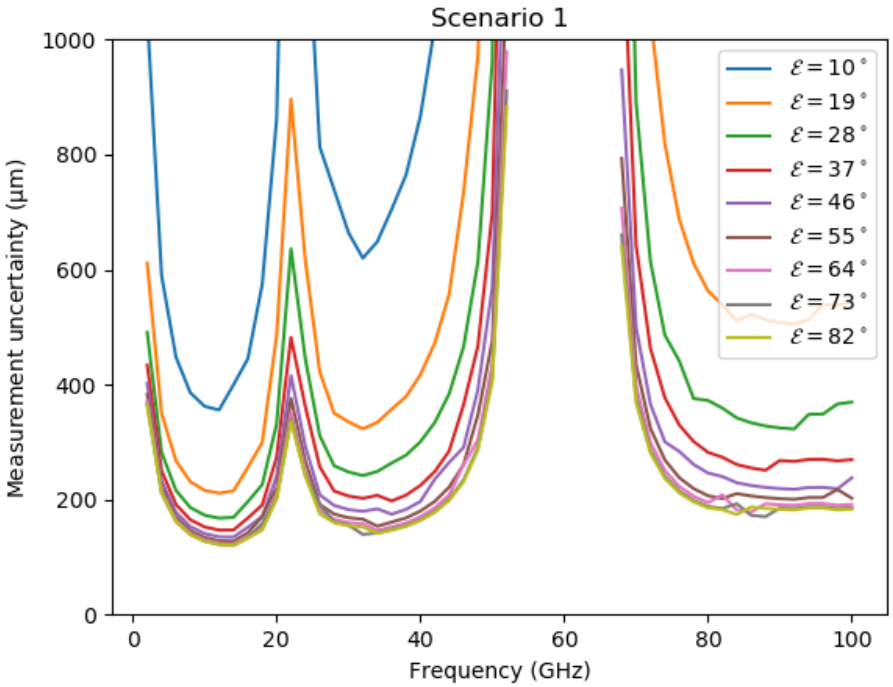

Figure 12: Simulated holography measurement uncertainty ϵ_{rms} plotted versus frequency and GBT elevation for Scenario 1. For all data, the exponent associated with the raised cosine feed illumination of the GBT was kept fixed at the value $p = 25$, which minimized ϵ_{rms} at nearly all frequencies.

at the first quartile of the 100 samples. For scenario Scenario 2, which represents "bad" weather conditions, the values are set according to the third quartile.

In Figures 12 and 13 we show the results of these computations for Scenarios 1 and 2, respectively. For reference, we also show the contributions of T_a and T_s to the zenith system temperature and the zenith opacity τ_z for both scenarios in figures 14 and 15, respectively. In all of these plots, the exponent p associated with the test antenna feed illumination was kept constant and equal to 25, which was found to be the optimum value for nearly all frequencies[4], and corresponds to an edge taper of 7.7 dB.

A few observations from Figures 12 and 13 can readily be made. Firstly, it is clear that atmospheric opacity strongly degrades the measurement sensitivity. This is particularly acute around the 22 GHz water line and the 60 GHz oxygen line, although there is an overall trend in reduced sensitivity with frequency due to the continuum absorption by water vapor. Along similar lines, we see a general worsening of sensitivity with lower elevation. The increase in measurement uncertainty towards zero frequency is a result of reduced interferometric sensitivity, i.e. the reduced change in aperture field phase with surface deformation.

For both scenarios a minimum measurement uncertainty is reached at zenith for Ku-band frequencies (14 GHz for Scenario 1 and 12 GHz for Scenario 2). For Scenario 1 the

[4]The optimum value for p deviated from 25 for only about 3-5 out of 43 frequencies, depending on the scenario, and the deviations did not exceed the sweep increment of $\Delta p = 5$.

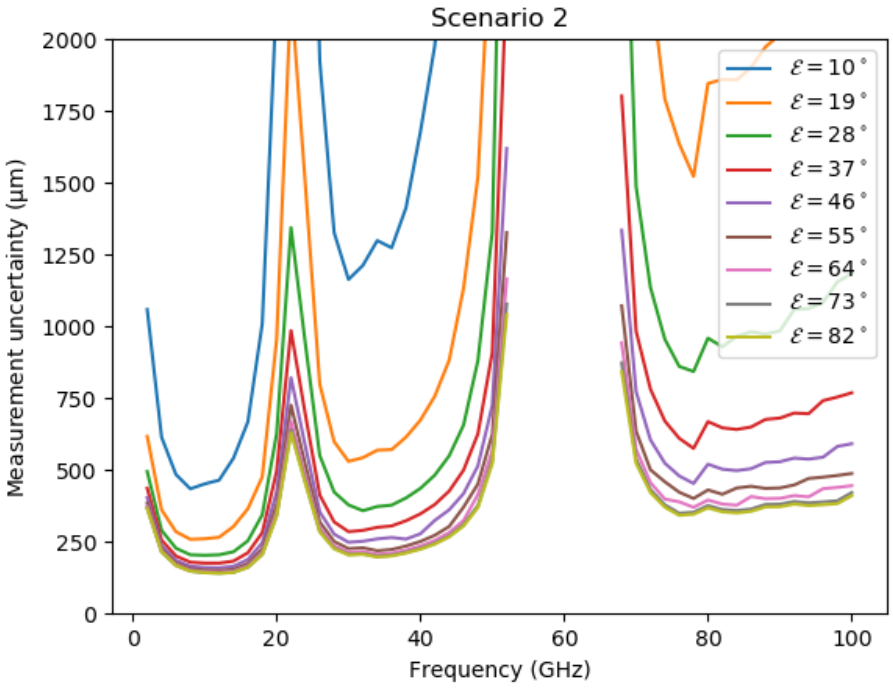

Figure 13: Simulated holography measurement uncertainty ϵ_{rms} plotted versus frequency and GBT elevation for Scenario 2. For all data, the exponent associated with the raised cosine feed illumination of the GBT was kept fixed at the value $p = 25$, which minimized ϵ_{rms} at nearly all frequencies.

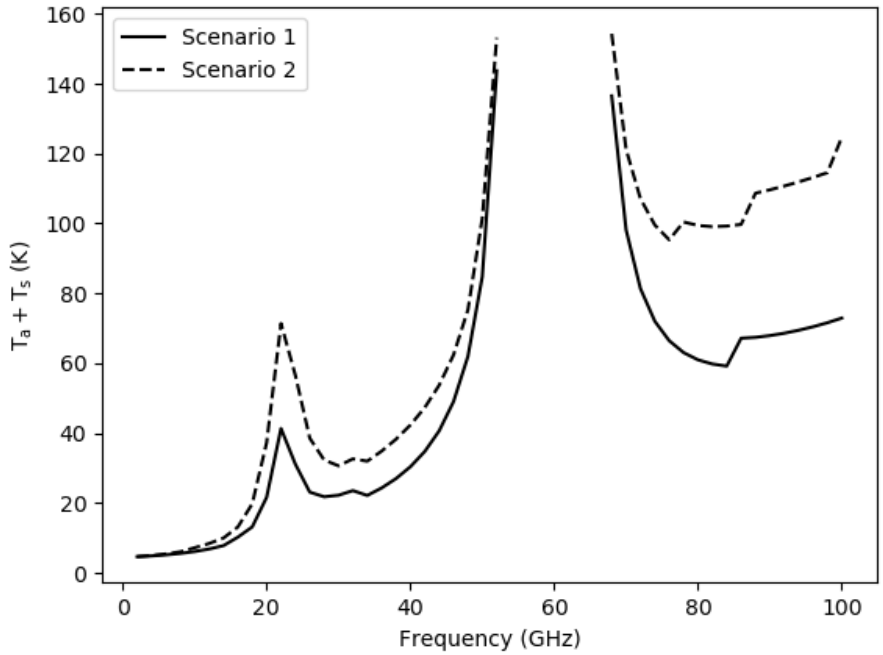

Figure 14: Contribution of antenna temperature T_a and spillover temperature T_s to the system temperature at zenith. For Scenario 1, $T_a + T_s$ is at the first quartile level and for Scenario 2 the same quantity is at the third quartile level, according to recent Green Bank weather statistics.

minimum measurement uncertainty is found to be 120 µm and for Scenario 2 it is found to be 140 µm. Both exceed the required measurement uncertainty of 100 µm specified for the current GBT holography system, although these results show that it is feasible to make moderate improvements to the corresponding system design such that this requirement can be met. In particular, if both the test and reference antennas were made dual polarized and the measurements from both polarizations were averaged, we would expect an approximate factor of $\sqrt{2}$ decrease in uncertainty to 80 µm for Scenario 1 and 100 µm for Scenario 2.

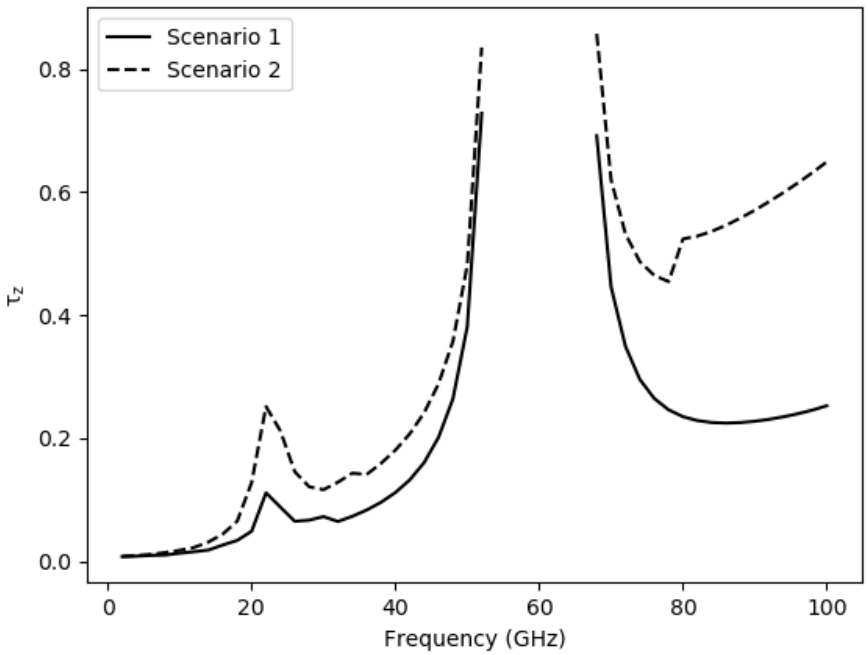

Figure 15: Similar to Figure 14, but for zenith opacity τ_z.

B Aperture field of a dual reflector antenna

In Appendix A it was shown that the sensitivity of the holography system to measure deformations at a given location depends on the strength of the aperture field at that location and the geometric mean of the system temperatures of the test and reference receivers. Thus, maintaining sensitivity over the entirety of the test reflector is a trade-off between aperture field uniformity and spillover noise, and so in this section we will provide explicit relations for the antenna's aperture field, farfield pattern, and aperture efficiency so that this relationship can be examined quantitatively. We will assume both the test antenna (the GBT) and the reference antenna are perfect (i.e. undeformed) and well-focused dual reflector antennas. While the GBT is of a Gregorian configuration, we will assume the reference antenna is of a Cassegrain configuration, but the analysis will handle both cases. In this way we will also make explicit the relative phase relationship between the test and reference antenna farfield patterns, which is required for geometric delay compensation.

For the sake of simplicity and definiteness, we will consider either antenna to consist of a feed linearly polarized along $\hat{x}_f$, and we choose the raised cosine form for its farfield pattern. The associated electric field is given (up to a proportionality constant) by (Lee, 1988b):

$$\vec{E}_f(r_f, \theta_f, \phi_f) = \begin{cases} \left[C_E(\theta_f) \cos\phi_f \, \hat{\theta}_f - C_H(\theta_f) \sin\phi_f \, \hat{\phi}_f \right] \frac{e^{-i(kr_f + \gamma_f)}}{r_f} & 0 \le \theta_f < \pi/2 \\ 0 & \pi/2 \le \theta_f < \pi \end{cases} \tag{101}$$

$$C_E(\theta_f) = (\cos\theta_f)^p \tag{102}$$

Symbol	Description	Value
α	Gregorian feed axis tilt wrt. subreflector axis	17.899°
β	Subreflector axis tilt wrt. paraboloid axis	5.57°
e	Subreflector eccentricity	0.528
a	Subreflector semimajor axis	10.417 m
θ_H	Subreflector subtended half-angle	14.99°
M	Magnification	3.166
f	Paraboloid focal length	60 m
D	Paraboloid projected aperture diameter	100 m
R	Paraboloid projected aperture radius	50 m
x_c	Paraboloid projected aperture center offset from axis	54 m

Table 6: GBT geometrical constants (Norrod & Srikanth, 1996)

$$C_H(\theta_f) = (\cos\theta_f)^q \tag{103}$$

where $C_E(\theta_f)$ and $C_H(\theta_f)$ are the E- and H-plane patterns, k is the wavevector, and (r_f, θ_f, ϕ_f) are the spherical coordinates in a coordinate system centered on the feed phase center. The phase γ_f is meant to account for the phase change between the reference plane shown in Figure 10 of Appendix A and the feed phase center. This will in general include dispersive effects due to the waveguide and the precise nature of the transition region of the feed, and so for the following analysis we will leave it unspecified. The exponents p and q parameterize the width of the forward lobe of $\vec{E}_f$, and can be determined from a specified edge taper, for example. For simplicity, we will assume the E- and H-plane patterns are equal (i.e. $p = q$). Also note that the form given above for the farfield pattern implies an additional assumption that the E- and H-plane phase centers are both located at the same point along the feed axis, i.e. $r_f = 0$.

Determining the aperture field of the primary reflector from this can be accomplished using geometric optics, from which we obtain the following result for both the Gregorian and Cassegrain antennas (Rusch, 1990; Shore & Sletten, 1988):

$$\vec{E}_a = \frac{1 + C_1 \sin\theta_f \cos\phi_f + C_2 \cos\theta_f}{2fM} \left[e^{-i[2k(a+f)+\gamma_f]} (\cos\theta_f)^p \left(\cos\phi_f \hat{\rho} - \sin\phi_f \hat{\psi} \right) \right] \tag{104}$$

$$M = \frac{|1 - e^2|}{1 + e^2 - 2e\cos\beta} \tag{105}$$

where M is the magnification of the two-reflector system, e and a are the respective eccentricity and semi-major axis of the secondary reflector, β is the angle between the secondary reflector axis and the primary, paraboloidal reflector axis, and f is the primary reflector focal length. ρ and ψ are polar coordinates for the primary reflector's aperture plane, which is offset from the primary reflector's axis by an amount (Shore & Sletten, 1988):

$$x_c = \frac{4fe\sin\beta}{1 + e^2 - 2e\cos\beta} \tag{106}$$

The aperture plane is normal to the primary reflector's axis, and we have defined its axial position such that it contains the primary reflector's focal point (i.e. prime focus).

The constants C_1 and C_2 are given by (Rusch, 1990):

$$C_1 = \frac{(e^2-1)\cos\alpha\sin\beta - [2e-(e^2+1)\cos\beta]\sin\alpha}{e^2+1-2e\cos\beta} \tag{107}$$

$$C_2 = \frac{-(e^2-1)\sin\alpha\sin\beta - [2e-(e^2+1)\cos\beta]\cos\alpha}{e^2+1-2e\cos\beta} \tag{108}$$

where α is the angle between the feed axis and the secondary reflector axis. For the particular choice of e, α, and β given in Table 6 for the GBT, it is found that $C_1 = 0$ and $C_2 = 1$. At this stage, we will also assume for simplicity that the reference antenna is of a symmetric Cassegrain design with $\alpha = \beta = 0$, and in this case we also have $C_1 = 0$ and $C_2 = 1$, but the offset (106) becomes zero, as expected.

In this case we then have the following mapping between feed coordinates and (primary reflector) aperture plane coordinates:

$$\rho = 2fM\tan(\theta_f/2) \tag{109}$$

$$\psi = \phi_f \tag{110}$$

Using these relations, we have:

$$\cos\theta_f = \cos\left[2\tan^{-1}(\rho/2fM)\right] = \frac{1-(\rho/2fM)^2}{1+(\rho/2fM)^2} \tag{111}$$

$$\begin{aligned}\frac{1+\cos\theta_f}{2} &= \cos^2(\theta_f/2) \\ &= \cos^2\left[\tan^{-1}(\rho/2fM)\right] \\ &= \frac{1}{1+(\rho/2fM)^2}\end{aligned} \tag{112}$$

which we can use to simplify the aperture field (104) as follows:

$$\vec{E}_a = \frac{e^{-i[2k(a+f)+\gamma_f]}}{fM}\frac{[1-(\rho/2fM)^2]^p}{[1+(\rho/2fM)^2]^{p+1}}\hat{x} \tag{113}$$

The antenna's farfield pattern can be computed from this using the Fourier transform (Lee, 1988b):

$$\begin{aligned}\vec{F}(\theta,\phi) =& \hat{P}_{\theta,\phi}\left[\frac{k}{2\pi}\iint e^{ik\hat{r}\cdot\vec{R}}\vec{E}_a\,d^2R\right] \\ =& \hat{P}_{\theta,\phi}\left[\frac{k}{2\pi}e^{ik\hat{r}\cdot\vec{r}_0}\iint e^{ik\hat{r}\cdot\vec{\rho}}\vec{E}_a\,d^2\rho\right] \\ =& \frac{ke^{i[k(\hat{r}\cdot\vec{r}_0-2f-2a)-\gamma_f]}(\cos\theta\cos\phi\,\hat{\theta}-\sin\phi\,\hat{\phi})}{2\pi fM}\iint e^{ik\hat{r}\cdot\vec{\rho}}\frac{[1-(\rho/2fM)^2]^p}{[1+(\rho/2fM)^2]^{p+1}}\,d^2\rho \\ \approx& \frac{ke^{i[k(\hat{r}\cdot\vec{r}_0-2f-2a)-\gamma_f]}\hat{x}}{2\pi fM}\iint e^{ik\hat{r}\cdot\vec{\rho}}\frac{[1-(\rho/2fM)^2]^p}{[1+(\rho/2fM)^2]^{p+1}}\,d^2\rho\end{aligned} \tag{114}$$

$$\hat{P}_{\theta,\phi} = \hat{I} - \hat{r}\hat{r} \tag{115}$$

The operator $\hat{P}_{\theta,\phi}$ is a projection operator, which projects out the θ and ϕ components of the quantity in brackets, which in turn is oriented along $\hat{x}$. In the last line we have assumed that θ is small, in which case $\hat{P}_{\theta,\phi}\hat{x} = \hat{x}$. Here, θ and ϕ are the spherical coordinates of a coordinate system whose polar (z) axis is aligned with that of the primary (paraboloidal) reflector, and $\hat{r}$ is the corresponding radial unit vector. The choice of origin is arbitrary, but in the second line above, we have simplified the integral by shifting the origin of the integration domain to the center of the primary reflector's projected aperture, $\vec{r}_0$:

$$\vec{R} = \vec{\rho} + \vec{r}_0 = \rho\hat{\rho} + \vec{r}_0 \tag{116}$$

It will be useful to separate out the phase factor outside the integral in (114) as follows:

$$\vec{F} = e^{i\theta_g}\vec{F}_0 \tag{117}$$

$$\theta_g = k(\hat{r}\cdot\vec{r}_0 - 2f - 2a) - \gamma_f \tag{118}$$

$$\vec{F}_0 = \frac{k(\cos\theta\cos\phi\,\hat{\theta} - \sin\phi\,\hat{\phi})}{2\pi fM}\iint e^{ik\hat{r}\cdot\vec{\rho}}\frac{[1-(\rho/2fM)^2]^p}{[1+(\rho/2fM)^2]^{p+1}}\,d^2\rho \tag{119}$$

It can be seen that the phase θ_g consists only of a constant component $-2k(f+a) - \gamma_f$ accounting for propagation from the aperture plane to the chosen reference plane at the feed input as well as a dynamic component $k\hat{r}\cdot\vec{r}_0$ which depends on the orientation of the source. For this reason, we will refer to θ_g as the *geometric phase* of the farfield pattern, to be distinguished from the phase contribution resulting from deformations of the reflector surface.

In Appendix A it was shown that the correlation of the test and reference receiver outputs will be proportional to FF'^*, where F and F' are the magnitudes of the respective test and reference antenna farfield patterns, which are assumed co-polarized. Using the definition (117) for each of these, we have:

$$FF'^* = e^{i\Delta\theta_g}F_0F_0'^* \tag{120}$$

$$\Delta\theta_g = \theta_g - \theta_g' = k[\hat{r}\cdot\vec{b} - 2(f-f') - 2(a-a')] - \gamma_f + \gamma_f' \tag{121}$$

where $\vec{b} = \vec{r}_0 - \vec{r}_0'$ is the baseline associated with the test and reference antenna. Further, if the phases γ_f and γ_f' associated with the two feeds are non-dispersive, i.e. they both may be expressed as k times some fixed distance d, then we can associate with $\Delta\theta_g$ a unique geometric time delay:

$$t_g \equiv \frac{\Delta\theta_g}{2\pi\nu} = \frac{1}{c}[\hat{r}\cdot\vec{b} - 2(f-f') - 2(a-a') - (d-d')] \tag{122}$$

where c is the speed of light and ν is the frequency. As discussed in Appendix A, compensating for this delay, either before or after correlation, is required for the holography measurement to accurately determine the phase changes associated with the deformations of the reflector.

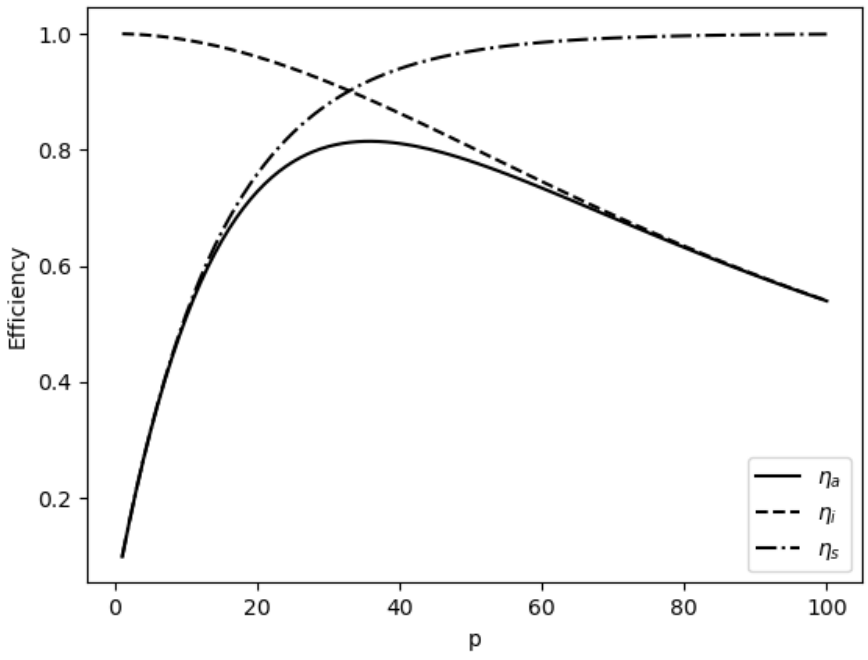

Figure 16: GBT aperture efficiency η_a, illumination efficiency η_i, and spillover efficiency η_s plotted versus exponent p for a raised cosine illumination (101).

We next determine the aperture efficiency η_a as a function of the reflector illumination, which we have parameterized by the exponent p in the raised cosine form given in (101). To do so, we'll factor the efficiency into a product of illumination efficiency η_i and spillover efficiency η_s (Thomas, 1971):

$$\eta_a = \eta_i \eta_s \tag{123}$$

$$\eta_i = 2\cot^2(\theta_H/2)\frac{\left\{\int_0^{\theta_H}\left[|C_E(\theta_f)| + |C_H(\theta_f)|\right]\tan(\theta_f/2)\,d\theta_f\right\}^2}{\int_0^{\theta_H}\left[|C_E(\theta_f)| + |C_H(\theta_f)|\right]^2\sin\theta_f\,d\theta_f} \tag{124}$$

$$\eta_s = \frac{\int_0^{\theta_H}\left[|C_E(\theta_f)|^2 + |C_H(\theta_f)|^2\right]\sin\theta_f\,d\theta_f}{\int_0^{\pi/2}\left[|C_E(\theta_f)|^2 + |C_H(\theta_f)|^2\right]\sin\theta_f\,d\theta_f} \tag{125}$$

where $C_E(\theta_f)$ and $C_H(\theta_f)$ are the E- and H-plane patterns of the feed, and θ_H is the half-angle subtended by the secondary reflector. Inserting the forms given in (102) and (103) we obtain:

$$\eta_i = \frac{(2+4p)}{1-(\cos\theta_H)^{1+2p}}\cot^2(\theta_H/2)\left[B(-1,1+p,0) - B(-\cos\theta_H, 1+p, 0)\right]^2 \tag{126}$$

$$\eta_s = 1 - (\cos\theta_H)^{1+2p} \tag{127}$$

$$B(z,a,b) = \int_0^z t^{a-1}(1-t)^{b-1}\,dt \tag{128}$$

A plot of the total aperture efficiency is shown in Figure 16 for the case of the GBT, with $\theta_H = 14.99°$. It is seen that for small p (small edge taper), the spillover efficiency is dominant, whereas for large p (large edge taper), illumination efficiency is dominant, and a maximum in η_a will occur between these two regimes. For the GBT, this maximum will occur at $p = 36$ (10.8 dB edge taper), where $\eta_a = 0.81$.

C Aperture field phase versus surface deformation

An essential step in the holography measurement is to convert the measured aperture field phase of the antenna under test into an equivalent surface deformation. In this section we will give an explicit expression for this relationship for the case of a dual reflector Gregorian antenna such as the GBT. We will treat the problem from the standpoint of geometric optics by considering an arbitrary ray emitted from the point O_g shown in Figure 17. Assuming this point coincides with one of the two foci of the secondary, ellipsoidal reflector, it will be reflected at Σ and arrive at the other focus O_p, which we take to be the prime focus of the undeformed primary reflector, which is a paraboloid.

If the primary reflector were undeformed, the ray would continue on from the prime focus to a point Γ on the primary reflector, and get reflected to a point A on the aperture plane, which we take to be the plane containing the prime focus and lying normal to the paraboloid axis. It may be shown that the total path length traversed by this ray is given by:

$$d = 2a + 2f \tag{129}$$

where a is the semimajor axis of the secondary reflector and f is the focal length of the primary reflector.

If we define a cylindrical coordinate system with origin at O_p and z-axis pointed along the primary reflector axis, we can describe the undeformed paraboloid by the equation

$$z_0(P) = P^2/4f - f \tag{130}$$

where P is the radial coordinate.

If we now turn to the actual deformed surface, which we describe by an arbitrary axial displacement Δz, we see that the original ray reflects off of a point Γ' on the deformed primary reflector, and travels an additional path length $\Delta d = \Delta d_1 + \Delta d_2$ on its way to the aperture plane, as shown in the expanded view of Figure 17. Note, we assume here and in the following analysis that the change in surface normal due to the deformation can be neglected, and so the paths $\overline{\Gamma A}$ and $\overline{\Gamma' A'}$ are parallel.

Under this assumption, we have for Δd_2:

$$\begin{aligned} \Delta d_2 =& z_0(P_0) - z(P_0 + \Delta P) \\ \approx& -\Delta z - \frac{\partial z}{\partial P}\Delta P \end{aligned} \tag{131}$$

where in the second step we have neglected higher order derivatives in the series expansion of $z(P_0 + \Delta P)$. If we denote the distance from O_p to Γ' by r_0 and associate with this a unit vector $\hat{r}$, we then have:

$$\hat{r} = \frac{P_0}{P_0^2/4f + f}\hat{P} + \frac{P_0^2/4f - f}{P_0^2/4f + f}\hat{z} \tag{132}$$

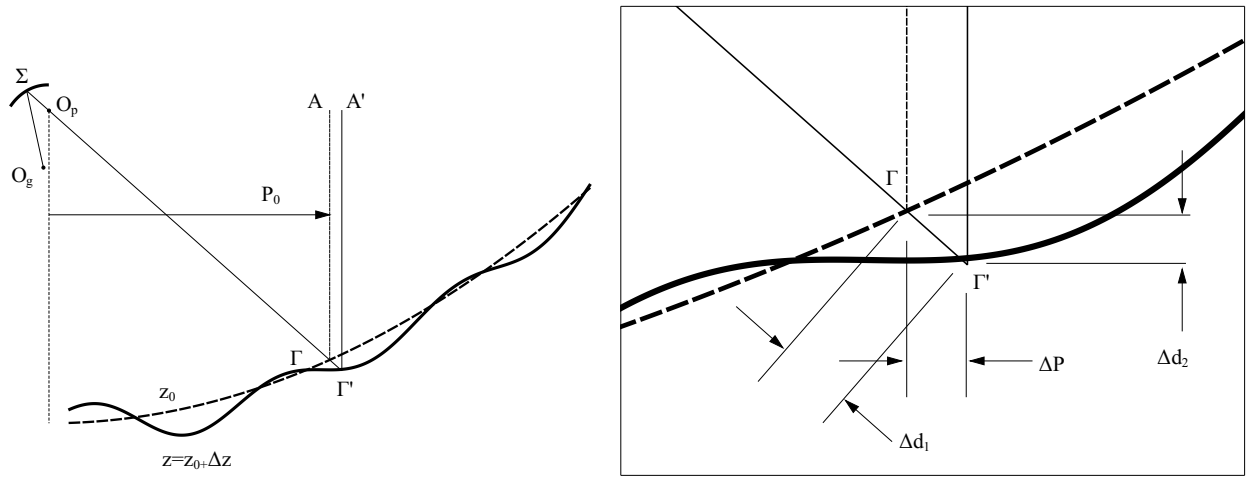

Figure 17: Ray path length analysis for a dual reflector Gregorian antenna

$$\Delta r = \Delta d_1 \tag{133}$$

$$\begin{aligned}(r_0 + \Delta r)\hat{r} =& (P_0 + \Delta P)\hat{P} + z(P_0 + \Delta P)\hat{z} \\ \approx& r_0\hat{r} + \Delta P\hat{P} + \left(\Delta z + \frac{\partial z}{\partial P}\Delta P\right)\hat{z}\end{aligned} \tag{134}$$

$$\Delta P \approx \frac{P_0}{P_0^2/4f + f}\Delta r \tag{135}$$

$$\Delta z + \frac{\partial z}{\partial P}\Delta P \approx \frac{P_0^2/4f - f}{P_0^2/4f + f}\Delta r \tag{136}$$

Solving the simultaneous equations (135) and (136):

$$\Delta P \approx \frac{P_0\Delta z}{P_0^2/4f - f - P_0\frac{\partial z}{\partial P}} \tag{137}$$

$$\Delta r \approx \frac{(P_0^2/4f + f)\Delta z}{P_0^2/4f - f - P_0\frac{\partial z}{\partial P}} \tag{138}$$

As mentioned above, we assume any change in the surface normal due to the deformation can be neglected. Thus, we can simplify the derivative:

$$\frac{\partial z}{\partial P_0} \approx \frac{dz_0}{dP} = \frac{P}{2f} \tag{139}$$

$$\Delta d_1 \approx \frac{(P_0^2/4f + f)\Delta z}{P_0^2/4f - f - P_0^2/2f} = -\Delta z \tag{140}$$

$$\Delta d_2 \approx -\Delta z - \frac{(P_0^2/2f)\Delta z}{P_0^2/4f - f - P_0^2/2f} = -\Delta z + \frac{(P_0^2/2f)\Delta z}{P_0^2/4f + f} \tag{141}$$

$$\Delta d = \Delta d_1 + \Delta d_2 \approx -2\Delta z + \frac{(P_0^2/2f)\Delta z}{P_0^2/4f + f} = \frac{-2f}{P_0^2/4f + f}\Delta z \tag{142}$$

Finally, we have for the associated aperture field phase:

$$\theta_a = -k\Delta d \approx \frac{f}{P_0^2/4f + f} \cdot \frac{4\pi\Delta z}{\lambda} \tag{143}$$

where k is the wavevector and λ is the wavelength. Note that the proportionality factor between θ_a and Δz is not constant with radial distance from the paraboloid axis. In fact, for the GBT, it varies from about $4\pi/\lambda$ near the vertex ($P_0 = 4$ m) to about $0.57 \cdot 4\pi/\lambda$ at the edge farthest from the paraboloid axis ($P_0 = 104$ m).

D Influence of dynamic gravitational deformations

D.1 Summary of gravitational deformations and their corrections

The holography measurement technique is predicated on the assumption that the antenna under test rotates rigidly as the measurement progresses. In other words, in order for the Fourier transform relationship between the measured antenna farfield pattern and the aperture field to be valid, the deformations which are to be measured must be perfectly static. This of course is only approximately true, and in fact one of the primary design criteria for the holography system upgrade is to allow for short measurement durations so that dynamic thermal and wind-induced deformations will be small. Gravitational deformations will also change with time as the telescope is pointed at various offset angles from the source, particularly if the source is non-geostationary. Since these deformations are largely repeatable, we will focus in this section on the effects these deformations will have on the holography measurement. Since, as is often the case, dynamic focus corrections are applied to the subreflector during a holography measurement, an attempt will be made to account for these as well. In principal, gravitationally-induced pointing offsets and their associated corrections will also be at play. But for low resolution holography maps ($N = D/\Delta x \approx 10$ or so), the offset pointing from the source will, depending on the wavelength, be at most $\sim 1°$, and at these offsets the pointing error will only be a negligible fraction of a beamwidth (White et al., 2022).

Much work has already been done to characterize and correct for gravitational deformations of the GBT, as has already been discussed in detail by others (Wells & King, 1995a; Wells, 1998; Constantikes, 2008; Prestage et al., 2004; Maddalena, 2014; White et al., 2022). But to briefly summarize: the GBT, owing to its offset feed design, is only a partly homologous structure. What this means in practice is that the primary reflector forms a perfect paraboloid only at its rigging elevation angle (nominally 50°), and at this position the subreflector can also be positioned such that both the Gregorian feed and the prime focus of the paraboloid can be simultaneously located at either of its two foci. At any other elevation, gravity will cause the primary reflector to deform into the approximate shape of a paraboloid with a different focal length. The feed arm will also deflect by a certain amount, displacing the two foci of the subreflector from the feed and the prime focus.

To correct for these effects, the actuators underneath the GBT primary reflector drive the reflector panels towards the nearest "best fit" paraboloid and the subreflector is driven by its actuators to a position of best focus. The best fit paraboloid is known as a function

of elevation from a combination of the GBT finite element model (FEM) (Wells & King, 1995a) and a parametric model for the residual error in the FEM (Maddalena, 2014). The latter is an empirical model based on out-of-focus (OOF) holography measurements and parameterized in terms of Zernike polynomials with elevation-dependent coefficients, and so we will refer to it as the Zernike gravity model to distinguish it from the FEM. Each Zernike polynomial coefficient (measured in microns) has the empirical form:

$$z_n = a_n \sin \mathcal{E} + b_n \cos \mathcal{E} + c_n \tag{144}$$

where $\mathcal{E}$ is the telescope elevation and a_n, b_n, and c_n are constant coefficients. These are periodically updated to reflect structural changes to the telescope, and as of this writing the latest model is Model 8.

The position of best focus for the subreflector is similarly parameterized using focus scan data. Each of the subreflector coordinates (x_s, y_s, and z_s) as well as the associated tilts have the parametrization:

$$u = a + b \cos \mathcal{E} + c \sin \mathcal{E} \tag{145}$$

(note the different naming scheme compared to the one above for the Zernike gravity model). These parameters are associated with the GBT pointing and focus tracking model, which is also periodically updated. The latest model as of this writing is Model 6a. Previous to this focus tracking model, another was developed based on a ray tracing analysis of the GBT (Wells, 1998), but this was superseded.

It must be stressed that the above corrections are not perfect, however. In particular, since the subreflector has no active surface, there are insufficient degrees of freedom to compensate for the change in separation between the Gregorian feed and the prime focus. In addition, the uncertainty in the Zernike gravity model's parameters is comparable or even larger in magnitude to the values of the parameters themselves, and so it is likely that the corrections applied to the primary reflector still have some residual error of this order (a few hundred microns for the lower order Zernike terms). Furthermore, for any observation in which a source is mapped, the active surface is set to the best fit paraboloid associated with the midpoint of the map (which for a holography scan would be the source's location halfway through the scan), but that setting remains fixed for the entirety of the map. At points other than the midpoint of the map, gravitational deformations relative to that setting occur without correction.

D.2 Evaluating the severity of dynamic gravitational deformations

As stated at the beginning of this section, the dynamic gravitational deformations which occur over the course of a holography measurement should remain "static" to within the measurement precision. To make this statement more precise, let us consider the case where the aperture field phase, which we allow to depend on elevation $\mathcal{E}$, can be expanded to first order about the elevation $\mathcal{E}_0$ at the midpoint of the holography scan:

$$\begin{aligned} \theta_a(\mathcal{E}) =& \theta_{a,0} + \Delta\theta_a \\ \approx& \theta_{a,0} + \frac{\partial \theta_a}{\partial \mathcal{E}} \Delta\mathcal{E} \end{aligned} \tag{146}$$

where $\theta_{a,0} = \theta_a(\mathcal{E}_0)$, $\Delta\mathcal{E} = \mathcal{E} - \mathcal{E}_0$ and the derivative is evaluated at $\mathcal{E}_0$. If the telescope must be moved to elevation $\mathcal{E}$ to measure the antenna farfield pattern along direction $\hat{r}$ (with spherical coordinates θ and ϕ), we can approximate the measured farfield pattern as follows:

$$\begin{aligned} F(\theta,\phi) =& \iint e^{ik\hat{r}\cdot\vec{\rho}} e^{i\theta_a}\, d^2\rho \\ \approx& \iint e^{ik\hat{r}\cdot\vec{\rho}} e^{i\theta_{a,0}} \left(1 + i\frac{\partial\theta_a}{\partial\mathcal{E}}\Delta\mathcal{E}\right) d^2\rho \\ \approx& F_0 + \Delta F \end{aligned} \tag{147}$$

$$F_0(\theta,\phi) \equiv \iint e^{ik\hat{r}\cdot\vec{\rho}} e^{i\theta_{a,0}}\, d^2\rho \tag{148}$$

$$\Delta F(\theta,\phi) \equiv i\Delta\mathcal{E} \iint e^{ik\hat{r}\cdot\vec{\rho}} e^{i\theta_{a,0}} \frac{\partial\theta_a}{\partial\mathcal{E}}\, d^2\rho \tag{149}$$

where in the first line of (147) we have assumed constant unit amplitude for the aperture field and in the second line we have assumed the change $\Delta\theta_a$ to be small. In (148) we have defined F_0 as the antenna farfield pattern at the midpoint elevation $\mathcal{E}_0$ while ΔF is the corresponding change due to $\Delta\mathcal{E}$. In the limit of small aperture field sample spacing Δx we can approximate the measured antenna aperture field by the inverse Fourier transform of F:

$$\begin{aligned} E_a =& \text{F.T.}^{-1}\left[F(\theta,\phi)\right] \\ =& E_{a,0} + \Delta E_a \end{aligned} \tag{150}$$

$$E_{a,0} \equiv \text{F.T.}^{-1}\left[F_0(\theta,\phi)\right] = \begin{cases} e^{i\theta_{a,0}} & \rho \le R \\ 0 & \rho > R \end{cases} \tag{151}$$

$$\Delta E_a \equiv \text{F.T.}^{-1}\left[\Delta F(\theta,\phi)\right] \tag{152}$$

Determining the effect of the elevation change $\Delta\mathcal{E}$ then only reduces to finding the inverse Fourier transform of ΔF. Since $\Delta\mathcal{E}$ changes with coordinates θ and ϕ, we must determine this dependence first.

The telescope elevation $\mathcal{E}$ and azimuth $\mathcal{A}$ can be related to the farfield coordinates θ and ϕ as follows:

$$\sin\theta\cos\phi = -\cos\mathcal{E}_s \sin(\mathcal{A} - \mathcal{A}_s) \tag{153}$$

$$\sin\theta\sin\phi = \sin\mathcal{E}_s\cos\mathcal{E} - \cos(\mathcal{A} - \mathcal{A}_s)\cos\mathcal{E}_s\sin\mathcal{E} \tag{154}$$

where $\mathcal{A}_s$ and $\mathcal{E}_s$ are the source azimuth and elevation. For most holography measurements, particularly those with low spatial resolution in the antenna aperture plane, the offset angles $\mathcal{A} - \mathcal{A}_s$ and $\mathcal{E} - \mathcal{E}_s$ will be small, and so we can approximate the above expressions as follows:

$$\sin\theta\cos\phi \approx -(\mathcal{A} - \mathcal{A}_s)\cos\mathcal{E}_s \tag{155}$$

$$\sin\theta\sin\phi \approx -(\mathcal{E} - \mathcal{E}_s) = -\mathcal{E}_0 - \Delta\mathcal{E} + \mathcal{E}_s \tag{156}$$

If we assume the entire holography measurement lasts $T = 10$ minutes and the source orbits the celestial pole once per sidereal day, the source elevation $\mathcal{E}_s$ will change by at most:

$$\Delta\mathcal{E}_s \approx \frac{360^\circ \cdot \cos\mathcal{L}}{23.93\,\text{h}} \cdot 10\,\text{min} = 1.96^\circ \tag{157}$$

where $\mathcal{L} = +38.4330^\circ$ is the latitude of the GBT. This is about an order of magnitude larger than the angular offset for a low resolution holography measurement at Ku-band, which for a resolution of $\Delta x = D/15 = 6.67$ m is:

$$\Delta m \equiv \Delta(\sin\theta \sin\phi) = \lambda/\Delta x = 0.2^\circ \tag{158}$$

The telescope in this case is essentially tracking the source while making only small angular offsets to measure the antenna farfield pattern. If we approximate this by a linear function of the time relative to the time t_0 at the midpoint of the scan and we further assume $\mathcal{E}_s(t_0) = \mathcal{E}_0$:

$$\mathcal{E}_s = \frac{\Delta\mathcal{E}_s}{T}(t - t_0) + \mathcal{E}_0 \tag{159}$$

we have for $\Delta\mathcal{E}$:

$$\Delta\mathcal{E} \approx \mathcal{E}_s - \mathcal{E}_0 = \frac{\Delta\mathcal{E}_s}{T}(t - t_0) \tag{160}$$

Conventionally, holography measurements are performed as `RALongMap` scans, in which the telescope is raster scanned along parallel rows of constant declination, with the declination incremented between rows. In this case, the left hand side of (156) will have a stair-step functional dependence on time, which we may also approximate as a linear function of the time offset from t_0. Within this approximation, we can use (160) to relate it to $\Delta\mathcal{E}$:

$$\sin\theta \sin\phi \approx \frac{\Delta m}{T}(t - t_0) = \frac{\Delta m}{\Delta\mathcal{E}_s}\Delta\mathcal{E} \tag{161}$$

Solving the above expression for $\Delta\mathcal{E}$ then gives the explicit dependence on θ and ϕ that is required:

$$\Delta\mathcal{E} = \kappa \sin\theta \sin\phi \tag{162}$$

$$\kappa \equiv \frac{\Delta\mathcal{E}_s}{\Delta m} \tag{163}$$

We are now prepared to compute the expression for ΔE_a:

$$\begin{aligned}
\Delta E_a =& \text{F.T.}\left[\Delta F(\theta,\phi)\right] \\
=& \text{F.T.}\left[i\Delta\mathcal{E}\iint e^{ik\hat{r}\cdot\vec{\rho}} e^{i\theta_{a,0}} \frac{\partial\theta_a}{\partial e}\, d^2\rho\right] \\
=& \frac{i\lambda\kappa}{(2\pi)^3}\iint e^{-i(k_x x + k_y y)} k_y \left[\iint e^{i(k_x x' + k_y y')} e^{i\theta_{a,0}} \frac{\partial\theta_a}{\partial\mathcal{E}}\, dx'\, dy'\right] dk_x\, dk_y \\
=& \frac{\lambda\kappa}{(2\pi)^3}\frac{\partial}{\partial y}\left[e^{i\theta_{a,0}}\frac{\partial\theta_a}{\partial\mathcal{E}}\right] \\
=& E_{a,0}(\epsilon_x + i\epsilon_y)
\end{aligned} \tag{164}$$

where in the above we have defined:

$$\epsilon_x \equiv \frac{\lambda\kappa}{(2\pi)^3}\frac{\partial^2\theta_a}{\partial y \partial\mathcal{E}} \tag{165}$$

$$\epsilon_y \equiv \frac{\lambda\kappa}{(2\pi)^3}\frac{\partial\theta_{a,0}}{\partial y}\frac{\partial\theta_a}{\partial\mathcal{E}} \tag{166}$$

and used the coordinate transformation in terms of the in-plane wavevector components:

$$k_x = \frac{2\pi}{\lambda} \sin\theta \cos\phi \tag{167}$$

$$k_y = \frac{2\pi}{\lambda} \sin\theta \sin\phi \tag{168}$$

Here, the y-axis of the aperture plane is aligned approximately orthogonal to the rows of the raster map and along the direction of monotonically increasing (or decreasing) declination. Note: in taking the partial derivative with respect to y, we have neglected the discontinuity at the edge of the aperture.

Assuming $|\Delta E_a| \ll |E_{a,0}|$, we can approximate the error $\Delta\tilde{\theta}_a$ in the measured aperture field phase $\tilde{\theta}_a$ as a result of ΔE_a:

$$\begin{aligned} \Delta\tilde{\theta}_a &= -i \log\left[\frac{E_{a,0}(E_{a,0}+\Delta E_a)^*}{|E_{a,0}||E_{a,0}+\Delta E_a|}\right] \\ &= -i \log\left(\frac{1+\epsilon_x - i\epsilon_y}{\sqrt{(1+\epsilon_x)^2+\epsilon_y^2}}\right) \\ &\approx -\epsilon_y = -\frac{\lambda\kappa}{(2\pi)^3}\frac{\partial\theta_{a,0}}{\partial y}\frac{\partial\theta_a}{\partial\mathcal{E}} \end{aligned} \tag{169}$$

In the following section, we will determine the aperture field phase θ_a from a modeled deformation of the primary reflector surface $z(\mathcal{E}, x, y)$ and using the approximate proportionality constant $4\pi/\lambda$:

$$\Delta\tilde{\theta}_a = -\frac{2\kappa}{\pi\lambda}\frac{\partial z_0}{\partial y}\frac{\partial z}{\partial\mathcal{E}} \tag{170}$$

In Section D.4, we will determine the aperture field phase from the optical path length (OPL) $l(\mathcal{E}, x, y)$ from the Gregorian feed to the aperture plane, in which case the proportionality constant is $k = 2\pi/\lambda$:

$$\Delta\tilde{\theta}_a = -\frac{\kappa}{2\pi\lambda}\frac{\partial l_0}{\partial y}\frac{\partial l}{\partial\mathcal{E}} \tag{171}$$

In either case, we will then proceed to numerically compute the effective surface measurement error ϵ_{rms} from (85).

Before proceeding, however, it is important to note that the partial derivative with respect to y in (169) is a direct consequence of the mapping sequence. If the holography scan were conducted instead as a `DecLatMap`, where the raster scan would proceed along columns of constant right ascension, $\Delta\mathcal{E}$ would no longer relate to the coordinates θ and ϕ in a straightforward manner, and the expression for $\Delta\tilde{z}$ would be more complicated. The analysis also changes if the holography map angular size Δm along the elevation direction becomes comparable to or larger than the elevation change of the source. We nevertheless use (169) as a guide in the following discussion.

D.3 Dynamic surface deformations

We will first examine the dynamic changes in the measured antenna aperture field due only to the gravitational deformations of the primary reflector surface and their associated corrections, leaving a discussion of the effects of the feed arm deflections for later. We will assume that, at the midpoint elevation $\mathcal{E}_0$ of the scan, the active surface is set according to the sum of the FEM and Zernike gravity model corrections $z_{FEM}(\mathcal{E}_0)$ and $z_Z(\mathcal{E}_0)$, respectively. Whenever these corrections are applied at any arbitrary elevation $\mathcal{E}$, we define the residual correction required to shape the reflector into the best fit paraboloid to be:

$$z_r(\mathcal{E}, \rho, \psi) \equiv \sum_{j=4}^{21} \left(\Delta a_j \sin\mathcal{E} + \Delta b_j \cos\mathcal{E} + \Delta c_j\right) Z_j(\rho/R, \psi) \tag{172}$$

where the coefficients Δa_j, Δb_j and Δc_j are normally distributed, zero mean random variables with standard deviations equal to the corresponding parameter uncertainties of the Zernike gravity model (Maddalena, 2014)[5].

Since the reflector surface is set only at the midpoint elevation of the scan, the total correction applied to the surface at any arbitrary elevation $\mathcal{E}$ will be given by:

$$z_{c,0} = z_{FEM}(\mathcal{E}_0) + z_Z(\mathcal{E}_0) \tag{173}$$

whereas the required surface correction is given by:

$$z_c(\mathcal{E}) = z_{FEM}(\mathcal{E}) + z_Z(\mathcal{E}) + z_r(\mathcal{E}) \tag{174}$$

The difference between these is just the net remaining surface deformation z:

$$z = z_{c,0} - z_c = -z_r(\mathcal{E}) - \Delta z_{FEM}(\mathcal{E}) - \Delta z_Z(\mathcal{E}) \tag{175}$$

$$\Delta z_{FEM}(\mathcal{E}) \equiv z_{FEM}(\mathcal{E}) - z_{FEM}(\mathcal{E}_0) \tag{176}$$

$$\Delta z_Z(\mathcal{E}) \equiv z_Z(\mathcal{E}) - z_Z(\mathcal{E}_0) \tag{177}$$

To evaluate the phase error $\Delta\tilde{\theta}_a$ from (170), we must then compute the following derivatives:

$$\frac{\partial z_0}{\partial y} = -\frac{\partial z_{r,0}}{\partial y} \tag{178}$$

$$\frac{\partial z}{\partial \mathcal{E}} = -\frac{\partial z_r}{\partial \mathcal{E}} - \frac{\partial z_{FEM}}{\partial \mathcal{E}} - \frac{\partial z_Z}{\partial \mathcal{E}} \tag{179}$$

where $z_0 = z(\mathcal{E}_0)$, $z_{r,0} = z_r(\mathcal{E}_0)$, and the partial derivatives with respect to $\mathcal{E}$ are evaluated at $\mathcal{E} = \mathcal{E}_0$.

In Figure 18 we show the phase error $\Delta\tilde{\theta}_a$ over the entire aperture plane for the case $\mathcal{E} = 90°$, $\kappa = 10$, and center frequency $\nu_0 = 12$ GHz, and in Figure 19 we show the

[5]Because the standard deviations σ_a, σ_b, and σ_c also reflect the scatter in the dynamic environmental conditions during the gathering of data for the empirical Zernike gravity model, this expression for z_r likely overestimates the error between the active surface setting and the correct best fit paraboloid if gravitational deformations alone are to be included.

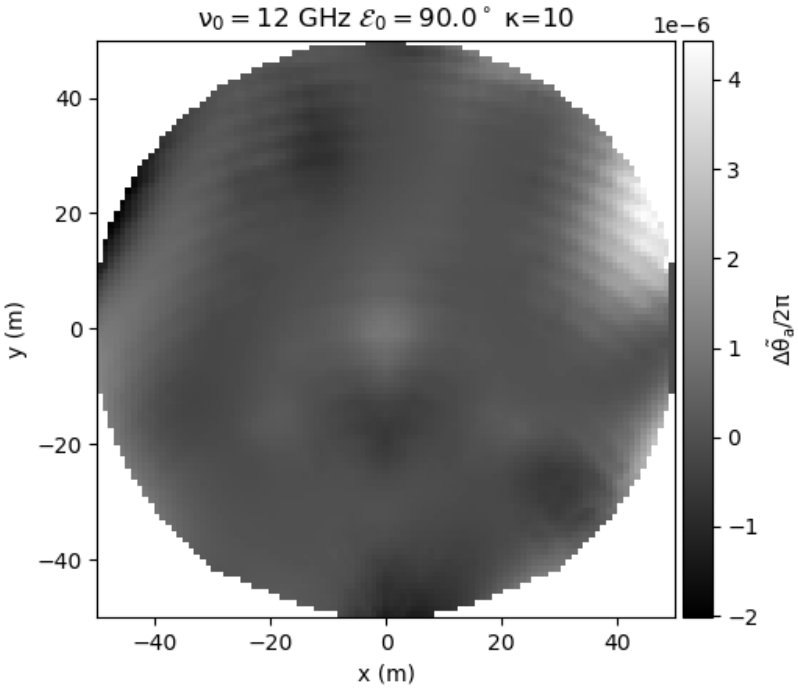

Figure 18: Simulated aperture phase measurement error $\Delta\tilde{\theta}_a$ due to dynamic gravitational changes of the surface. Here, the midpoint elevation of the simulated holography scan is 90° and the source change in elevation $\Delta\mathcal{E}_s$ is assumed to be ten times the angular size of the holography map.

equivalent deformation measurement error ϵ_{rms} calculated from (85) for several elevations between 10° and 90°. The partial derivatives given above were evaluated numerically with step sizes of $\Delta\mathcal{E} = 1.0°$ and $\Delta y = 1.0$ m, and the residual error z_r was simulated over 100 iterations according to the statistical properties mentioned earlier for the coefficients Δa_j, Δb_j, and Δc_j. Both figures 18 and 19 reflect the average over those 100 iterations. The versions used for the FEM and Zernike gravity model were 95b and 8, respectively.

From Figure 19 it can be seen that, over the full range of possible telescope elevations, the measurement error ϵ_{rms} associated just with the dynamic gravitational deformations of the primary reflector is about four orders of magnitude smaller than the required 100 µm measurement uncertainty for the holography system. In the context of holography measurements, we can therefore regard these deformations as effectively static.

D.4 Dynamic feed arm deflections and focus tracking

As mentioned above, when the telescope tips away from its rigging angle, the feed arm will undergo a deflection simultaneous with the deformations to the primary reflector. It is the strategy of the GBT focus tracking model to compensate both for the deflection of the feed arm and the transformation of the primary reflector into a different best fit paraboloid, whose focal length, absolute position, and orientation have all changed with respect to the

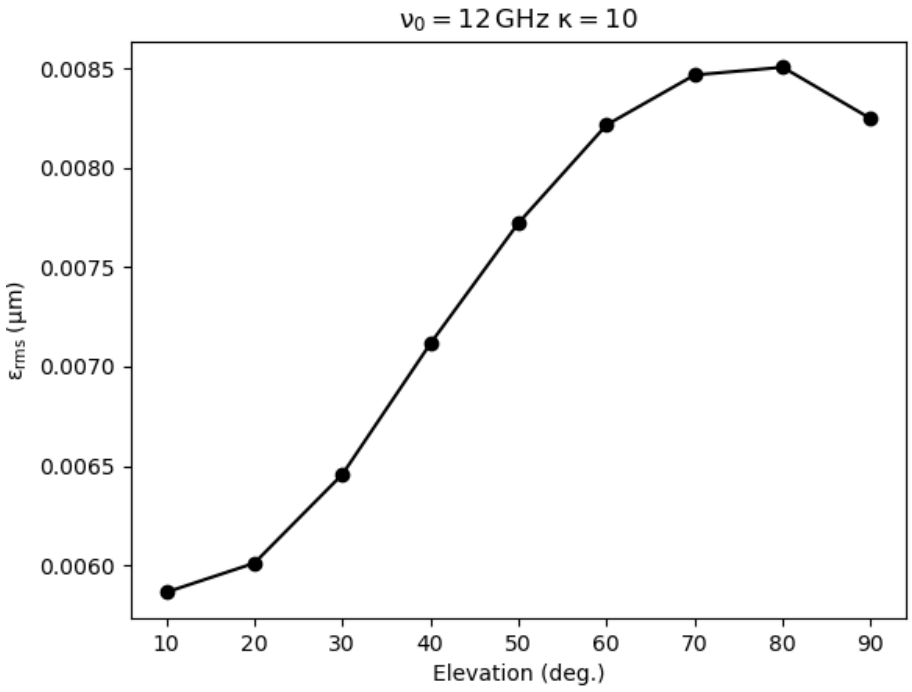

Figure 19: Equivalent surface error ϵ_{rms} due to dynamic gravitational deformations of the primary reflector, plotted as a function of the elevation at the midpoint of the holography scan. The elevation change ratio κ is fixed and equal to 10, and the center frequency ν_0 is fixed an equal to 12 GHz.

design paraboloid in the co-rotating "reflector" coordinate system (Wells & King, 1995b; Goldman, 1997). The correction applied by the focus tracking model can only ever partially compensate for the induced optical aberrations since, in general, the separation between the Gregorian feed and the prime focus of the primary reflector will be different than the separation between the two foci of the subreflector's parent ellipsoid.

In practice, then, even if the active surface corrections manage to shape the primary reflector into the best fitting paraboloid, the imperfect illumination of the primary reflector via the subreflector will still induce a nonuniform phase distribution over the projected aperture plane, and this too will vary over the course of the holography measurement. The axial displacement z associated with the phase in this case is not due to a deformation of the primary reflector, but a change in the OPL from the Gregorian feed to the aperture plane. By using the elevation-dependent deflections and corrections from the GBT FEM and focus tracking model to determine the positions of the relevant optical elements, we can therefore use raytracing to compute the OPL as a function of elevation and position within the aperture plane and then use (171) and (85) to compute the measurement error.

In Figure 20 we show the result of this analysis for a midpoint elevation $\mathcal{E}_0 = 90°$, elevation change ratio $\kappa = 10$, and center frequency $\nu_0 = 12$ GHz. The equivalent measurement error ϵ_{rms} of the surface deformation is plotted versus midpoint elevation in Figure 21. Similarly to the preceding analysis, the derivatives in (171) were computed numerically with step sizes $\Delta\mathcal{E} = 1.0°$ and $\Delta y = 1.0$ m. Simulated rays were projected from the (deflected) Gregorian focus at regular increments of the feed spherical coordinates $\theta_{f,j} = j\Delta\theta_f$ and $\phi_{f,j} = j\Delta\phi_f$, with $\Delta\theta_f = 0.5°$ and $\Delta\phi_f = 1.0°$. The net deformations, deflections, and tilts of all relevant optical elements (Gregorian feed phase center, subreflector, and primary reflector) were incorporated using the version 95b GBT FEM and version 6a pointing focus model. So that the effects of the feed illumination alone could be studied, it was assumed that the primary reflector was in the shape of its best fit paraboloid at all elevations. Position and rotational information is given for the relevant optical elements for all simulated midpoint elevations in Table 7.

From these figures it can be seen that the measurement error associated with the elevation-dependent feed illumination is several orders of magnitude larger than that due to the elevation-dependent deformations of the primary reflector, at least when the elevation is different from the 50° rigging angle. Figure 21 shows that the equivalent surface measurement error remains below the 100 µm for all elevations, although it does climb rapidly towards this value at zenith. This can be mostly attributed to the fact that the antenna model at this elevation exhibits an approximately 0.5 radians per meter phase gradient along the y-axis, which also increases with elevation at a rate of about 0.5 radians per degree.

It is difficult to assess whether these results and those in the preceding section above are indicative of the true measurement errors one would encounter in an actual holography measurement. For one thing, a phase gradient of 0.5 radians per meter at $\nu_0 = 12$ GHz would produce a pointing offset of about 7'. This is comparable in size to both the symmetric and asymmetric gravity terms of the current pointing model, which has not been included in the raytracing simulation (White et al., 2022). A second source of uncertainty in the model is the accuracy of the GBT FEM used to determine the positions and orientations of the optical elements. For the present purposes, however, it is perhaps enough to say that, on an order of magnitude basis, the interplay between the pointing model, focus tracking model,

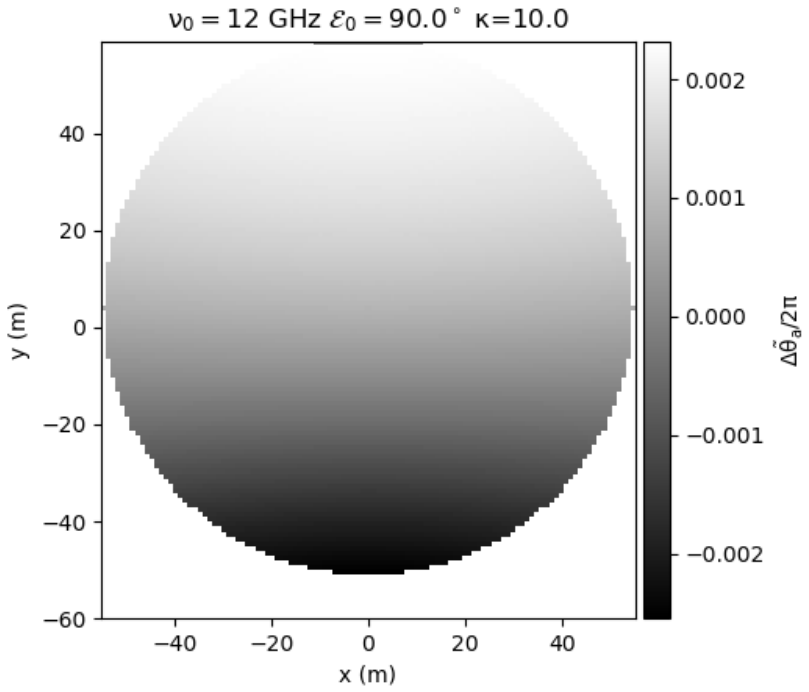

Figure 20: Simulated aperture phase measurement error $\Delta\tilde{\theta}_a$ due to dynamic gravitational changes of the feed arm combined with focus tracking. Here, the midpoint elevation of the simulated holography scan is 90° and the source change in elevation $\Delta\mathcal{E}_s$ is assumed to be ten times the angular size of the holography map.

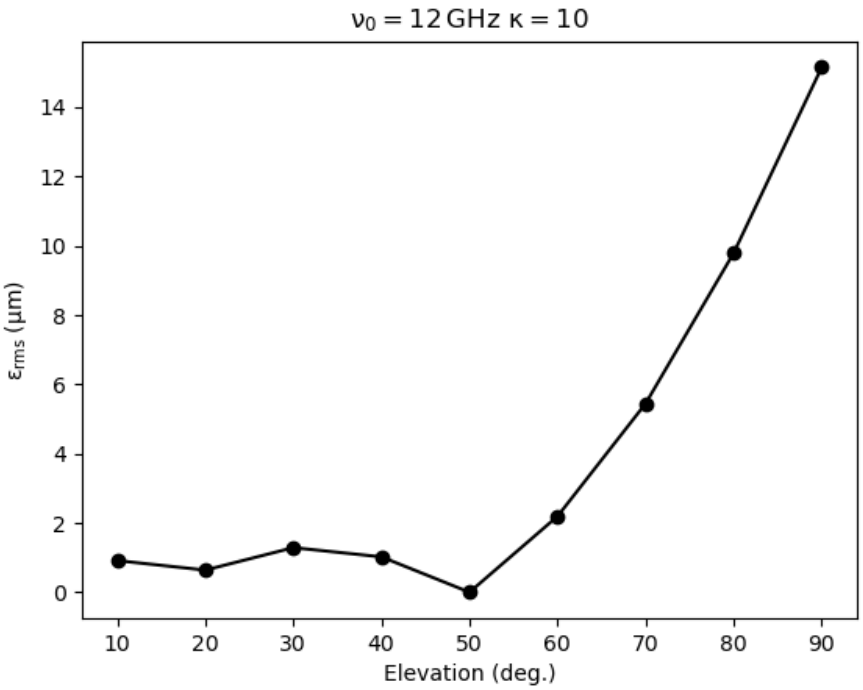

Figure 21: Equivalent surface error ϵ_{rms} due to dynamic gravitational deformations of the feed arm and focus tracking errors, plotted as a function of the elevation at the midpoint of the holography scan. The elevation change ratio κ is fixed and equal to 10, and the center frequency ν_0 is fixed an equal to 12 GHz.

and gravitational deflections of the feed arm are far more dynamic than the gravitational deformations of the primary reflector, and there is at least a potential for those effects to introduce systematic errors into the holography measurement.

$\mathcal{E}$	y_f	z_f	α'	y_s	z_s	β'	f	y_r	z_r	γ'
10	-1.0312	-10.9223	12.17	-0.5655	-5.4764	-5.71	60.0023	-8.0800	7.7883	-0.14
20	-1.0288	-10.9293	12.21	-0.5617	-5.4772	-5.68	60.0008	-8.0900	7.7762	-0.11
30	-1.0342	-10.9360	12.25	-0.5550	-5.4771	-5.65	59.9999	-8.1087	7.7642	-0.08
40	-1.0473	-10.9423	12.29	-0.5456	-5.4760	-5.61	59.9996	-8.1356	7.7525	-0.04
50	-1.0677	-10.9481	12.33	-0.5338	-5.4740	-5.57	60.0000	-8.1699	7.7417	0.00
60	-1.0947	-10.9530	12.37	-0.5200	-5.4711	-5.53	60.0010	-8.2106	7.7320	0.04
70	-1.1276	-10.9571	12.40	-0.5046	-5.4674	-5.49	60.0027	-8.2563	7.7237	0.08
80	-1.1654	-10.9601	12.43	-0.4880	-5.4629	-5.46	60.0049	-8.3058	7.7170	0.11
90	-1.2068	-10.9620	12.46	-0.4708	-5.4578	-5.43	60.0077	-8.3574	7.7123	0.14

Table 7: Positions and rotations of relevant optical elements from ray tracing simulations, as determined from the GBT finite element model version 95b and focus tracking model 6a. $\mathcal{E}$ is the telescope elevation; (y_f, z_f, α'), (y_s, z_f, β'), and (y_r, z_r, γ') are the respective coordinates and inclination angles of the Gregorian feed, subreflector parent ellipsoid, and reference feed; and f is the focal length of the primary reflector. All distances are measured in meters and all angles are measured in degrees in a coordinate system centered on the primary reflector's prime focus and aligned with its z-axis along the primary reflector axis. Angles are measured with respect to the $+z$-axis.

D.5 Effects on geometric delay tracking

Until now we have only considered the effects of dynamic gravitational deformations just to the farfield pattern of the antenna under test, which in Appendix B was denoted $F_0(\nu, \theta, \phi)$ (see Equation (117)). However, since the holography measurement detects both magnitude and phase, the actual quantity measured will also include the complex phase factor $e^{i\theta_g}$ which is due to the relative propagation delay t_g between the test and reference receivers. If the reference antenna is placed at the top of the feed arm, both it and the test receiver will be subject to the dynamic gravitational deflections described in the previous section. Since the geometric phase delay must be tracked and compensated by an equal instrumental delay t_d in order to maintain coherence between the test and reference signals before correlation, delay tracking requires accurate tracking or foreknowledge of the dynamic changes in t_g due to changing gravitational deformations (see Figure 11 in Appendix A for the effect delay error has on the modulus r_c of the complex correlator output).

We re-state the expression (122) for t_g below:

$$t_g = \frac{1}{c}\left[\hat{r}\cdot\vec{b} - (l - l')\right] \tag{180}$$

where c is the speed of light, $\hat{r}$ is the source direction, $\vec{b}$ is the baseline vector pointing from the center of the reference antenna projected aperture to the corresponding point of the test

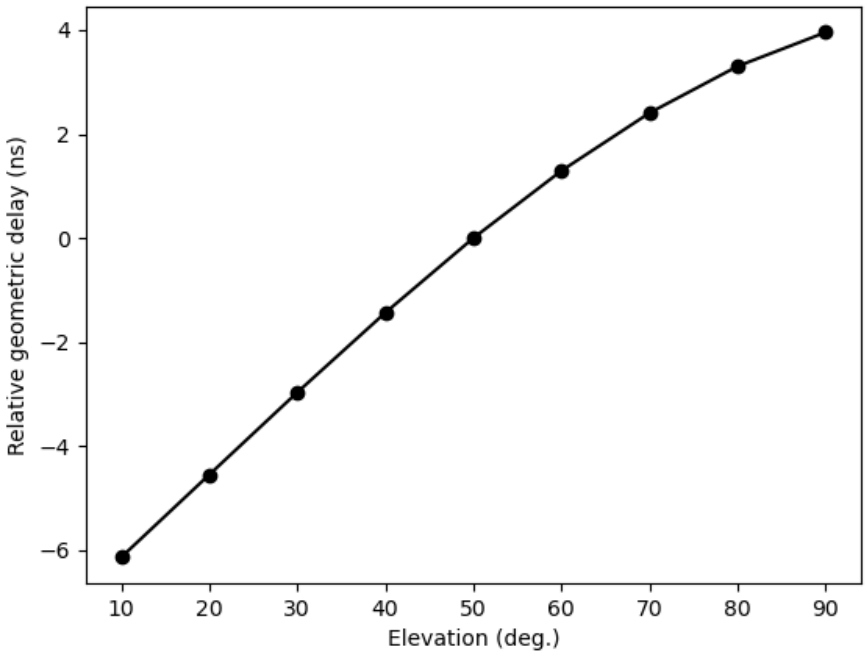

Figure 22: Geometric delay between test and reference signals relative to that in which no gravitational deformations of the GBT were present

antenna, and l and l' are the OPLs from the test and reference feeds to the aperture planes of their respective antennas, which we have defined to lie normal to the primary reflector axis and contain the prime focus. If we assume the reference antenna to be perfectly rigid, the geometric delay then contains two terms which are sensitive to gravitational changes: $\hat{r} \cdot \vec{b}$ and l.

The influence of the first term is simple enough to estimate using the GBT finite element model if one simply picks a suitable FEM node to associate with the center of the reference antenna aperture plane. For the following analysis we have chosen node `51020` (from FEM version 95b), which lies in the GBT symmetry plane $x = 0$ and whose remaining coordinates are given as y_r and z_r in Table 7 as a function of telescope elevation.

The gravity and elevation dependence of the OPL l is more difficult to determine. In (122) it was shown equal to twice the sum of the GBT focal length f and the subreflector semimajor axis a, however this only applies when the GBT optics are perfectly aligned. As we have seen in the previous section, the OPL at any elevation other than the rigging angle will vary over the aperture plane. But since the spatial variations of the OPL across the aperture are what one desires to measure, the instrumental delay needs only to compensate for the bulk, or average propagation delay from the aperture plane to the Gregorian feed. To do so, we use ray tracing in combination with the version 95b FEM and version 6a focus tracking model as was done in the analysis of the previous section. The result is shown in Figure 22 for the case when the test and reference antennas are both pointed directly at the source, which may lie at any arbitrary elevation.

In the figure, we have plotted the relative geometric delay, which is the the quantity given above in (180) averaged over the test antenna aperture plane minus the "ideal" geometric delay, which is what would occur in the absence of gravitational deformations. It can be seen that, at least for the gravitational deformations and corrections incorporated into the model, the relative propagation delay is significant in comparison with the inverse of the proposed upgraded holography system's bandwidth (1 GHz), which would lead to strong decoherence between the test and reference signals if not accurately accounted for in the compensating instrumental delay.

E Bandwidth smearing

In the sensitivity analysis of Appendix A it was assumed that the system fractional bandwidth $\Delta\nu/\nu_0$ was small, which simplified the resulting expressions for the complex correlator outputs v_x and v_y such that they were proportional to the test antenna farfield pattern evaluated at the center frequency, $F(\nu_0, \theta, \phi)$ (see Equations (26) and (27)). In this section we will drop this quasi-monochromatic assumption, at least for those terms with the strongest frequency dependence, and examine what effect this will have on the measured antenna aperture field and its phase. It will be shown that the effect results in a radial smearing of the measured aperture field, which is analogous to the *bandwidth smearing* effect referred to in the context of imaging radio interferometry (Thompson et al., 2017b).

Since the model for the aperture field in the sensitivity analysis was real, we can restrict attention to the real part of the measured test antenna farfield pattern, which in turn is proportional to the real part of the complex correlator output v_x. In (24) it was shown that v_x was proportional to the following integral over frequency before making the quasi-monochromatic assumption:

$$v_x \propto \int_{\nu_{min}}^{\nu_{max}} \sqrt{A_e A'_e} S \frac{F_0(\nu, \theta, \phi)}{|F_0(\nu, 0, 0)|} d\nu \tag{181}$$

where in the above we have ignored all frequency-independent terms and assumed that the geometric phase delay has been exactly canceled by the instrumental time delay (see Appendix B). The bounds of the frequency integral ν_{min} and ν_{max} are defined in terms of the system bandwidth $\Delta\nu$ and center frequency ν_0:

$$\nu_{min} = \nu_0 - \Delta\nu/2 \tag{182}$$

$$\nu_{max} = \nu_0 + \Delta\nu/2 \tag{183}$$

The effective antenna areas A_e and A'_e will depend on frequency through changes in the beamwidths of their respective feeds. However, if we assume that the antennas are illuminated close to their maximum antenna efficiency (see Figure 16), we can assume that any frequency dependence will be small, and these can still be brought out of the integral. The incident power flux density S is assumed to be that of a blackbody with solid angle Ω_s and brightness temperature T_B:

$$S = \frac{2k_B\nu^2}{c^2} T_B \Omega_s \tag{184}$$

In the Raleigh-Jeans limit, T_B can be assumed constant and equal to the thermodynamic temperature of the source, and so S contributes a factor ν^2 to the integral.

The test antenna farfield pattern $F_0(\nu, \theta, \phi)$ (normalized by its on-axis value $F_0(\nu, 0, 0)$) contains the largest frequency dependence through the presence of the wavevector k in the Fourier kernel $e^{ik\hat{r}\cdot\vec{\rho}}$. If we use (114) to express it as a Fourier transform of the aperture field, and retain all remaining frequency-dependent terms in the integral, we have:

$$\begin{aligned} v_x &\propto \int_{\nu_{min}}^{\nu_{max}} \nu^2 \left\{ \text{F.T.} \left[E_a(\rho, \psi) \right] (k \sin\theta, \phi) \right\} \, d\nu \\ &\propto \int_{\nu_{min}}^{\nu_{max}} \nu^2 \left[\iint e^{ik\rho \sin\theta \cos(\phi - \psi)} E_a(\rho, \psi) \, \rho \, d\rho \, d\psi \right] d\nu \\ &\propto \int_{\nu_{min}}^{\nu_{max}} \nu^2 \left[\iint e^{i(\nu/\nu_0) k_0 \rho \sin\theta \cos(\phi - \psi)} E_a(\rho, \psi) \, \rho \, d\rho \, d\psi \right] d\nu \end{aligned} \tag{185}$$

where we have used the shorthand notation F.T. to express the Fourier transform:

$$\text{F.T.} \left[E_a(\rho, \psi) \right] (k \sin\theta, \phi) = \iint e^{ik\hat{r}\cdot\vec{\rho}} E_a(\rho, \psi) \, d^2\rho \tag{186}$$

and in the last line we have expressed the wavevector in terms of that at the center frequency:

$$k = \frac{2\pi\nu}{c} = \frac{\nu}{\nu_0} \cdot \frac{2\pi\nu_0}{c} = \frac{\nu}{\nu_0} k_0 \tag{187}$$

If we make an analogous change of variables in the spatial integral:

$$\rho_\nu \equiv \frac{\nu}{\nu_0} \rho \tag{188}$$

$$E_{a,\nu}(\rho_\nu, \psi) \equiv E_a((\nu_0/\nu)\rho_\nu, \psi) = E_a(\rho, \psi) \tag{189}$$

we then have:

$$\begin{aligned} v_x &\propto \int_{\nu_{min}}^{\nu_{max}} \nu_0^2 \left[\iint e^{ik_0 \rho_\nu \sin\theta \cos(\phi - \psi)} E_{a,\nu}(\rho_\nu, \psi) \, \rho_\nu \, d\rho_\nu \, d\psi \right] d\nu \\ &\propto \int_{\nu_{min}}^{\nu_{max}} \nu_0^2 \left\{ \text{F.T.} \left[E_{a,\nu}(\rho_\nu, \psi) \right] (k_0 \sin\theta, \phi) \right\} d\nu \end{aligned} \tag{190}$$

The measured aperture field $\tilde{E}_a$ will be the discrete Fourier transform of the sequence of measurements of v_x, but in the limit that the sample spacing in the measured antenna farfield pattern tends to zero, we can approximate it by taking the continuous Fourier transform:

$$\begin{aligned} \tilde{E}_a &\propto \text{F.T.}^{-1} \left[v_x(k_0 \sin\theta, \phi) \right] (\rho, \psi) \\ &\propto \int_{\nu_{min}}^{\nu_{max}} \nu_0^2 \left(\text{F.T.}^{-1} \left\{ \text{F.T.} \left[E_{a,\nu}(\rho', \psi') \right] (k_0 \sin\theta, \phi) \right\} (\rho, \psi) \right) \, d\nu \\ &\propto \int_{\nu_{min}}^{\nu_{max}} \nu_0^2 E_{a,\nu}(\rho, \psi) \, d\nu \end{aligned} \tag{191}$$

From its definition above, it can be seen that $E_{a,\nu}(\rho,\psi)$ is a radially scaled version of the antenna aperture field (which is stretched for $\nu > \nu_0$ and contracted for $\nu < \nu_0$), and since it appears inside the frequency integral the result is a radially smeared image of the original aperture field.

Since we will be interested in characterizing the antenna surface in terms of its Zernike decomposition, it will be useful to determine the effect this radial smearing will have on the Zernike polynomials $Z_n^m(\rho,\psi)$. For simplicity, we will assume that the aperture field has uniform unit amplitude and the surface deformation is small, such that the associated phase θ_a is given by its imaginary part:

$$\begin{aligned} E_a(\rho,\psi) =& H(R-\rho)e^{i\theta_a} \\ \approx& H(R-\rho)(1+i\theta_a) \end{aligned} \tag{192}$$

where $H(x)$ is the Heaviside step function:

$$H(x) = \begin{cases} 1 & x \geq 0 \\ 0 & x < 0 \end{cases} \tag{193}$$

In this approximation, if θ_a is expressed in terms of the Zernike polynomials

$$\theta_a = \sum_{n=0}^{\infty}\sum_{m=0}^{n}\left[a_{mn}Z_n^m(\rho/R,\psi) + b_{mn}Z_n^{-m}(\rho/R,\psi)\right] \tag{194}$$

the effect of the radial smearing can therefore be understood entirely from its effect on the individual polynomials after multiplication with $H(R-\rho)$ (note: for clarity we use a different indexing scheme for the Zernike polynomials than that used in the GBT gravity model, for example). Since the Zernike polynomials can be expressed as the product of a radial part $R_n^m(\rho/R)$ and an azimuthal part:

$$Z_n^m(r,\psi) = \begin{cases} R_n^m(r)\cos m\psi & m \geq 0 \\ R_n^{-m}(r)\sin(-m\psi) & m < 0 \end{cases} \tag{195}$$

the effect of the radial smearing will affect the radial part alone (in the above we have defined the normalized radial coordinate $r = \rho/R$). From this it also follows that the radially smeared Zernike polynomial will remain orthogonal to Zernike polynomials with different azimuthal index m, and so it will have a Zernike decomposition in terms of polynomials with the same m. At the edge of the projected aperture, the measured field amplitude will no longer drop discontinuously to zero, but will gradually taper to zero over a radial distance proportional to the fractional bandwidth $\Delta\nu/\nu_0$:

$$\begin{aligned} \tilde{R}_n^m(r) &= \int_{\nu_{min}}^{\nu_{max}} H(1-(\nu_0/\nu)r)R_n^m((\nu_0/\nu)r)\,d\nu \\ &= \begin{cases} \int_{\nu_{min}}^{\nu_{max}} R_n^m((\nu_0/\nu)r)\,d\nu & r \leq \nu_{min}/\nu_0 \\ \int_{\nu_0 r}^{\nu_{max}} R_n^m((\nu_0/\nu)r)\,d\nu & \nu_{min}/\nu_0 < r \leq \nu_{max}/\nu_0 \\ 0 & r > \nu_{max}/\nu_0 \end{cases} \end{aligned} \tag{196}$$

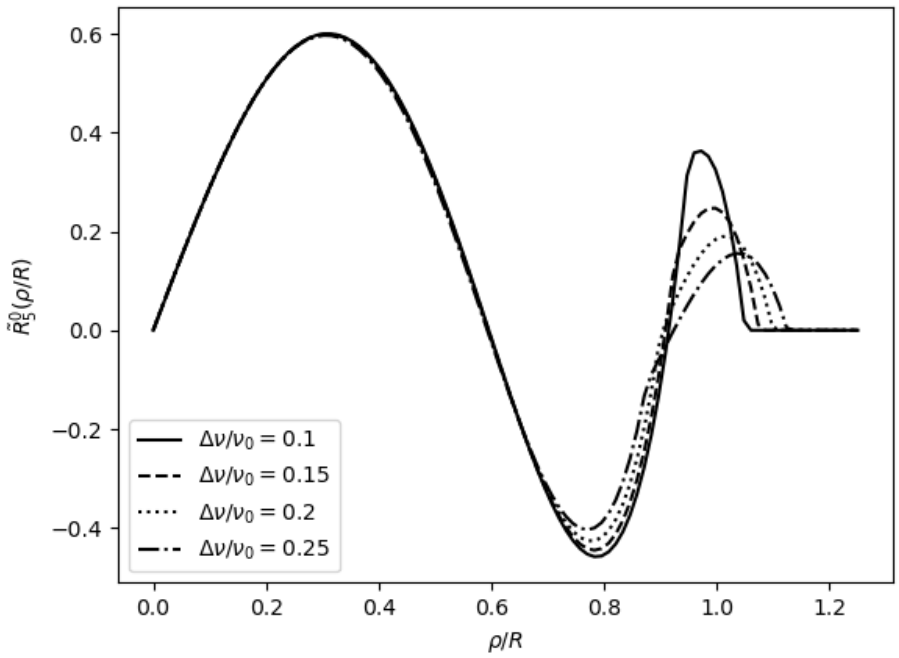

Figure 23: An example of the effect of radial smearing in the case of the Zernike radial function $R_5^0(\rho/R)$ for several different fractional bandwidths

As an example we show $\tilde{R}_5^0(r)$ for several different fractional bandwidths in Figure 23.

For the present purposes, we will consider only the interior region of the aperture field (where $r \leq \nu_{min}/\nu_0$). In this region, the real part of the measured aperture field remains constant and uniform, and so the real part of the frequency integral (191) evaluates to a constant amplitude of $\nu_0^2 \Delta\nu$. If we retain the small angle approximation for the aperture field phase θ_a, we can then give an approximate expression for the measured aperture field phase $\tilde{\theta}_a$ after bandwidth smearing:

$$\begin{aligned} \tilde{\theta}_a(r,\psi) \approx & \frac{\nu_0^2 a_{mn} \tilde{R}_n^m(r) \cos m\psi}{\nu_0^2 \Delta\nu} \\ \approx & a_{mn} \Delta\nu^{-1} \tilde{R}_n^m(r) \cos m\psi \end{aligned} \tag{197}$$

In the above we have assumed for simplicity that θ_a consists of a single even Zernike term with expansion coefficient a_{mn}. Since under the small angle approximation, a_{mn} is no larger than 1 radian, we can then define the maximum phase error as follows:

$$\Delta\theta_a \equiv \Delta\nu^{-1} \tilde{R}_n^m(r) \cos m\psi - R_n^m(r) \cos m\psi \tag{198}$$

In Table 8 we list the first set of Zernike radial functions with $1 \leq n \leq 5$ along with their smeared versions (normalized by $\Delta\nu$) as a function of the fractional bandwidth. For each of these terms we have also computed the equivalent surface measurement error ϵ_{rms} (see Equation (85)) from the phase error defined in (198) above, and plotted this as a function of fractional bandwidth for the case that the center frequency $\nu_0 = 12$ GHz.

From this it can be seen that, by and large, the error ϵ_{rms} associated with Zernike terms with higher radial indices tends to grow more rapidly with increasing fractional bandwidth than it does for lower radial index terms. But for radial indices up to $n = 5$, this error does not exceed the required surface measurement error 100 µm until a fractional bandwidth of about 0.2, which for $\nu_0 = 12$ GHz is 2.4 GHz. But given that we have not considered effects at the boundary of the aperture or Zernike terms with $n > 5$, a safety factor of, say, 2 should be probably be imposed when limiting the system bandwidth.

n	m	$R_n^m(r)$	$\Delta\nu^{-1}\tilde{R}_n^m(r)$
1	1	r	$\frac{1}{\delta}\log\left(\frac{2+\delta}{2-\delta}\right)r$
2	0	$2r^2-1$	$\frac{8}{4-\delta^2}r^2-1$
2	2	r^2	$\frac{4}{4-\delta^2}r^2$
3	1	$3r^3-2r$	$\frac{48}{(4-\delta^2)^2}r^3-\frac{4}{\delta}\tanh^{-1}(\delta/2)r$
3	3	r^3	$\frac{16}{(4-\delta^2)^2}r^3$
4	0	$6r^4-6r^2+1$	$\frac{32(12+\delta^2)}{(4-\delta^2)^3}r^4-\frac{24}{4-\delta^2}r^2+1$
4	2	$4r^4-3r^2$	$\frac{64(12+\delta^2)}{3(4-\delta^2)^3}r^4-\frac{12}{4-\delta^2}r^2$
4	4	r^4	$\frac{16(12+\delta^2)}{3(4-\delta^2)^3}r^4$
5	1	$10r^5-12r^3+3r$	$\frac{640(4+\delta^2)}{(4-\delta^2)^4}r^5-\frac{192}{(4-\delta^2)^2}r^3+\frac{6}{\delta}\tanh^{-1}(\delta/2)r$
5	3	$5r^5-4r^3$	$\frac{320(4+\delta^2)}{(4-\delta^2)^4}r^5-\frac{64}{(4-\delta^2)^2}r^3$
5	5	r^5	$\frac{64(4+\delta^2)}{(4-\delta^2)^4}r^5$

Table 8: Effect of radial smearing (191) on Zernike radial functions $R_n^m(r)$ as a function of fractional bandwidth $\delta = \Delta\nu/\nu_0$

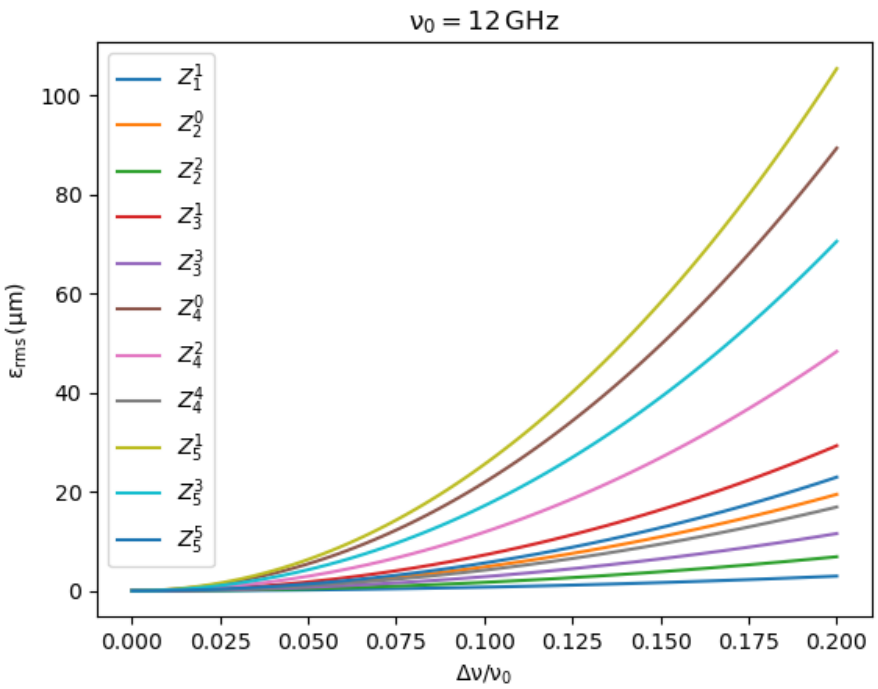

Figure 24: Effective surface measurement error ϵ_{rms} due to bandwidth smearing of the lowest order Zernike polynomials, plotted as a function of fractional bandwidth and assuming a center frequency of $\nu_0 = 12$ GHz

Should the original small angle approximation for the aperture field phase become invalid, we can improve the approximation for the exponential in (192) up to second order, for example. In this case we can see that the frequency integral (191) will involve smearing of products of Zernike polynomials, which does not preserve the angular dependence of the original polynomial. The analysis quickly becomes more complicated, and so we will not attempt it here. But the results given above may still serve as an optimistic estimate for the onset of appreciable phase measurement errors due to the effects of bandwidth smearing.

F Aperture field errors due to discrete sampling and truncation

F.1 Overview

The antenna farfield and aperture field are both defined over continuous domains and are related to each other through the continuous Fourier transform. However, in practice, one must determine one from the other from a measurement over a finite domain and a discrete set of points and approximate the Fourier transform by the discrete Fourier transform (DFT). The error in this approximation manifests as two well-known effects: the Gibbs phenomenon and aliasing. The purpose of this section is to quantify these errors in the context of holography measurements.

We consider first the one-dimensional case in which we have an aperture field $E_a(x)$ and farfield $E_f(\nu)$, where

$$\nu = \frac{\sin\theta}{\lambda} \tag{199}$$

is the wavenumber Fourier conjugate to the aperture coordinate x, θ is the corresponding angular coordinate, and λ is the wavelength. As stated above, these are Fourier transform pairs (up to a proportionality constant):

$$E_f(\nu) = \int_{-\infty}^{\infty} E_a(x) e^{2\pi i \nu x} dx. \tag{200}$$

$$E_a(x) = \int_{-\infty}^{\infty} E_f(\nu) e^{-2\pi i \nu x} d\nu. \tag{201}$$

In practice, we measure the farfield $E_f(\nu)$ over a set of N discrete points $\nu_k = k\Delta\nu$ over a finite (truncated) domain, obtaining the values $E_{f,k} = E_f(\nu_k)$ (without loss of generality we shall assume N to be even). Taking the DFT of $E_{f,k}$ approximates the desired aperture field over a discrete set of points $x_j = j\Delta x$:

$$\begin{aligned} \tilde{E}_{a,j} &= \sum_{k=-N/2}^{N/2-1} E_{f,k} e^{-2\pi i \nu_k x_j} \\ &= \sum_{k=-N/2}^{N/2-1} E_{f,k} e^{-2\pi i j k/N}, \end{aligned} \tag{202}$$

where we have used the notation $\tilde{E}_{a,j}$ to distinguish the quantity from the true aperture field $E_a(x)$. In the second line above we have used the Nyquist sampling theorem:

$$x_n = \frac{N\Delta x}{2} = \frac{L}{2} = \frac{1}{2\Delta\nu} \tag{203}$$

$$\Delta\nu\Delta x = N^{-1}, \tag{204}$$

where x_n is analogous to the Nyquist frequency in the spatial domain and is therefore equal to half the sampling frequency $\Delta\nu^{-1}$ in the reciprocal domain. $L = N\Delta x$ then defines the interval $|x| \leq L/2$ corresponding to the first Nyquist zone. In order to avoid aliasing at the zone boundaries, Holography measurements therefore must be performed with $\Delta\nu$ chosen small enough that this interval fully encloses the region where $E_a(x)$ is expected to be significant, which is typically some factor $k > 1$ times the diameter of the antenna under test. However, as will be shown below, some aliasing will nevertheless be unavoidable due to the effect of the finite sampling interval $|\nu| \leq N\Delta\nu/2$.

To proceed we use the Poisson summation formula, which states that for a given Fourier transform pair $f(x)$ and $g(\nu)$:

$$f_L(x) = \sum_{k=-\infty}^{\infty} \left[L^{-1} g(k/L)\right] e^{-2\pi i k x/L}, \tag{205}$$

where $f_L(x)$ is the periodic extension of $f(x)$ with period L:

$$f_L(x) = \sum_{k=-\infty}^{\infty} f(x - kL). \tag{206}$$

We see that the right-hand side of (205) can be made equivalent to the DFT in (202) if we regard $E_{f,k}$ as a set of discrete samples of a function $L^{-1}g'(\nu)$ and we define $g(\nu)$ as a windowed version of $g'(\nu)$:

$$g(\nu) = \Pi(\nu/Q)g'(\nu) = \begin{cases} g'(\nu) & |\nu| \leq Q/2 \\ 0 & |\nu| > Q/2, \end{cases} \tag{207}$$

where $Q = N\Delta\nu = \Delta x^{-1}$ is the width of the sampling interval and $\Pi(z)$ is the rectangular windowing function. If $f'(x)$ is the Fourier transform of the original function $g'(\nu)$, we have from the convolution theorem:

$$f(x) = f'(x) * \Delta x^{-1} \operatorname{sinc} \pi x/\Delta x, \tag{208}$$

where $*$ is the convolution operator and $Q \operatorname{sinc} \pi Q x$ is the Fourier transform of $\Pi(\nu/Q)$. In the limit as $\Delta x \to 0$ we have:

$$\lim_{\Delta x \to 0} \Delta x^{-1} \operatorname{sinc} \pi x/\Delta x = \delta(x) \tag{209}$$

where $\delta(x)$ is the Dirac delta function, and the result of the convolution is just the original function $f'(x)$, as expected. Combining these results, we can finally express the values $\tilde{E}_{a,j}$ in terms of the actual aperture field $E_a(x)$:

$$\begin{aligned}\tilde{E}_{a,j} =& L \sum_{k=-\infty}^{\infty} \left[E_a(x') * \Delta x^{-1} \operatorname{sinc} \pi x'/\Delta x\right](x_j - kL) \\ \to& L E_a(x_j)\end{aligned} \tag{210}$$

where in the second line we have taken the limit as $\Delta x \to 0$ and assumed $E_a(x)$ is zero outside the interval $L/2 \leq x < L/2$. This result may be readily extended to two dimensions:

$$\begin{aligned}\tilde{E}_{a,jk} =& L^2 \sum_{l,m=-\infty}^{\infty} \left[E_a(x', y') * *(\Delta x \Delta y)^{-1} \operatorname{sinc}(\pi x'/\Delta x) \operatorname{sinc}(\pi y'/\Delta y)\right](x_j - lL, y_k - mL) \\ \to& L^2 E_a(x_j, y_k)\end{aligned} \tag{211}$$

where $**$ represents a convolution along both x and y.

Note, however, that for any finite sample spacing $\Delta\nu$, the convolution of $E_a(x)$ with $\Delta x^{-1} \operatorname{sinc} \pi x/\Delta x$ will be nonzero outside of this interval, and so the periodic extension expressed in (211) will contain aliased components from nearby Nyquist zones. A second effect of the convolution is the Gibbs phenomenon, which results in an apparent overshoot near discontinuities. Both of these effects can be observed in Figure 25 for the case $E_a(x) = \Pi(x)$.

F.2 Holography measurement errors: Gibbs phenomenon

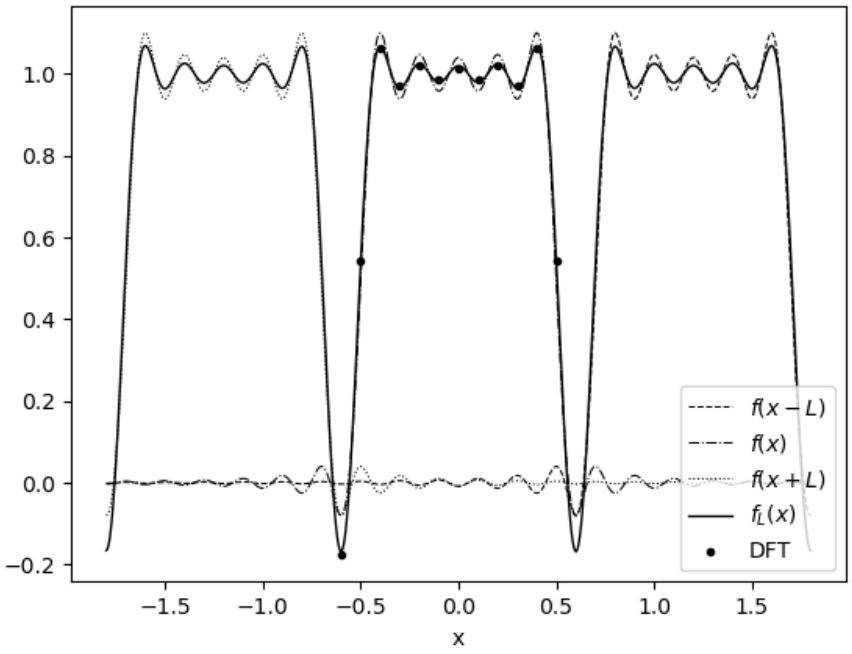

Figure 25: Example showing the discrete Fourier Transform (DFT) of the sinc function, which is equal to the rectangular function $\Pi(x)$ in the continuum limit. Discrete sampling over a finite domain results in aliasing from the periodic replicas $f(x - kL)$ in adjacent Nyquist domains and the oscillations near discontinuities (Gibbs phenomena). $f_L(x)$ is the sum of all periodic replicas as defined in (206) and is equal to the DFT at the sampled locations.

To quantify the effect of the Gibbs phenomenon separately from the effect of aliasing, we will first compute (210) for a one-dimensional model for the aperture field distribution and include only the central $k = 0$ term. We express the model aperture field as:

$$\begin{aligned} E_a(x) =& \Pi(x/D) e^{2\pi i x/a} \\ \approx& \Pi(x/D) \left[1 + 2\pi i x/a\right] \end{aligned} \tag{212}$$

where $\Pi(x)$ is same rectangular window function defined above in (207), $D = 2R$ is the aperture diameter, and we have assumed the phase $\theta_a = 2\pi x/a$ is small and has uniform gradient parameterized by a.

Inserting this into the convolution integral (208), we obtain the measured aperture field including the Gibbs phenomenon:

$$\begin{aligned} E'_a(x) =& E_a(x) * \Delta x^{-1} \operatorname{sinc} \pi x/\Delta x \\ =& E'_{a,R}(x) + i E'_{a,I}(x) \end{aligned} \tag{213}$$

$$E'_{a,R}(x) = \frac{1}{\pi} \operatorname{Si}\left[\frac{\pi(x+R)}{\Delta x}\right] - \frac{1}{\pi} \operatorname{Si}\left[\frac{\pi(x-R)}{\Delta x}\right] \tag{214}$$

$$\begin{aligned} E'_{a,I}(x) =& \frac{2\pi x}{a} \left\{ \frac{1}{\pi} \operatorname{Si}\left[\frac{\pi(x+R)}{\Delta x}\right] - \frac{1}{\pi} \operatorname{Si}\left[\frac{\pi(x-R)}{\Delta x}\right] \right. \\ & \left. + \frac{\Delta x}{\pi^2 x} \cos\left[\frac{\pi(x+R)}{\Delta x}\right] - \frac{\Delta x}{\pi^2 x} \cos\left[\frac{\pi(x-R)}{\Delta x}\right] \right\} \end{aligned} \tag{215}$$

$$\operatorname{Si}(z) = \int_0^z \frac{\sin t}{t}\, dt \tag{216}$$

For the aperture field phase θ_a we then have:

$$\begin{aligned} \theta_a =& \tan^{-1}\left(E'_{a,I}/E'_{a,R}\right) \\ \approx& E'_{a,I}/E'_{a,R} \\ \approx& \frac{2\pi x}{a} + \Delta\theta_a \end{aligned} \tag{217}$$

$$\Delta\theta_a = \frac{2\pi\Delta x}{a} \left\{ \frac{1}{\pi} \cdot \frac{\cos\left[\frac{\pi(x+R)}{\Delta x}\right] - \cos\left[\frac{\pi(x-R)}{\Delta x}\right]}{\operatorname{Si}\left[\frac{\pi(x+R)}{\Delta x}\right] - \operatorname{Si}\left[\frac{\pi(x-R)}{\Delta x}\right]} \right\} \tag{218}$$

where we have defined $\Delta\theta_a$ as the error term due to the above convolution. Figure 26 shows $\Delta\theta_a$ plotted for a few values of the grid spacing Δx and phase gradient $2\pi/a$. From the figure it is may be seen that the "overshoot" associated with the Gibbs phenomenon is prominent within about Δx of the aperture field edge, and it becomes more pronounced with both increasing phase gradient (decreasing a) and decreasing resolution (increasing Δx), as expected from Equation (218).

To compute the effective surface measurement error (85) due to the Gibbs phenomenon, we extend the model aperture field to two dimensions and retain only the $l = m = 0$ convolution term in (211). The model aperture field may be expressed analogously to (212):

$$E_a = \begin{cases} e^{2\pi i x/a} & \rho \le R \\ 0 & \rho > R \end{cases} \tag{219}$$

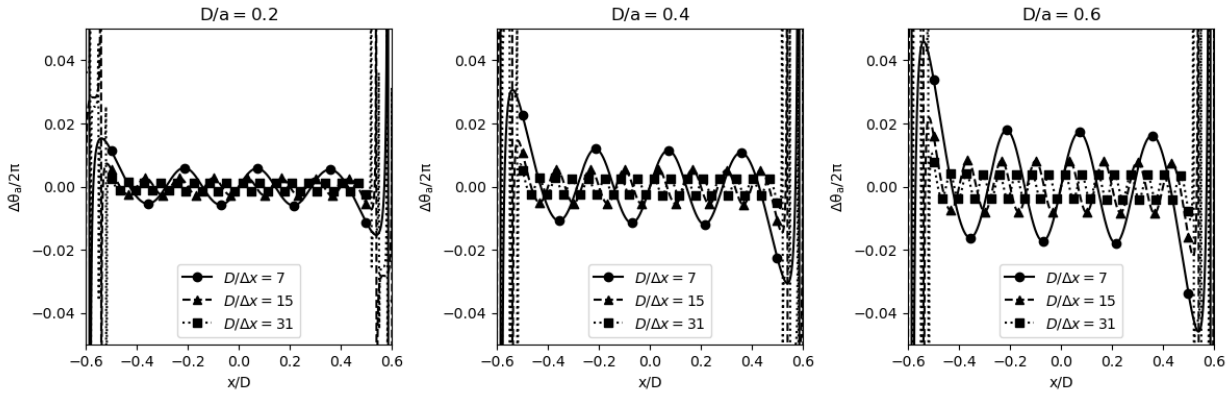

Figure 26: Phase error due to the Gibbs phenomenon in the case of the model aperture field (212) for several values of aperture plane resolution Δx and aperture field phase gradient $2\pi/a$. Markers show the associated DFT values.

In this case we will drop the small phase angle assumption and simply define the phase error $\Delta\theta_a$ as:

$$\Delta\theta_a \equiv \theta_a - 2\pi x/a \tag{220}$$

where θ_a is the aperture field phase after convolution. After substituting $\Delta\theta_a$ into (82) and carrying out the integration, we obtain the results shown in Figure 27 (both convolution and integration were performed numerically).

Here it is seen that the surface measurement error is also proportional to both the spatial resolution parameter Δx and the phase gradient parameter a^{-1}, but there is an apparent rolloff at large values of a^{-1}. This is possibly due to a breakdown of the small angle approximation used earlier, since at D/a approaching 1, the aperture field phase goes through 2π across the aperture diameter. In any case, over this range of phase gradients, all curves shown remain below the required 100 µm measurement uncertainty.

The maximum phase gradient in Figure 27 corresponds to a pointing offset of $\lambda/a = 41$" or an equivalent surface deformation gradient of $\lambda/2a = 100\,\mu\text{m}\cdot\text{m}^{-1}$. Assuming local pointing corrections were applied before commencing with the holography measurement, the pointing offset should be much smaller than this (White et al., 2022). As for the equivalent surface deformation gradient, we can estimate this following a similar procedure to that used in Section D.3. Specifically, we use a Monte Carlo method to generate random surface deformations according to the scatter in the Zernike coefficients of the GBT gravity model (Maddalena, 2014), compute the r.m.s. surface gradient for each of these, and average the results. In Figure 28 we see that for all telescope elevations, the gradients are $\sim 160\,\mu\text{m}\cdot\text{m}^{-1}$. From Figure 27 we therefore expect measurement errors due to the Gibbs phenomenon to remain about a factor of 2 below the measurement uncertainty, at least for the use case specified in Section 2 for which $\Delta x = D/15 = 6.67$ m.

F.3 Holography measurement errors: aliasing

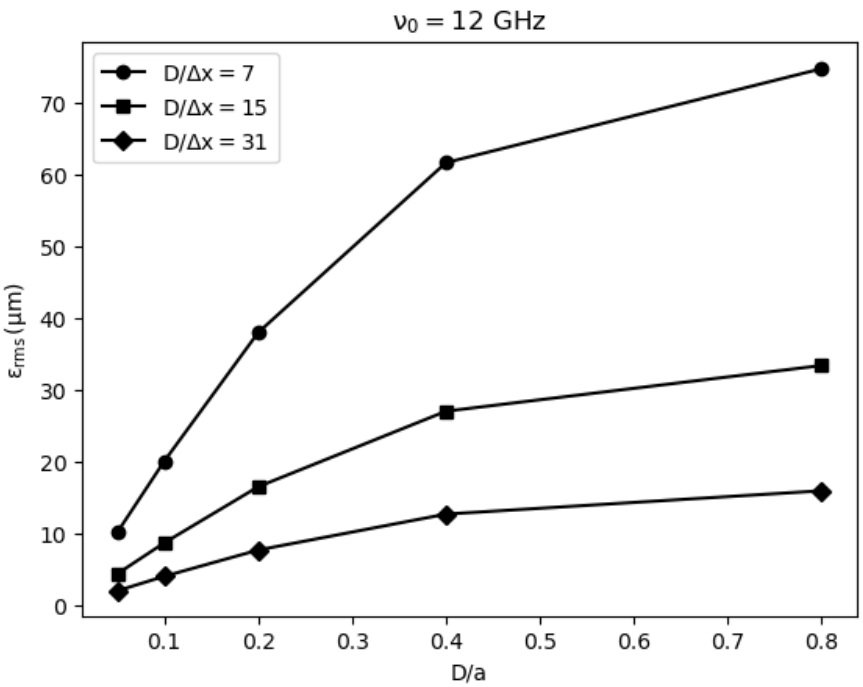

Figure 27: Equivalent surface measurement error ϵ_{rms} due to the Gibbs phenomenon plotted versus the phase gradient parameter a^{-1} for several values of the spatial resolution Δx, assuming an operating frequency of $\nu_0 = 12$ GHz

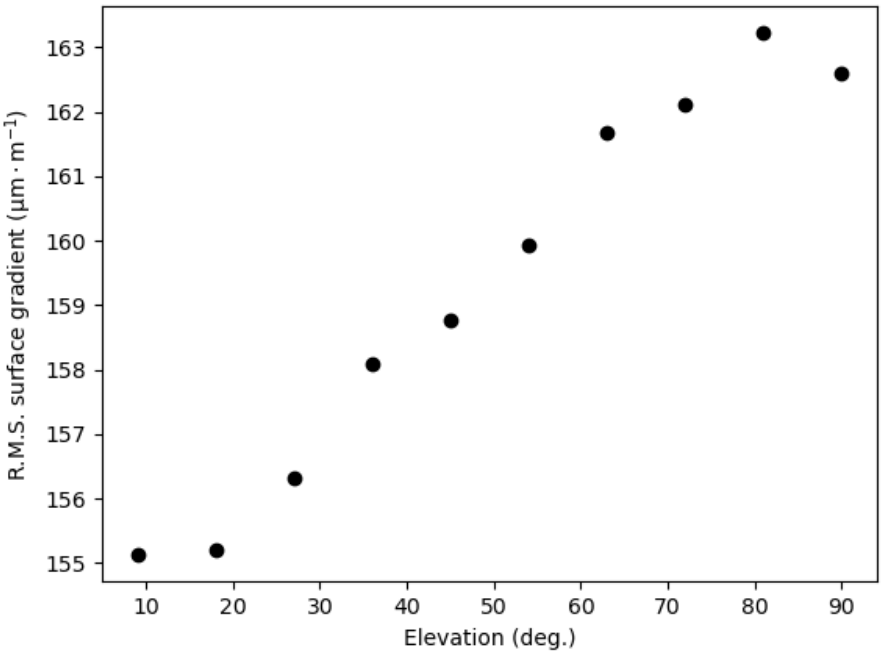

Figure 28: Simulated r.m.s. surface deformation gradient over the entire GBT projected aperture as a function of elevation. Surface deformations were modeled as Zernike polynomials whose coefficients were randomly distributed about zero and with standard deviation given by those listed in Table 1 of Maddalena (2014). Values shown were averaged over 10^4 iterations.

To estimate the measurement error due to aliasing, we will again assume a model aperture field distribution of the form (219) but with it phase equal to zero:

$$E_a = \begin{cases} 1 & \rho \leq R \\ 0 & \rho > R \end{cases} \tag{221}$$

For sufficiently large Nyquist domain size L, we need only consider terms with $-1 \leq l, m \leq 1$ in the sum (211). But in the region of overlap, $-L/2 \leq x, y \leq L/2$, we will further assume that the aliased replicas from adjacent Nyquist domains are all purely imaginary. For the real-valued model aperture field given above, this would not be the case, but we use this contrivance to estimate the worst case scenario for general aperture field distributions where the phase is not zero or even uniform.

In Figure 29 we show the model aperture field (221) after convolution as well as the imaginary-valued aliased components superimposed in the central Nyquist domain for several values of L. Note that, due to the symmetry of the model, the aliased components undergo near-total cancellation over most of the central Nyquist domain for certain values of L. Conversely, for other values the aliased components add together constructively.

We next compute the aperture field phase for each value of L and insert it into (82) in order to obtain the effective surface measurement error ϵ_{rms}. As before, the convolution integrals and integration over the aperture plane were performed numerically. The result is shown in Figure 30 for several values of the spatial resolution Δx, assuming a fixed operating frequency of $\nu_0 = 12$ GHz.

As noted above, there is a strong periodicity in L (with period Δx) due to the strong constructive and destructive interference of the aliased components, but the prevailing trend is lower measurement error with higher oversampling ratio L/D and smaller spatial resolution Δx, as would be expected. For a spatial resolution of $\Delta x = D/15 = 6.67$ m, the surface measurement error remains below the required 100 µm level for all $L > D$[6]. However, to avoid compounding systematic errors, a safety factor of, say, 2 should be applied. In this case, an oversampling ratio of 1.2 or 1.3 is recommended.

[6]Since the Gibbs phenomenon and aliasing are not totally separable effects, some of the measurement error at low oversampling ratio is partly due to the Gibbs phenomenon

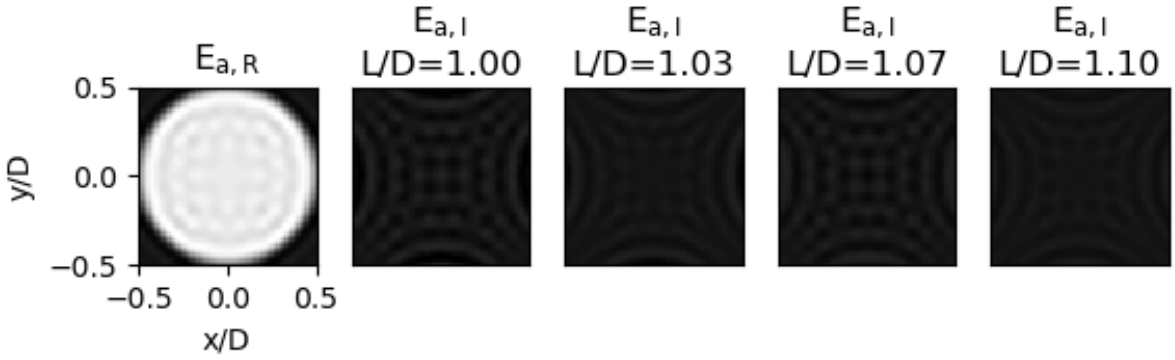

Figure 29: The first image on the left represents the model aperture field distribution (221) after convolution, which remains purely real. The three images to the right represent the aliased components, which are assumed purely imaginary, for three different values of the Nyquist domain size L relative to the aperture diameter D. The spatial resolution is $\Delta x = D/15 = 6.67$ m and he grayscale mapping is fixed for all images.

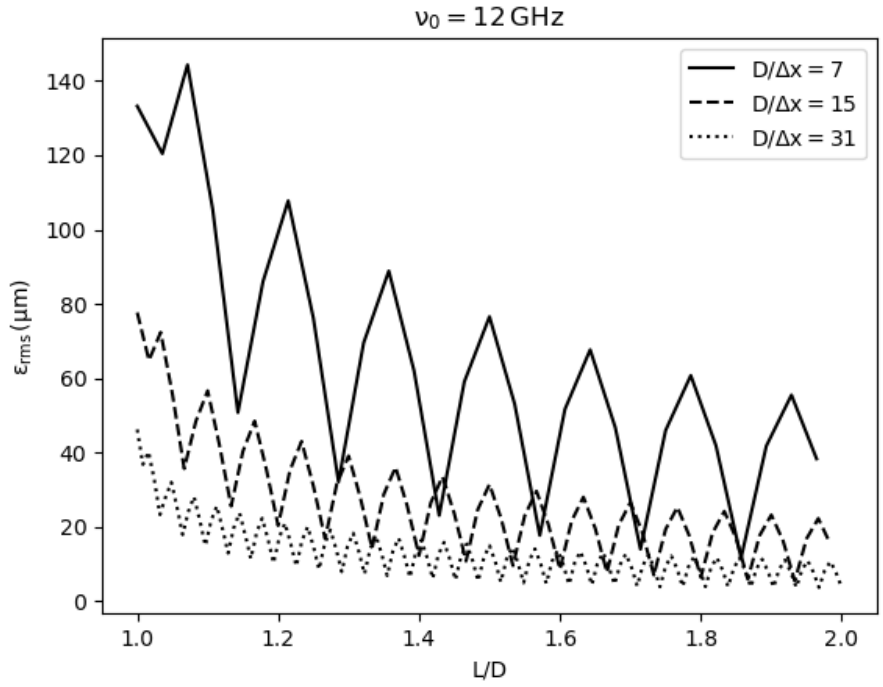

Figure 30: Effective surface measurement error ϵ_{rms} due to aliasing, computed as a function of Nyquist domain size L relative to the aperture diameter D and for three different values of the spatial resolution Δx and a fixed operating frequency $\nu_0 = 12$ GHz.